

**Microstructure Engineering During Heat Treatment of Inconel 718 Superalloy Processed
by Laser Powder Bed Fusion**

by

Yunhao Zhao

Bachelor of Engineering, Central South University, 2015

Master of Science, University of Pittsburgh, 2017

Submitted to the Graduate Faculty of the
Swanson School of Engineering in partial fulfillment
of the requirements for the degree of
Doctor of Philosophy

University of Pittsburgh

2021

UNIVERSITY OF PITTSBURGH

SWANSON SCHOOL OF ENGINEERING

This dissertation was presented

by

Yunhao Zhao

It was defended on

June 15, 2021

and approved by

Brian Gleeson, Ph.D., Harry S. Tack Chair Professor, Department of Mechanical Engineering
and Materials Science

Albert C. To, Ph.D., William Kepler Whiteford Professor, Department of Mechanical
Engineering and Materials Science

Markus Chmielus, Ph.D., Associate Professor, Department of Mechanical Engineering and
Materials Science

Youngjae Chun, Ph.D., Associate Professor, Department of Industrial Engineering /
Bioengineering

Dissertation Director: Wei Xiong, Ph.D., Assistant Professor, Department of Mechanical
Engineering and Materials Science

Copyright © by Yunhao Zhao

2021

Microstructure Engineering During Heat Treatment of Inconel 718 Superalloy Processed by Laser Powder Bed Fusion

Yunhao Zhao, Ph.D.

University of Pittsburgh, 2021

Post-heat treatment of additively manufactured (AM) Inconel 718 components is essential for optimizing microstructure and property since deformation processing is no longer applicable. Although several commercial heat treatments have been developed for wrought and cast alloys, a systematic study on the microstructure engineering during heat treatment of AM Inconel 718 is needed because its different initial microstructures from the traditional alloys can cause varied microstructure change during heat treatment and can thus influence material properties.

This dissertation comprehensively studied the microstructure engineering during the heat treatment of Inconel 718 alloy fabricated by laser powder bed fusion (LPBF). Experiments along with modeling were conducted to understand the phase transformations. The microstructure evolutions in the heat treatment stages, i.e., homogenization, continuous cooling, and aging, were investigated and the process-structure-property relationships were inferred. The microstructure change of LPBF Inconel 718 during homogenization was studied by both experiments and kinetics simulation. Homogenization at a higher temperature (1180°C) than what is used traditionally could effectively introduce recrystallization, remove columnar grain texture, and reduce residual stress. Additionally, grain refinement was achieved through recrystallization and the Zener pinning effect in LPBF Inconel 718, confirming that the mechanical properties of AM components could be potentially improved by heat treatment. During a continuous cooling process, the phase transformations of LPBF alloys were found to be different from those in suction-cast alloys and

were impacted by homogenization durations. The different phase transformation behaviors were attributed to the varied Nb homogeneities caused by diverse homogenization conditions. Microstructure evolution during isothermal aging process at intermediate temperature could be affected by homogenization conditions; more isotropic mechanical properties could be obtained with aging after high-temperature homogenization. A novel optimized heat treatment strategy was developed based on the inferred phase transformation behaviors, which achieved a combination of good strength and ductility while maintaining the properties isotropic. Moreover, a high-throughput approach leveraging the printing flexibility of LPBF was developed and the potential of accelerating heat treatment design for AM alloys was demonstrated.

Table of Contents

Preface.....	xx
1.0 Introduction.....	1
1.1 Overview of Inconel 718.....	1
1.2 Additive Manufacturing	5
1.3 State of the Art: Heat Treatment on LPBF Inconel 718.....	9
1.4 Research Motivation	17
2.0 Methodology	19
2.1 Experiment.....	19
2.2 Modeling.....	22
2.3 Summary of Methodology	27
3.0 Study on Homogenization Process Assisted by DICTRA Simulation.....	30
3.1 Homogenization Kinetics for Inconel 718 Alloys.....	32
3.1.1 Microstructure Characterization of As-fabricated Inconel 718 Alloys	32
3.1.2 Kinetic Simulations Using DICTRA	36
3.1.2.1 Model 1: Single-Phase Simulations with Laves Phase Composition from the EDS or Lever Rule	41
3.1.2.2 Model 2: Single-Phase Simulations with Segregation Profiles from Scheil Simulations.....	46
3.1.2.3 Model 3: Moving Boundary Simulations with Laves Phase Composition from the Lever Rule.....	49
3.1.3 Experimental Validation of the DICTRA Simulations.....	51

3.1.4 Discussion.....	53
3.2 Microstructure Evolution during Homogenization at 1180°C	57
3.2.1 Phase Transformations during Homogenization	57
3.2.2 Grain Size Evolution: Recrystallization and Precipitates-pinning Effects...	63
3.2.3 Dislocation Behaviors in Homogenized Inconel 718	70
4.0 Phase Transformations During Continuous Cooling	74
4.1 Experiments and Theoretical Analysis.....	75
4.1.1 Experiments.....	75
4.1.2 Theoretical Analysis.....	79
4.1.2.1 TC-PRISMA Simulation Setup	79
4.1.2.2 Key Equations in Classical Nucleation and Growth Theory	80
4.2 CCT Diagrams of LPBF and Suction-Cast Alloys	82
4.3 Effects of Homogenization on the δ Phase Transformation upon Cooling.....	84
4.3.1 Nb Homogenization in Alloys.....	84
4.3.2 Analysis Based on Classical Nucleation and Growth Theory	89
4.3.3 Analysis Based on Precipitation Simulation.....	91
4.4 Effects of Manufacturing Methods on the CCT Diagrams of δ Phase	93
4.5 Effects of Cooling Rates on Microhardness	94
5.0 Microstructure and Mechanical Property Evolution During Isothermal Aging Processes.....	98
5.1 Impact of Homogenization on Microstructure-Property Relationships	99
5.1.1 Grain Structure Evolution	99
5.1.1.1 Grain Texture in the As-built Condition.....	99

5.1.1.2 Grain Texture Evolution After Homogenization.....	102
5.1.2 Evolution of the Residual Stress	106
5.1.3 Phase Transformations during Aging Processes.....	109
5.1.4 Mechanical Properties	113
5.2 Optimization of Heat Treatment.....	116
5.2.1 Post-Heat Treatment Optimization Based on Microhardness Testing	116
5.2.2 Microstructure after Optimized Heat-Treatment.....	118
5.2.3 Tensile Properties after Optimized Heat-Treatment.....	122
6.0 Acceleration of Heat Treatment Development Using High-Throughput	
Experiment	125
6.1 The Setup of the High-Throughput Experiment	125
6.2 Microstructure and Mechanical Property Characterization	129
7.0 Conclusions and Future Work.....	133
Appendix A Calculation and experimental results of abnormal grain growth rate for	
the suction-cast sample homogenized at 1180°C for 12 h, AC12h.....	140
Bibliography	143

List of Tables

Table 1-1. Typical chemical composition of Inconel 718.....	3
Table 1-2. Summary of the differences between wrought and LPBF Inconel 718 alloys.....	12
Table 2-1. Nominal compositions of alloying elements in suction-cast alloy and LPBF powders.....	20
Table 2-2. Summary of methodology in this dissertation.....	27
Table 3-1. Compositions (in at.%) of the cast and LPBF Inconel 718 alloys measured using EDS.....	36
Table 3-2. Comparison between compositions (in at.%) of the Laves_C14 phase measured using EDS and calculated with the lever rule in the cast and LPBF Inconel 718 alloys.	44
Table 3-3. Sample notations and homogenization conditions of the present work.....	57
Table 3-4. Variation of the total phase fraction of both NbC and Laves_C14 phases during homogenization at 1180°C.....	59
Table 4-1. Sample notations and heat treatment conditions in the present work.....	75
Table 4-2. Parameters of the δ phase precipitation simulation for analyzing the effects of Nb homogeneity.....	79
Table 4-3. Comparison of the effects of homogenization durations on the CCT characteristics of the δ phase.	85
Table 5-1. Sample notations and heat treatment conditions of the present work.....	100
Table 5-2. Average grain size (diameter, μm) of samples on different planes.	102
Table 5-3. Grain boundary density (GBD, /m) of samples on different planes.....	105

Table 5-4. Average grain orientation spread (GOS, °) of samples on different planes.	109
Table 5-5. Sample notations and heat treatment conditions.....	118
Table 5-6. Summary of grain and precipitate properties in the optimized aged samples..	120
Table 5-7. Tensile properties of samples with the optimized heat treatment.....	123

List of Figures

Figure 1-1. Typical precipitate morphologies [7] of (a) Laves_C14, γ'', and γ' phases in Laser Additively Manufactured Inconel 718 and (b) δ, γ'', and γ' phases in wrought Inconel 718.	3
Figure 1-2. Systems design chart of Inconel 718 alloys prepared by additive manufacturing.	4
Figure 1-3. Available temperature profiles of heat treatments for the commercial Inconel 718 alloys.....	5
Figure 1-4. Review of laser additive manufacturing methods for metallic components [35].	6
Figure 1-5. Illustration of LPBF setup [34].	8
Figure 1-6. Schematic of typical laser metal deposition (LMD) setup [43].	9
Figure 1-7. Stress-oriented precipitation of γ'' under applied stress in Inconel 718 [53].	11
Figure 1-8. (a) Defined characteristics of CCT diagrams in this work: starting temperature, phase formation range, and critical cooling rate; (b) integration of the reported CCT diagram by Garcia et al. [62], Slama and Cizeron [70], and Niang et al. [71]. Individual phases plotted in (b) are shown in the separate plots from (c) to (e) to show each section more clearly; (c) separate plot of the CCT diagram related to the δ phase, carbides, and carbonitrides according to [62,71]; (d) separate plot of the CCT diagrams related to γ'' phase (in red curves) according to Garcia et al. [62] and related to the δ, γ', or γ'' phases (in black curves) based on Slama and Cizeron [70]; (e) separate plot of the CCT diagram related to the γ' phase according to	

Garcia et al. [62]; (f) separate plot of the CCT diagram related to the Laves phase according to Garcia et al. [62]. The different line types from Garcia et al. [62] represent the CCT curves determined after various homogenization times..... 15

Figure 3-1. X-ray diffractograms for as-cast and as-built Inconel 718 alloys..... 34

Figure 3-2. SEM-BSE micrographs of (a) as-cast and (b) as-built Inconel 718 alloys. 34

Figure 3-3. Composition profiles (mole fraction) obtained using EDS in as-cast Inconel 718 alloy for (a) all alloying elements and (b) Nb; as well as the as-built Inconel 718 alloy for (c) all alloying elements and (d) Nb..... 35

Figure 3-4. (a) Equilibrium phase fraction as a function of temperature and (b) Scheil solidification diagram for the composition of cast Inconel 718 measured using EDS. 37

Figure 3-5. Schematic illustration of the simulation setup used for estimating the homogenization time in the suction-cast and LPBF Inconel 718 alloys (a) Single-phase simulations using the composition of Laves_C14 phase from experiments or the lever rule and composition of γ from experiments (Model 1) as well as segregation profiles obtained from Scheil simulations (Model 2) and (b) moving boundary simulations with the composition of γ from experiments and composition of Laves_C14 phase from the lever rule (Model 3)..... 40

Figure 3-6. Variation of the composition of Nb at the location with the highest Nb segregation as a function of time predicted by DICTRA simulations using Model 1 with Laves_C14 phase composition from EDS line scans for cast and LPBF Inconel 718 alloys. The homogenization times for the LPBF and cast alloys are 200 s and 2500 s, respectively. 43

Figure 3-7. Composition profiles (mole fraction) used as inputs for DICTRA simulations using Model 1 where the composition of Laves_C14 phase is determined using the lever rule and the composition of the γ matrix is obtained from EDS for (a) cast and (b) LPBF Inconel 718..... 45

Figure 3-8. Variation in composition of Nb at the location with the highest Nb segregation as a function of time predicted by DICTRA simulations using Model 1 with Laves_C14 phase composition from the lever rule for cast and LPBF Inconel 718 alloys. The homogenization times for the LPBF and cast alloys are 700 s and 1500 s, respectively. 46

Figure 3-9. Segregation profiles (mole fraction) obtained using Scheil calculations and scaled to diffusion distance for (a) cast and (b) LPBF Inconel 718 alloys that are used as inputs for the DICTRA simulations using Model 2. 48

Figure 3-10. Variation in the composition of Nb at the location with the highest Nb segregation as a function of time predicted by DICTRA simulations using Model 2 for cast and LPBF Inconel 718 alloys. The homogenization times for the LPBF and cast alloys are 15000 s and 2500 s, respectively. 48

Figure 3-11. Variation of interface position as a function of time indicating the dissolution of Laves_C14 phase predicted by DICTRA simulations using Model 3 for (a) cast alloy with a homogenization time of 1250 s and (b) LPBF alloy with a homogenization time of 136 s..... 50

Figure 3-12. Variation of interface positions as a function of time indicating the dissolution of Laves_C14 phase predicted by DICTRA simulations using 3-cell moving boundary model for (a) cast alloy with a homogenization time of 847 s and (b) LPBF alloy with

a homogenization time of 87 s. Cell#1, Cell#2, and Cell#3 indicate the simulation cells with the Laves_C14 region width of $w-\delta$, w , and $w+\delta$, respectively. 51

Figure 3-13. BSE-SEM micrographs for cast alloys homogenized for (a) 20 mins, (b) 1 h, and (c) 12 h; and for LPBF alloys homogenized for (d) 20 mins, (e) 1 h, and (f) 12 h. 53

Figure 3-14. SEM-BSE micrographs of Inconel 718 suction-cast alloys with (a) as-cast state, AC; and with homogeneous states at 1180°C for (b) 20 min, AC20m; (c) 1 h, AC1h; (d) 12 h, AC12h. SEM-BSE micrographs of LPBF Inconel 718 alloys with (e) as-built state, AB; and with homogeneous states at 1180°C for (f) 20 min, AM20m; (g) 1 h, AM1h; (h) 12 h, AM12h. The representative NbC carbides and Laves_C14 phase in each sub-figure are shown in the magnified SEM images on the right-hand side thereof. 59

Figure 3-15. (a) Illustration of EDS point identification for Nb homogeneity determination (taking sample AC12h, homogenized suction-cast alloy at 1180°C for 12 h as an example); (b) Nb concentration contour diagrams (10×10 μm) in γ matrix around NbC carbides for presenting Nb homogeneity. The NbC carbides are profiled by dashed black squiggles..... 62

Figure 3-16. The average grain size of suction-cast and LPBF alloys before and after homogenization at 1180°C..... 63

Figure 3-17. Grain size distribution of (a) suction-cast alloys; and inverse pole figure (IPF) orientation maps from EBSD of suction-cast Inconel 718 alloys with (b) as-cast state, AC; and with homogeneous states at 1180°C for (c) 20 min, AC20m; (d) 1 h, AC1h; (e) 12 h, AC12h. Grain size distribution of (f) LPBF alloys; and IPF orientation maps of LPBF Inconel 718 alloys with (g) as-built state, AB; and with homogeneous states

at 1180°C for (h) 20 min, AM20m; (i) 1 h, AM1h; (j) 12 h, AM12h. (k) TEM micrograph of sample AM12h. 65

Figure 3-18. GOS distribution of (a) suction-cast alloys; and grain orientation spread (GOS) maps from EBSD of suction-cast Inconel 718 alloys with (b) as-cast state, AC; and with homogeneous states at 1180°C for (c) 20 min, AC20m; (d) 1 h, AC1h; (e) 12 h, AC12h. GOS distribution of (f) LPBF alloys; and GOS maps of LPBF Inconel 718 alloys with (g) as-built state, AB; and with homogeneous states at 1180°C for (h) 20 min, AM20m; (i) 1 h, AM1h; (j) 12 h, AM12h. 68

Figure 3-19. TEM micrographs of sample AM12h (homogenized on LPBF alloy at 1180°C for 12 h): (a) grain boundary NbC carbides and dislocation-precipitate interaction; (b) selected area electron diffraction pattern of NbC carbides; (c) planar dislocation arrays; (d) interaction between dislocations and grain boundaries..... 72

Figure 4-1. Microstructure characterization and dilatometry analysis of sample AM12h-5. (a) SEM micrograph on the longitudinal plane of AM12h-5. (b) Dilatation curve of sample AM12h-5 and its first derivative curves for determining the inflection points of phase transformations for (c) NbC ending; (d) δ starting; and (e) δ ending. 77

Figure 4-2. Effects of homogenization on the CCT diagrams of (a) LPBF alloys homogenized for 20 min and 12 h; and (b) suction-cast alloys homogenized for 20 min and 12 h. The solvus temperature of the δ phase is predicted using the Thermo-Calc software TCNI8 database. Cooling rates in the unit of K/s (from 0.1 to 15) are indicated in cooling curves superimposed to the CCT diagram plot. 82

Figure 4-3. Effects of manufacturing methods on the CCT diagrams of (a) LPBF & suction-cast alloys homogenized for 20 min; and (b) LPBF and suction-cast alloys

homogenized for 12 h. The solvus temperature of the δ phase is predicted using the Thermo-Calc software TCNI8 database. Cooling rates in the unit of K/s (from 0.1 to 15) are indicated in cooling curves superimposed to the CCT diagram plot. 84

Figure 4-4. (a) AM20m, the LPBF alloy with homogenization for 20 min; (b) AM12h, the LPBF alloy with homogenization for 12 h; (c) AC20m, the suction-cast alloy with homogenization for 20 min; (d) AC12h, the suction-cast with homogenization for 12 h. All the homogenizations are done at 1180°C. Dashed black squiggles profile the NbC carbides. The Nb concentration contour maps are developed using the EDS point identification with a grid size of $10 \times 10 \mu\text{m}$ 87

Figure 4-5. Illustration of the effects of Nb homogeneity in the matrix near the NbC particles on precipitation kinetics of the δ phase (taking alloys AM20m and AM12h as an example). 89

Figure 4-6. Precipitation simulation of the δ phase for the qualitative analysis of Nb homogeneity effects on the CCT diagrams. AM12h and AM20m represent the conditions of low Nb homogeneity and high Nb homogeneity, respectively. 92

Figure 4-7. Vickers hardness testing results of continuously cooled Inconel 718 samples after homogenization at 1180°C with 20 min or 12 h: (a) alloy AM20m; (b) alloy AM12h; (c) alloy AC20m; (d) alloy AC12h. AC means the alloys are prepared using suction casting and AM is noted for the samples prepared by LPBF. 95

Figure 4-8. SEM micrographs on etched Inconel 718 samples cooled at 0.1 K/s: (a) sample AM20m-01; (b) sample AM12h-01; (c) sample AC20m-01; (d) sample AC12h-01. . 96

Figure 5-1. The Inverse Pole Figures (IPF) of the Inconel 718 samples. (a) XY plane, and (b) XZ plane of the as-built sample; (c) XY plane, and (d) XZ plane of sample #H1180

with 1180°C-1 h homogenization; (e) XY plane, and (f) XZ plane of sample #HA1180 with 718°C-10 h aging after 1180°C-1 h homogenization; (g) XY plane, and (h) XZ plane of sample #H1065 with 1065°C-2 h homogenization; (i) XY plane, and (j) XZ plane of sample #HA1065 with 718°C-10 h aging after 1065°C-2 h homogenization. The microstructures of the aged samples are shown in the SEM-BSE micrographs on the right-hand side of figures (e), (f), (i), and (j). The annealing twins in sample #H1180 are shown in Figs. 5-1(c)&(d)..... 101

Figure 5-2. The Grain Orientation Spread (GOS) of the Inconel 718 samples. (a) XY plane, and (b) XZ plane of the as-built sample; (c) XY plane, and (d) XZ plane of sample #H1180 with 1180°C-1 h homogenization; (e) XY plane, and (f) XZ plane of sample #HA1180 with 718°C-10 h aging after 1180°C-1 h homogenization; (g) XY plane, and (h) XZ plane of sample #H1065 with 1065°C-2 h homogenization; (i) XY plane, and (j) XZ plane of sample #HA1065 with 718°C-10 h aging after 1065°C-2 h homogenization. 108

Figure 5-3. Schematic of the single variant γ'' coarsening process under applied stresses. (a) Stress states of the three variants of γ'' under tension in the γ matrix; (b) magnified schematic of the stress states of the γ'' variants; (c) stress states of the unit cell of a Type I γ'' particle. 111

Figure 5-4. TEM analysis for aged alloys at 718°C for 10 h after different homogenizations. (a) Dark field image and (b) selected area electron diffraction pattern of sample #HA1180, which has been homogenized at 1180°C for 1 h; (c) Dark field image and (d) selected area electron diffraction pattern of sample #HA1065, which has been homogenized at 1065°C for 2 h. 112

Figure 5-5. Illustration of the process-structure-property relationships of the LPBF Inconel 718 tensile bars. (a) Demonstration of the vertically and horizontally printed tensile bars; illustration of the relationships between grain morphology and tensile direction for (b) vertical and (c) horizontal tensile bars (taking the as-built samples as examples); (d) engineering yield strength and (e) engineering elongation of horizontal and vertical tensile bars with various heat treatments..... 113

Figure 5-6. Temperature profiles of the heat treatment optimization process. 117

Figure 5-7. Hardness testing results for heat treatment optimization. 118

Figure 5-8. (a) Inverse Pole Figure (IPF) and (b) Grain Orientation Spread (GOS) map of sample HA1180 with 718°C-15 h aging after homogenization of 1180°C-1 h; (c) IPF and (d) GOS map of sample HAA1180 with 718°C-15 h+650°C-10 h after homogenization of 1180°C-1 h. 119

Figure 5-9. SEM images of (a) sample HA1180 with 718°C-15h aging after homogenization of 1180°C-1h; (b) sample HAA1180 with 718°C-15h+650°C-10h after homogenization of 1180°C-1h. 121

Figure 5-10. Brigh-field TEM images of (a) sample HA1180 with 718°C-15 h aging after homogenization of 1180°C-1 h; (b) sample HAA1180 with 718°C-15 h+650°C-10 h after homogenization of 1180°C-1 h..... 122

Figure 5-11. Comparison of the mechanical properties between the optimized heat treatments from this work and other studies in the literature. 124

Figure 6-1. Setup of high-throughput experiments. (a) Inconel 718 build printed by LPBF; (b) setup of temperature record and illustration of sample cutting for microstructure characterization (taking sample HT825 as an example; the sample notations and the

corresponding heat treatment are shown in Fig. 6-2); (c) setup of the furnace for the high-throughput experiment; (d) experimental temperature distribution inside the bar-sample. 126

Figure 6-2. Temperature diagram of heat treatment with the corresponding sample notations used in this work. 128

Figure 6-3. (a) Results of Vickers microhardness and average grain size measurements. IPFs of the aged samples with (b) HT605; (c) HT664; (d) HT716; (e) HT751; (f) HT779; (g) HT798; (h) HT816; (i) HT825..... 130

Figure 6-4. Microstructures of HT605 characterized by (a) SEM-BSE; (b) bright-field TEM; (c) selected-area-electron-diffraction (SAED). Microstructures of HT716 characterized by (d) SEM-BSE; (e) bright-field TEM; (f) SAED. Microstructures of HT825 characterized by (g) SEM-BSE; (h) bright-field TEM; (i) SAED. The different γ'' variants in (f) and (i) are shown by different colors, and the corresponding zone axes are indicated..... 131

Preface

Surely there is a vein for the silver, and a place for gold where they fine it. Iron is taken out of the earth, and brass is molten out of the stone.

—*Job 28:1-2, KJV*

Four years is short even in human life, but its echo speaks and can be long-lasting. It is my greatest fortune to spend the most precious four years pursuing the success of my Ph.D. career at Pitt and shaping the best characters of my life. The study on the heat treatment of Inconel 718 superalloy just resembles every lesson I have been taking since the first day of school. Only through the long-time and high-temperature heat treatment can the Inconel 718 components be strong, and similarly, only through the trial from massive challenges can a man stand firm. Although an alloy having been developed for more than a half-century, when being refabricated by additive manufacturing, Inconel 718 still shows quite different phase transformations and properties from the traditionally manufactured ones. This does remind me that manufacturing life with various novel approaches can always inspire the unknown potential that may be necessary to face new challenges.

However, nothing would I achieve without help from others. Among all the thanks I am eager to send out, I would like to heartily thank my supervisor, Prof. Wei Xiong, firstly. As the first Ph.D. student graduating under his guidance, I received the most of his supervision and mentorship. Never did he refuse to provide even the most detailed advice and support as long as it is beneficial to any of my progress. His great ideas of doing excellent research and being a good person always encourage me to explore more possibilities.

The research in this dissertation is mainly supported by National Aeronautics and Space Administration under the grant numbers of NNX17AD11G and 80NSSC18C0214. The financial funding is much appreciated. I am also much thankful for the valuable suggestions on this dissertation work from my distinguished committee members, Prof. Brian Gleeson, Prof. Albert C. To, Prof. Markus Chmielus, and Prof. Youngjae Chun. Their advice from multiple perspectives further polished the dissertation and made it better. I want to appreciate Dr. Qing Chen at Thermo-Calc Software AB, Sweden, for the discussions about my CALPHAD modeling. Dr. Esta Abelev, Dr. Susheng Tan, Dr. Jun Chen, Dr. Daniel N. Lamont, and Mr. Michael L. McDonald from the Petersen Institute of NanoScience and Engineering (PINSE) at University of Pittsburgh strongly supported most of my training in terms of advanced characterization techniques, and their help is much appreciated. I am grateful for the help from Dr. Bingtao Li on instrument maintenance and from Dr. Qiaofu Zhang on discussions regarding phase transformation. Thanks to Mr. Brandon Blasko for his help on sample printing and cutting as well as other sample preparation work. I am willing to appreciate all the members of the PMMD lab. I value the support much from my good friends, Dr. Soumya Sridar, Mr. Xin Wang, Ms. Liangyan Hao, Mr. Noah A. Sargent, Mr. Rafael Rodriguez, and Mr. Yuankang Wang for their assistance on the work related to my dissertation either on modeling or experiments. More important, their friendship always makes me confident to achieve more progress. All the previous lab members are also highly appreciated as I learned and got help from everyone who had contributed to the construction of this lab.

Last but not least, I would not have achieved this dissertation without the love from my family. My gratitude be to my wife, Dr. Fengxue Zhang, who has obtained her Ph.D. degree several weeks ago prior to me, for her unreserved support in my academic career. The unconditional love from my parents is the source of courage in the course of my life, I am grateful for owning this

every single second. I also want to thank my cute baby, Sebastian, for the joy he has been bringing to us. You may also want to pursue a Ph.D. in twenty years, Seb.

1.0 Introduction

This chapter is partly modified from the following published or submitted journal papers:

1. Y. Zhao, K. Li, M. Gargani, W. Xiong, A comparative analysis of Inconel 718 made by additive manufacturing and suction casting: microstructure evolution in homogenization, *Additive Manufacturing* 36 (2020) 101404 [1].
2. Y. Zhao, F. Meng, C. Liu, S. Tan, W. Xiong, Impact of homogenization on microstructure-property relationships of Inconel 718 alloy prepared by laser powder bed fusion, submitted to *Mater. Sci. Eng. A*.
3. Y. Zhao, L. Hao, Q. Zhang, W. Xiong, Phase transformations during continuous cooling in Inconel 718 alloys manufactured by laser powder bed fusion and suction casting, submitted to *Science and Technology of Advanced Materials*.

1.1 Overview of Inconel 718

Inconel 718 is a Ni-based superalloy that has been widely applied in the aerospace and nuclear industries because of its excellent strength, oxidation, and creep resistance properties at high service temperature [2–4]. The typical chemical composition of Inconel 718 is listed in Table 1-1 [5]. Among the major elements of Inconel 718, the Ni, Fe, and Cr mainly contribute to the formation of the fcc_A1 matrix while Cr also provides oxidation resistance and solid solution hardening to the alloy [6]. The addition of Mo is mainly for improving the solid solution hardening during high-temperature service, whereas the Nb, Ti, and Al can form hardening intermetallic

phases that strengthen the alloy. C is mainly used to promote the formation of carbides, which can pin the grain boundaries and help with refining grain size. The typical precipitation morphologies of Inconel 718 [7] are shown in Fig. 1-1. Inconel 718 has an austenite matrix of γ (fcc_A1) phase and is principally precipitation-hardened by the plate-shaped major strengthening phase γ'' (Ni_3Nb , bct_D0₂₂), and the sphere-shaped minor strengthening phase γ' ($\text{Ni}_3(\text{Al}, \text{Ti}, \text{Nb})$, fcc_L1₂) [8,9]. The γ'' and γ' precipitates distribute in the matrix with nano-size and are coherent or semi-coherent with the γ matrix [10–12], contributing to the strengthening effect of the alloy. The γ'' phase is metastable and will transform into the δ phase after long-time aging at an intermediate temperature range of 650 to 900°C [13–15]. Besides, MC carbides (mainly NbC with a small amount of TiC, fcc_B1) usually form along with the γ matrix during high-temperature annealing above 1000°C. With the proper size and distribution range, the NbC carbide can act as the grain boundary pinning particles to impede grain growth [16–18]. However, coarsened NbC particles can introduce microvoid softening effects with localized stress concentration and crack initiation to reduce grain boundaries strength [19–21]. The δ phase (Ni_3Nb , D0_a) and Laves_C14 phase ($(\text{Ni}, \text{Fe}, \text{Cr})_2(\text{Nb}, \text{Ti}, \text{Mo})$, hexagonal) are the two detrimental intermetallic phases that are often observed in the alloy. The δ phase has a needle shape and usually precipitates along grain boundaries [9,22]. It can pin the grain boundaries to control the grain size but degrades strengthening property due to its incoherent phase boundary with the γ [23]. Laves_C14 phase forms during solidification because of Nb and Mo segregation at grain boundaries. It can cause the initiation and propagation of cracking and is usually removed by homogenization treatment at an elevated temperature due to thermodynamic instability [24,25]. Additionally, it is reported that the σ phase and α -Cr phase can form during long-time exposure with stresses applied [26]. Therefore, they are seldom observed during normal heat treatments.

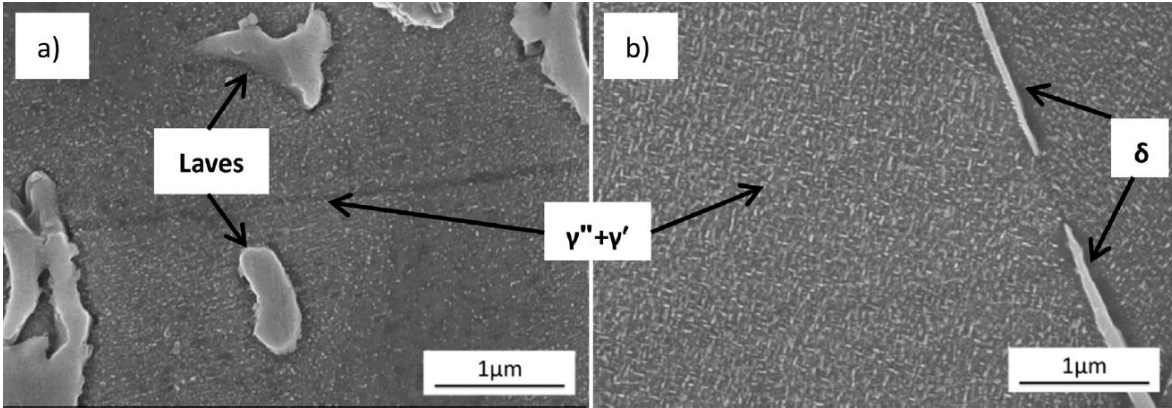


Figure 1-1. Typical precipitate morphologies [7] of (a) Laves_C14, γ'' , and γ' phases in Laser Additively Manufactured Inconel 718 and (b) δ , γ'' , and γ' phases in wrought Inconel 718.

Table 1-1. Typical chemical composition of Inconel 718.

Element	Ni	Fe	Cr	Nb+Ta	Mo	Ti	Al	C
Content, wt.%	50.0-55.0	Bal.	17.0-21.0	4.75-5.5	2.80-3.30	0.65-1.15	0.2-0.8	0.08 max.
Element	Mn	Si	P	S	Cu	Co	B	
Content, wt.%	0.35 max.	0.35 max.	0.015 max.	0.015 max.	0.30 max.	1.0 max.	0.006 max.	

A systems design chart describing the process-structure-property relationships of Inconel 718 alloys prepared by additive manufacturing (AM) is shown in Fig. 1-2, which shows that the post-heat treatments on Inconel 718 can affect the microstructure evolution and will further impact the properties of the materials. The commercial heat treatment strategies for wrought Inconel 718 usually include one homogenization step (sometimes it is also referred to as a *solutionization* step) at a high temperature and two aging steps at moderate temperatures. As summarized in Fig. 1-3 [27–29], the first step of the post-heat treatment is the homogenization heat treatment, which is usually performed between 970°C~1065°C with a holding time of 0.5~2 h. The purpose of the homogenization heat treatment is to dissolve the detrimental precipitates, i.e., the δ phase and the

Laves_C14 phase, formed during casting or wrought processes. Additionally, the dissolution of these phases can release Nb into the γ matrix, which is critical for the precipitation of the strengthening γ'' and γ' phases. The following aging processes consist of two steps (Fig. 1-3). The first aging step is performed at a higher temperature above the second aging step. The aging at 718°C for 8 h is frequently used as the first step, whereas the aging at 760°C for 10 h can be the other choice. The main precipitates formed during the first aging step are the γ'' , γ' , and δ phases. The second aging step is usually performed at 620°C or 650°C for 8 h with the γ'' and γ' strengthening phases precipitating. It is found that two-step aging heat treatment can achieve improved materials strength than the one-step aging process [6]. This is because the second aging step at a lower temperature can change the equilibrium state of the γ matrix, by which fewer strengthening particles can be kept in solution and more precipitates are allowed to form [6].

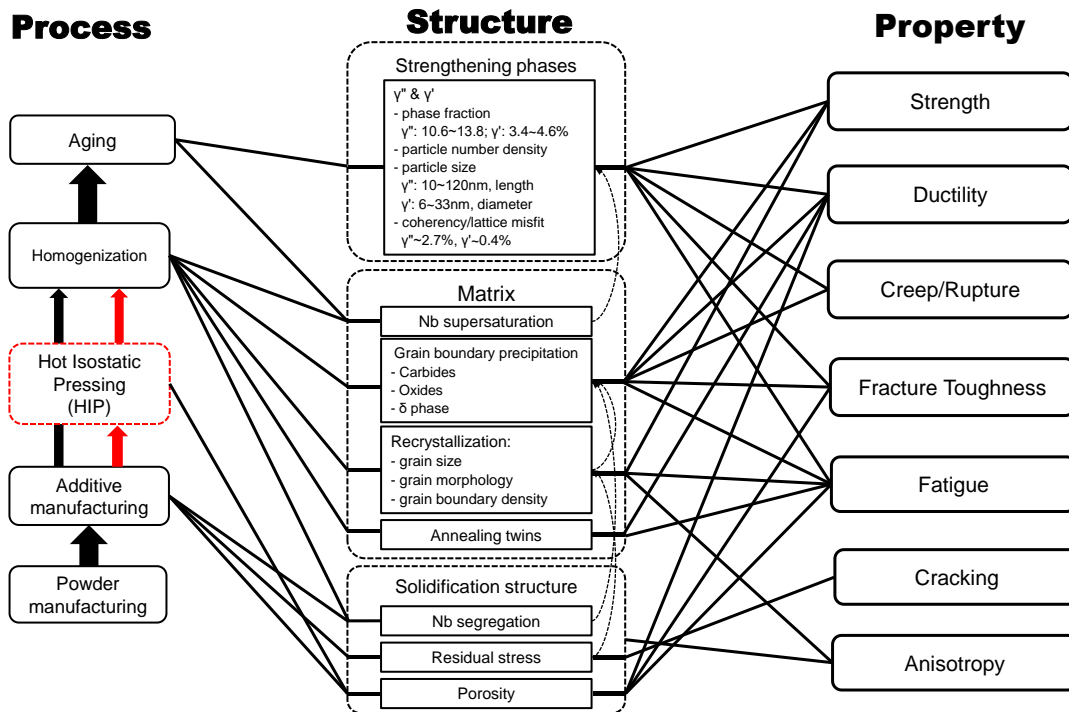


Figure 1-2. Systems design chart of Inconel 718 alloys prepared by additive manufacturing.

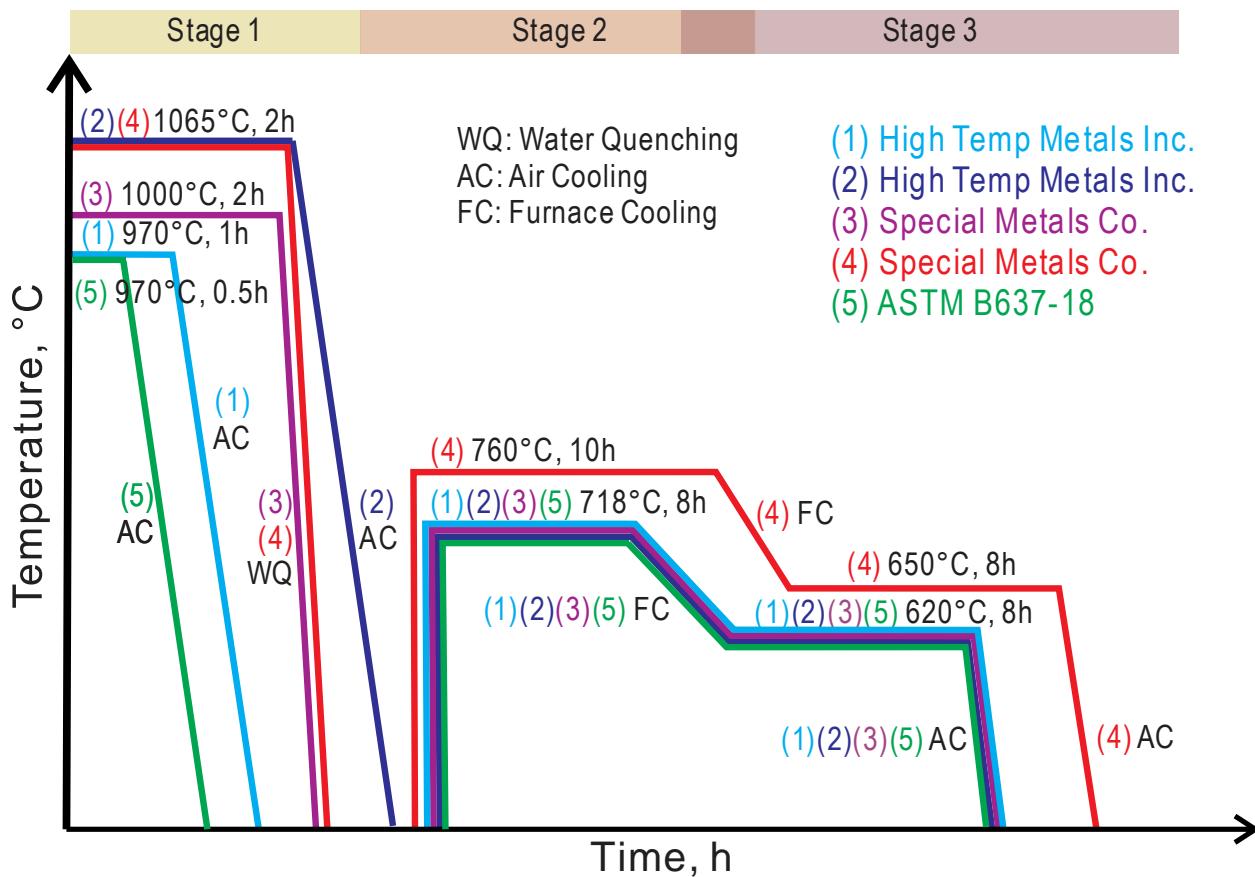


Figure 1-3. Available temperature profiles of heat treatments for the commercial Inconel 718 alloys.

1.2 Additive Manufacturing

In recent years, the application of Inconel 718 in the additive manufacturing communities has proliferated owing to its good printability as well as the increasing demands for high-temperature components with complex shapes [30–32]. Additive manufacturing can build components with complex geometries layer by layer with the assistance of computer-aided design (CAD) [33] and can be divided into two categories based on the materials shaping approaches [34]. The first category uses binder agents to shape components, materials extrusion and binder

jetting are two typical techniques of this category. The other category uses energy sources to directly shape materials. Laser and electron beam are the common energy sources for powder-based AM processes [34–36], while arc frequently serves for wire AM application [37]. As summarized in Fig. 1-4, there are three typical laser powder-based AM methods, i.e., (1) laser sintering (LS), (2) laser melting (LM), and (3) laser metal deposition (LMD).

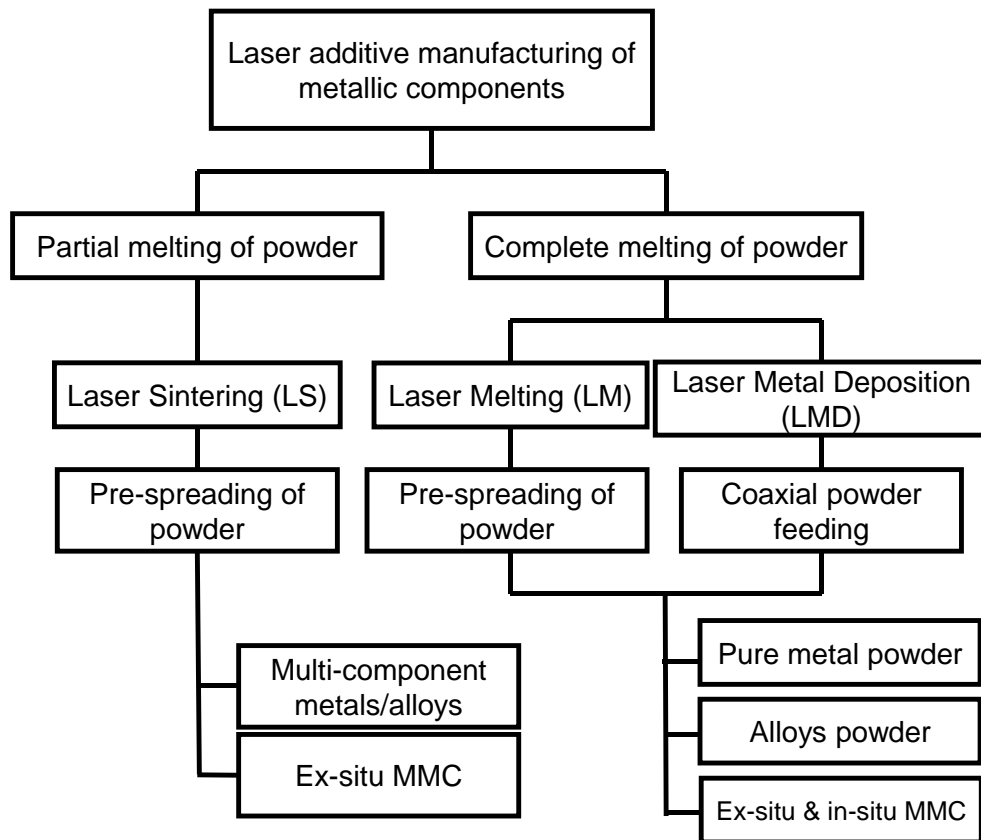


Figure 1-4. Review of laser additive manufacturing methods for metallic components [35].

The LS method manufactures components through the liquid phase sintering mechanism [35], which partially melts the powder bed using a laser beam under a protective inert gas atmosphere. For pure alloy powders, the laser parameters are adjusted to acquire an appropriate

operative temperature between the melting temperatures of the powders. In contrast, for the pre-alloyed powders, the operative temperature is supposed to reside between the liquidus and solidus, which is also named the mushy zone. Once the laser beam scan is finished, a new layer of powder is spread onto the top of the precedent layer for the consecutive scan process, until the whole component is built layer by layer. The LS method, however, has some processing problems, such as incomplete densification caused by the difficulties of controlling the operative temperature during complex thermal profiles. Therefore, post-treatments such as sintering and hot isostatic pressing (HIP) are usually required for the LS-processed builds to improve the properties of the materials.

The LM method has similar printing procedures to the LS method and is more commonly referred to as laser powder bed fusion (LPBF) or selective laser melting (SLM) [38,39]. The illustration of its setup is shown in Fig. 1-5. The powder bed in the LM process experiences complete melting/solidification cycles by the laser beam rather than being densified via liquid sintering. The LM process has higher laser power and smaller focused laser spot size than the LS process [35] and can thus produce components with better densification. Nonetheless, the main shortcoming of the LM process is the accumulation of residual stresses during the multiple melting/solidification cycles [40,41], which can cause the propagation of cracking and can finally lead to failure of the materials. The residual stress is usually mitigated by annealing heat treatment [42].

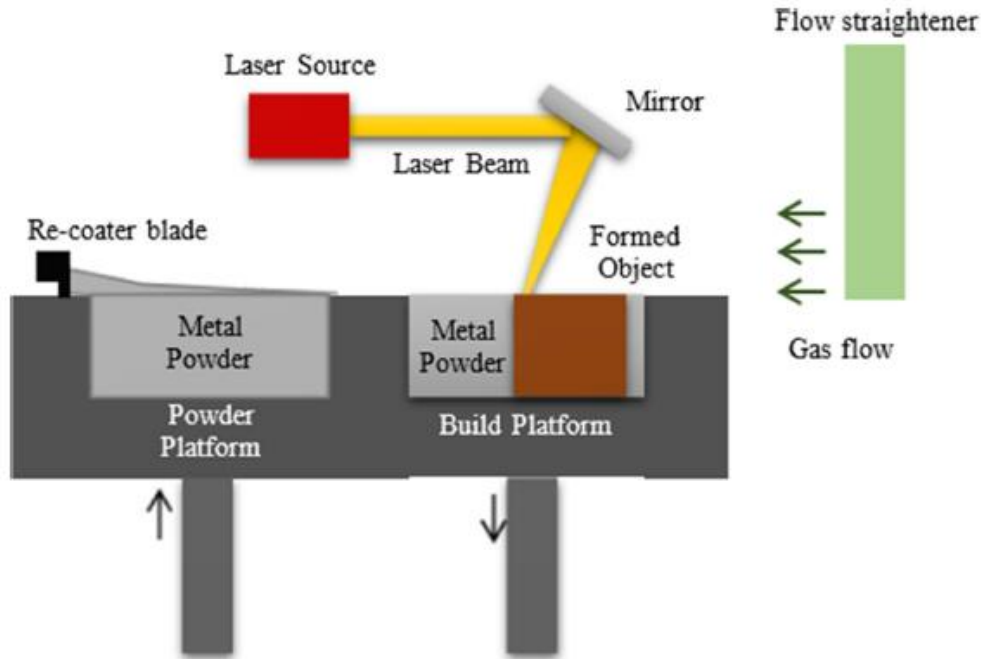


Figure 1-5. Illustration of LPBF setup [34].

In contrast to the LS and LM methods, which use a pre-spread powder bed for powder supplement, the LMD process uses a coaxial powder feeding method during the laser beam scanning. As shown in Fig. 1-6 [43], the powders are ejected from two nozzles; the beams of the powder and the laser are focused on the component, which moves horizontally under the control of a computer to get the components built layer by layer. The LMD method can build components with complex geometries readily, whereas the focusing conditions of the laser and powder beams, the velocity of powder ejection, and the laser power should be delicately optimized for printing a qualified workpiece.

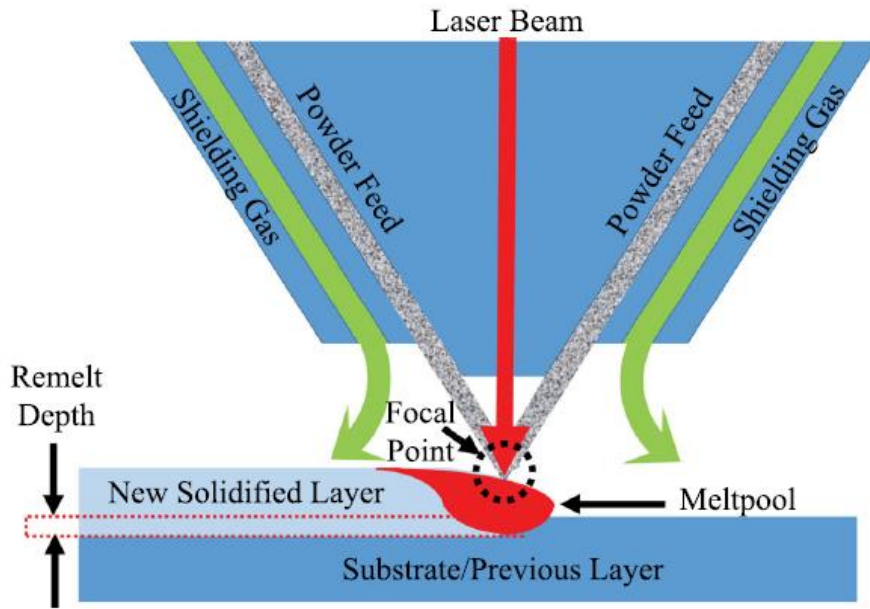


Figure 1-6. Schematic of typical laser metal deposition (LMD) setup [43].

Because the AM method directly produces builds with complex shapes, work hardening is no longer applied to improve the mechanical properties. Therefore, post-heat treatments are critical to controlling the microstructure and property of AM builds, and dedicated investigations should be conducted to understand the heat treatment-microstructure-property relationships. This dissertation will focus on the heat treatment of Inconel 718 builds prepared by the LPBF method. The phase transformations during different heat treatments and the corresponding properties of the material will be investigated.

1.3 State of the Art: Heat Treatment on LPBF Inconel 718

The as-built Inconel 718 alloys usually have some drawbacks, which prevent them from direct application. First, due to the segregation of the elements with low diffusivities, e.g., Nb and

Mo along the grain boundaries, a great amount of Laves_C14 precipitates are introduced during the solidification process, resulting in the degradation of mechanical properties [44]. Besides, the precipitation of the Laves_C14 phase consumes the critical elements consisting of γ'' and γ' phases [45]. For example, Nb is the major component in these precipitates, despite the low Nb content (~ 5 wt.%) in the Inconel 718 alloy. This impedes the formation of these strengthening phases during the subsequent aging processes, resulting in the reduction of strengthening effects of the materials. Second, columnar grains usually develop in the as-built alloys along the build direction Z owing to the thermal gradient induced by the laser melting process [41,46–48]. The difference of grain morphology along different directions in the as-built alloy can cause the anisotropy of mechanical properties [49,50]. Third, the multiple heating and cooling cycles during the LPBF process can generate residual stress, which will promote the initiation of cracking and lead to the failure of materials [51,52]. Qin et al. [53] found that the externally applied stresses would cause the preference of orientation of γ'' precipitation, as shown in Fig. 1-7. Therefore, the γ'' precipitation in the as-built alloy with a high level of residual stress can also have a preferred orientation with increased anisotropy of structure-property relationships.

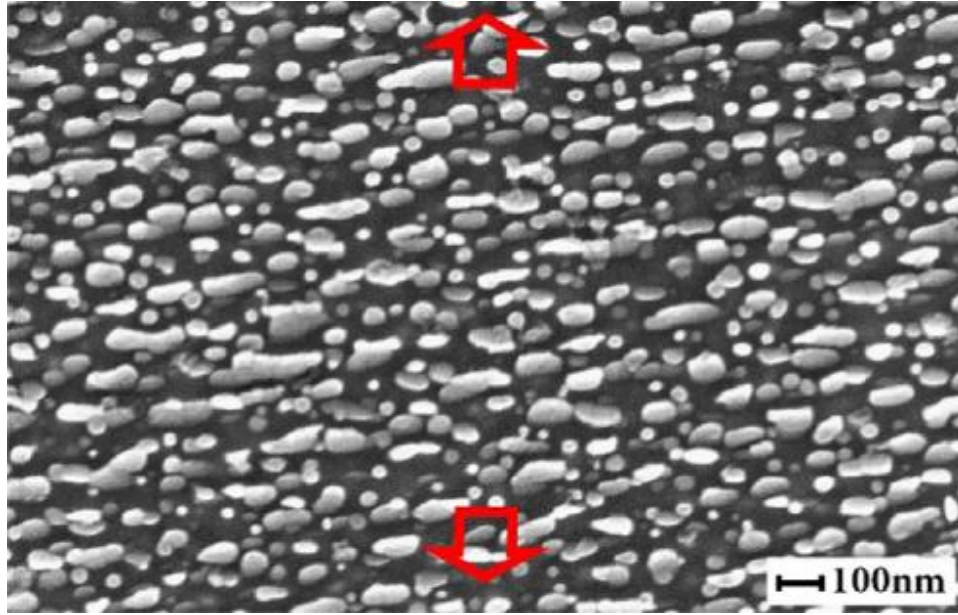


Figure 1-7. Stress-oriented precipitation of γ'' under applied stress in Inconel 718 [53].

Some researchers have reported that the traditional heat treatment methods for the wrought or cast Inconel 718 are not sufficient for the LPBF produced alloys to achieve homogeneous microstructure. Chlebus et al. [3] found that the LPBF samples required a higher homogenization temperature than that prescribed for the wrought or cast Inconel 718 samples, as the traditional homogenization parameters left undissolved Laves phase particles so that the γ matrix was not completely homogenized. Schneider et al. [54] found that the LPBF samples could achieve specified heat-treated wrought mechanical properties with reduced heat treatment steps and determined the recrystallization behavior of the LPBF samples differed from that in the cast samples. Liu et al. [55] reported that an effective temperature to introduce recrystallization in LPBF Inconel 718 is 1100°C, with the residual stresses caused by thermal cycles being the recrystallization driving force. In another paper by Liu et al. [56], they determined that the grain boundary migration and subgrain coalescence are the main mechanisms of recrystallization in LPBF Inconel 718. In addition, the annealing twins formed during the homogenization heat

treatment were also observed to provide nucleation sites for the recrystallized grains. The recrystallization temperature of 1100°C in the LPBF Inconel 718 alloys is higher than the reported recrystallization temperature of 1020°C in the wrought alloys [55]. Similar conclusions were also made in Inconel 625 alloys [57]. This is because the LPBF alloys have a lower deformation degree than the wrought alloys, and they lack the defects like slip bands and shear bands that are often observed in the wrought alloys. Therefore, the recrystallization driving force in LPBF alloys is lower than that in the wrought alloys, leading to a higher temperature required for recrystallization [57]. In consequence, the high-temperature homogenization has thus a chance to reduce and further eliminate the microstructure anisotropy and can improve the mechanical properties. On the contrary, the commonly used homogenization temperature of 1065°C for wrought Inconel 718 alloys cannot effectively introduce recrystallization in the LPBF alloys. The differences between wrought and LPBF Inconel 718 alloys are summarized in Table 1-2.

Table 1-2. Summary of the differences between wrought and LPBF Inconel 718 alloys.

	Wrought Inconel 718	LPBF Inconel 718
Grain morphology	Equiaxial grains	Columnar grains along build direction
Origin of internal stress/strain	Deformation processing	Residual stress
Recrystallization driving force	Defects, e.g., slip bands, shear bands, etc.	Residual stress
Recrystallization temperature	1020°C	1100°C

For the alloys fabricated by AM approaches, in which the builds experience multiple heating and cooling cycles, understanding the microstructure evolution during the continuous cooling process is important for the microstructure control, design, and optimization of post-

processing strategies [23,58–64]. The phase transformations during continuous cooling are usually illustrated by continuous-cooling-transformation (CCT) diagrams. The CCT diagrams have been widely used to study the solid-solid phase transformations in steels of which the phase transformation kinetics is usually fast [65–67]. Therefore, the heat treatment effect such as homogenization conditions on the CCT diagrams in steels is usually not considered. However, due to the relatively slow diffusion in superalloys [68], the homogenization conditions can cause different elemental homogeneity and thus affect the phase transformations during continuous cooling. A few CCT diagrams of Inconel 718 have been previously reported [62,69–71], as summarized in Fig. 1-8. In order to facilitate discussion, we define three characteristics of the CCT curves, as illustrated in Fig. 1-8(a), to describe the phase transformation behaviors: (1) starting temperature of the phase transformation; (2) phase formation range, which is defined as the difference between the starting temperature and ending temperature at one certain cooling rate; and (3) critical cooling rate, below which the phase transformation will happen. Garcia et al. [62] used a dilatometer to investigate the effect of homogenizations at 1180°C for 24, 72, and 90 h on the CCT diagrams of cast Inconel 718 alloys. They found the CCT curves shifted to the slower reaction side, i.e., the right-hand side of the CCT diagram, with increased homogenization durations (Figs. 1-8(b)~(f)), indicating that the homogenization can have a significant effect on the CCT diagrams for Inconel 718. The authors [62] also reported that during cooling after 90 h homogenization, new and small MC carbides formed before the δ phase, which was different from the cases of 24 and 72 h homogenizations. This was explained as the Nb segregation along grain boundaries was reduced after long-time homogenization, which increased the Nb supersaturation within the grains and promoted the formation of MC carbides, but limited δ . However, the formation temperature of the δ phase was determined to be quite high (Fig. 1-8(c)), which is up to

about 1130°C. This temperature is much higher than the reported solvus temperatures of δ from 998.3 to 1027°C obtained from experiments and CALPHAD (calculation of phase diagrams) calculations [26,72–74]. In addition, the γ'' , γ' , Laves_C14 phases were also found to form after continuous cooling, as can be seen in Figs. 1-8(d),(e)&(f). γ'' was determined to precipitate before γ' during cooling. The critical cooling rates for γ'' were 1~10 K/s, depending on the homogenization time (Fig. 1-8(d)). Geng et al. [69] investigated the phase transformation behaviors of γ'' and δ during continuous cooling after homogenization at 1100°C for 1 h in hot-extruded Inconel 718 alloys. The result deviated significantly from the one by Garcia et al. [62] since they determined the γ'' precipitated under very slow cooling rates of 0.1~20 K/min (0.0017~0.33 K/s), while δ formed at cooling rates lower than 5 K/min (0.083 K/s). Slama and Cizeron [70] reported that the δ , γ' , and γ'' phases can precipitate respectively after heat treatment at 990°C for 15 min, as reproduced in Fig. 1-8(d). The critical precipitation cooling rate of the δ phase was determined to be higher than 100 K/s, which is extremely high compared to the values from other work; while for the γ' and γ'' , critical cooling rates were 5 K/s, and 0.2 K/s, respectively. Niang et al. [71] provided a CCT curve for δ measured by differential thermal analysis (DTA) in forged Inconel 718 alloys, the critical cooling rate of δ was evaluated to be about 0.5 K/s (Fig. 1-8(c)). The above discussion indicates that, though some CCT diagrams of Inconel 718 have been reported, the results from different work are inconsistent and depend on different fabrication conditions, such as homogenization conditions. However, the effect from homogenization conditions is not prevalently investigated as many works assume the alloys have been completely homogenized with a certain heat treatment. Moreover, the CCT diagrams of AM Inconel 718 still lack investigation, which can impede the development of post-heat treatment.

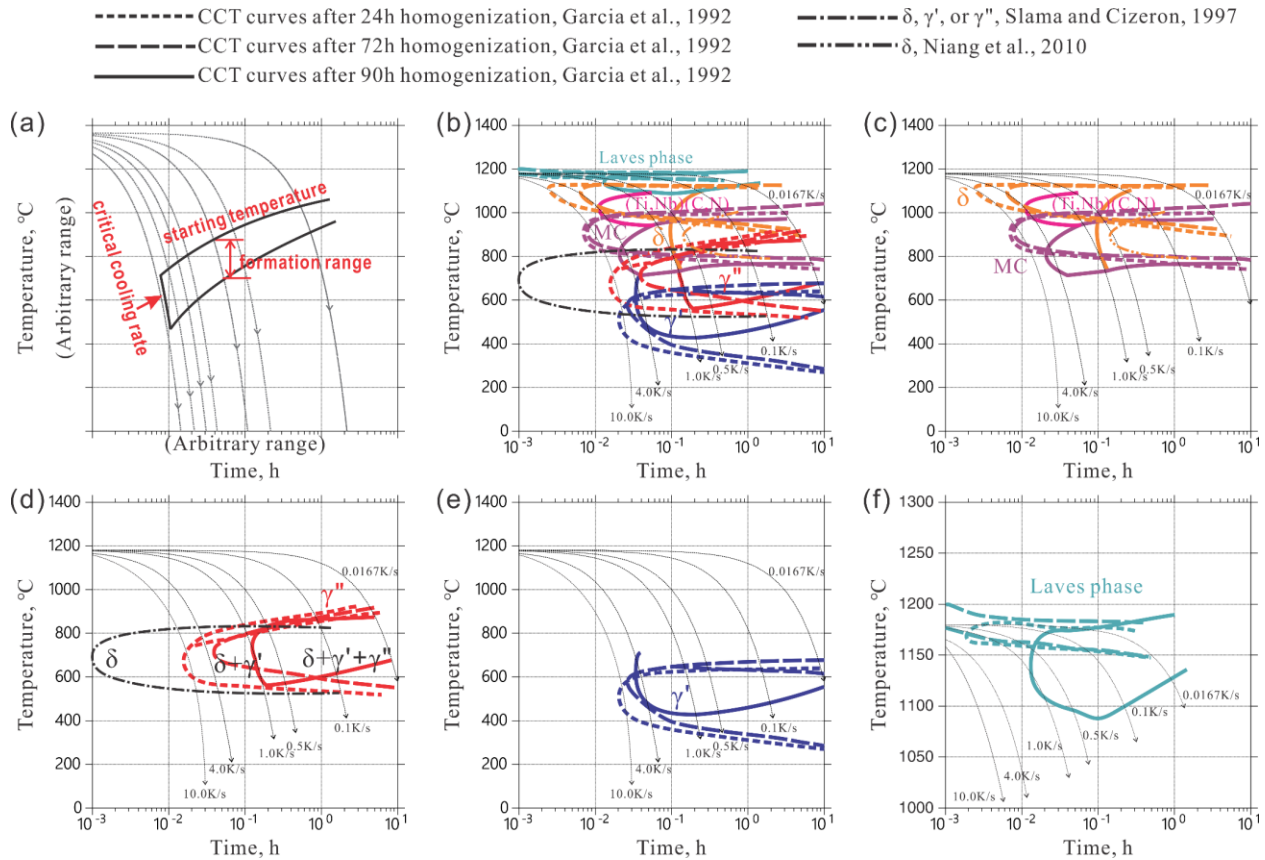


Figure 1-8. (a) Defined characteristics of CCT diagrams in this work: starting temperature, phase formation range, and critical cooling rate; (b) integration of the reported CCT diagram by Garcia et al. [62], Slama and Cizeron [70], and Niang et al. [71]. Individual phases plotted in (b) are shown in the separate plots from (c) to (e) to show each section more clearly; (c) separate plot of the CCT diagram related to the δ phase, carbides, and carbonitrides according to [62,71]; (d) separate plot of the CCT diagrams related to γ'' phase (in red curves) according to Garcia et al. [62] and related to the δ , γ' , or γ'' phases (in black curves) based on Slama and Cizeron [70]; (e) separate plot of the CCT diagram related to the γ' phase according to Garcia et al. [62]; (f) separate plot of the CCT diagram related to the Laves phase according to Garcia et al. [62]. The different line types from Garcia et al. [62] represent the CCT curves determined after various homogenization times.

In the isothermal aging processes, the mainly formed phases are γ'' , γ' , and δ . Tucho and Hansen [75] studied the effects of homogenizations on the phase transformations in LPBF Inconel 718 during aging processes at temperatures from 970°C to 1250°C. They concluded that the

elevated homogenization temperature or the increased holding time will lead to the coarsened γ'' precipitates and will further reduce the hardness of materials after aging. Slama et al. [76] systematically investigated the effect of aging temperature on the microstructure and hardness evolution in hot-rolled Inconel 718 after homogenization and aging processes. They found an aging temperature between 600°C and 650°C could cause an increase of the γ' phase precipitation, and significant precipitation of γ'' occurred during aging between 650°C and 750°C, where a remarkable hardness increase was obtained accordingly. An aging temperature higher than 750°C promoted the precipitation of δ , whereas a reduction of hardness was observed. With the aging times being less than 5 h, the isochronal hardness peaks occurred when an aging temperature of 750°C was applied. As a comparison, when the aging times were longer than 8 h, the peak of hardness happened in aging at 680°C for 50 h, which could produce a hardness value up to 500 HV. The reported work indicated that the aging temperature and time could significantly affect the materials properties. Theska et al. [77] investigated the precipitation in the early stages of the direct aging process in forged Inconel 718. It was found the fine γ' , and γ'' precipitates nucleated homogeneously as spherical particles and remained coherent with the γ matrix during the growth process. The existence of dislocations could promote the pipe diffusion of Nb and accelerated the growth of γ'' . The local changes of the (Al+Ti)/Nb ratio enabled the secondary precipitates to form heterogeneously on the phase boundaries between the γ and the primary particles. Nevertheless, there are few works focusing on the aging processes in the AM Inconel 718 alloys, and the effects of the aging temperature and time on the phase transformations are not well understood. Hence, a comprehensive study on the aging processes in AM Inconel 718 is required, and the difference between the AM and cast/wrought alloys should be clarified.

1.4 Research Motivation

As introduced in Chapter 1.3, although some studies have indicated the necessity of adopting a high-temperature homogenization process to achieve homogeneous microstructure for LPBF Inconel 718, little dedicated research has been conducted to investigate the microstructure evolution in this material during homogenization treatment, leaving the impacts from homogenization on the subsequent heat treatment steps (i.e., the aging process and cooling process) unrevealed. Due to the unique microstructure in the as-built alloy, the phase transformations, particularly the dissolution of Laves_C14 phase and the formation of NbC carbides, the grain morphology evolution, and the residual stress change would be significantly different from those in the cast or wrought alloys, with the underlying physics to be disclosed. This knowledge gap with regards to the homogenization process in LPBF Inconel 718 poses obstacles for the optimization of post-processing. Hence, a systematic study is essential to gain a better insight into microstructure evolution during the homogenization heat treatment for LPBF Inconel 718 alloys.

The cooling process is vital for microstructure control and a thorough study on its influence should be conducted. The discussion in Chapter 1.3 indicates the reported CCT diagrams of Inconel 718 are inconsistent and are correlated with manufacturing conditions. The homogenization condition has been found to be a key factor affecting the CCT diagrams of cast Inconel 718, nevertheless, whether it also causes a similar change in LPBF alloys remains unclear. Moreover, it is intriguing to explore how CCT diagrams of LPBF Inconel 718 deviate from the cast alloys due to the different initial microstructures although given a certain homogenization condition. A related study on such effect is left blank, impeding the heat treatment design of LPBF alloys since the heat treatment design would be based on the reported diagrams of cast Inconel

718. Therefore, a thorough study related to the homogenization and manufacturing effects on phase transformations during continuous cooling processes for Inconel 718 is desirable.

The isothermal aging process plays an important role in material strengthening and should thus be further optimized. Currently, most of the reported aging processes used for LPBF are based on the standard heat treatment developed for wrought or cast alloys. These studies did not consider the possible influence on microstructure change during aging from the different initial microstructure and the homogenization conditions that are suitable for LPBF alloys. Thus, the microstructure evolution in LPBF Inconel 718 during aging affected by homogenization conditions deserves specific investigation, based on which the aging parameters could be further optimized for improving mechanical properties. In addition, it is of interest to develop new high-throughput experiments to accelerating the post-heat treatment design of the LPBF Inconel 718.

2.0 Methodology

2.1 Experiment

Inconel 718 alloys processed by suction casting and LPBF were used for study in this dissertation. The suction-cast Inconel 718 alloys were produced from wrought materials with the composition listed in Table 2-1. Rods of 11 mm diameter and 40 mm length were suction-cast using an arc-melter (ABJ-338 arc-melter, Materials Research Furnaces Inc., USA) with a copper crucible under pure Ar protective atmosphere. Pure Zr was pre-melted before the suction casting to remove the remnant oxygen that may be present in the chamber. The powders used for the LPBF process were manufactured by Praxair Surface Technologies, Inc. with the nominal composition listed in Table 2-1. The d_{10} , d_{50} , and d_{90} particle sizes of the powder were 18.5, 20, and 44 μm , respectively. Inconel 718 alloys were printed using an EOS M 290 machine (EOS company, Germany) with the factory default parameters. The laser power was 285 W, the scan velocity was 960 mm/s, and the hatching space was 0.11 mm. The length of the build was 100 mm, the width of the build was 10 mm, and the height of the build was 45 mm. The samples for microstructure characterization were cut at the middle height locations of the build. An additional investigation in this work revealed that the height of this build did not influence the as-built microstructure and microhardness. The hatch lines between adjacent layers had a rotation angle of 67° . The suction-cast and LPBF alloys were cut into small bulk samples by wire cutting using EDM (electrical discharge machining) machine and were encapsulated into quartz tubes with a backfilled Ar protective atmosphere for heat treatment. Samples were hot-mounted and surface-finished through

metallographic grinding and polishing steps with the final one using a 0.04 μm water-based colloidal silica suspension.

Table 2-1. Nominal compositions of alloying elements in suction-cast alloy and LPBF powders.

wt.%	Fe	Cr	Nb	Mo	Ti	Al	Mn	Co	Cu	Si	C
Suction casting	18.50	18.30	4.99	3.04	1.02	0.55	0.23	0.39	0.07	0.08	0.051
LPBF	18.26	18.87	4.97	2.97	0.94	0.46	0.06	0.23	0.05	0.06	0.03

The microstructure characterizations and mechanical testing conducted in this study are summarized as follows.

Scanning Electron Microscopy (SEM) and Energy-Dispersive X-ray Spectroscopy (EDS):

The SEM characterization was used to determine the microstructure of the material on the surface, and the EDS measurement was carried out for determining the chemical compositions of different phases. Two SEMs were used in this work: the ZEISS-Sigma 500 VP (Carl Zeiss AG) and the FEI Scios Dual-Beam system (FEI Company). The phase morphology determination was performed under the back-scattered electron mode of the SEMs, and the EDS detector (Oxford Instruments plc) was equipped on the ZEISS-Sigma 500 VP. The EDS results were analyzed with Aztec 3.2 software. The SEM and EDS characterizations adopted an accelerating voltage of 30 kV. Phase fractions were estimated by analyzing the SEM images using the ImageJ software package.

Electron Backscatter Diffraction (EBSD):

The EBSD characterization was conducted on the FEI Scios Dual-Beam system to analyze the grain morphology, grain size, grain boundary, and level of residual stress. The accelerating

voltage of EBSD was 20 kV. The EBSD results were analyzed by the OIM Analysis™ v8 software package.

Transmission Electron Microscopy:

High-resolution microstructure characterization was performed on an H-9500 E-TEM (Hitachi, Ltd) with an accelerating voltage of 300 kV. The TEM samples were mechanically thinned to a thickness of 50 μm , and further polished using an automatic twin-jet electropolisher (Model 110, E.A. Fischione Instruments, Inc.) with a voltage of 15 V at -30°C . The electropolishing solution was a mixture of 10 vol.% perchloric acid and 90 vol.% methanol.

X-Ray Diffraction (XRD):

The XRD characterization was used to analyze the phases contained in the alloys. A Bruker D8 X-ray diffraction system (Bruker AXS Inc., Madison, WI, USA) with $\text{Cu K}\alpha$ radiation was used in this work to determine the XRD patterns. The measurements were performed in the 2θ range of $30\text{-}70^{\circ}$ with 0.01° step size and with 0.5 s for each step.

Quenching Dilatometry:

The sample dilatations during continuous cooling processes were measured using a DIL805A quenching dilatometer (TA Company) to determine the phase transformation temperatures at different cooling rates. The dilatometry measurements were conducted under a pure Ar atmosphere to protect the samples from being oxidized.

Microhardness Testing:

The microhardness tests were performed on surface-polished samples using a Leco LM-800 tester under 50 or 100 gf loads with a dwell time of 10 s.

Tensile Testing:

The tensile tests were conducted on an MTS Sintech 20G tensile test machine with a strain rate of $8E-5$ /s, the tensile bars were printed according to the ASTM E8/E8M-16a standard [78].

2.2 Modeling

In this work, the CALPHAD modeling was performed using the Thermo-Calc software package (Thermo-Calc Software AB) to understand the phase equilibria and phase transformations in Inconel 718. The thermodynamic (TCNI8) and mobility (MOBNI4) databases released by the Thermo-Calc AB [79] were adopted in the CALPHAD modeling.

For the thermodynamic calculation, the Thermo-Calc software can predict the phase equilibria by calculating the Gibbs free energy with the given compositions and temperatures. The Gibbs free energy functions of each phase are assessed using thermodynamic models and experimental data. The Gibbs free energy of liquid and solid solution phases are modeled using the solution model, whereas the modeling of Gibbs free energy of the intermetallic phases such as the Laves_C14 phase, δ , and γ'' phases in Inconel 718 uses the sublattice model [80–82]. For a binary system (e.g., A-B), the molar Gibbs free energy of a solid solution phase ϕ can be described as

$$G_m^\phi = \sum_i x_i {}^oG_i^\phi + RT \sum_i x_i \ln x_i + G_{ex}^\phi \quad (2-1)$$

The first term on the right side represents the reference state of the Gibbs free energy and the second term indicates the contribution of the configurational entropy to the Gibbs free energy,

where i is the number of components in ϕ , x_i is the mole fraction of component i , ${}^oG_i^\phi$ is the Gibbs free energy of pure component i in ϕ , R is the gas constant, and T is the temperature. The third term G_{ex}^ϕ is the excess Gibbs free energy of mixing, which can be expressed by Redlich-Kister polynomial [83] as

$$G_{ex}^\phi = x_A x_B \sum_v {}^vL_{A,B} (x_A - x_B)^v \quad (2-2)$$

where x_A and x_B are the mole fraction of components A and B, respectively; ${}^vL_{A,B}$ is the interaction coefficient, and v is the power. It should be noted that if $v = 0$, the model becomes a regular solution model, while when $v = 1$, it becomes a sub-regular solution model. The parameters are optimized by fitting the model with experimental thermodynamic data.

As for an intermetallic phase ϕ , the Gibbs free energy is described by considering the interactions between various sublattices. As the simplest case, i.e., a two-sublattice model of $(A, B)_m(A, B)_n$ gives [84]

$$\begin{aligned} G_m^\phi &= \sum_i \sum_j y'_i y''_j {}^oG_{i,j}^\phi \\ &+ RT \left(\frac{m}{m+n} \sum_i y'_i \ln(y'_i) + \frac{n}{m+n} \sum_i y''_i \ln(y''_i) \right) \\ &+ y'_A y'_B \sum_j y''_j {}^vL_{A,B;j} (y'_A - y'_B)^v \\ &+ y''_A y''_B \sum_j y'_j {}^vL_{i:A,B} (y''_A - y''_B)^v \\ &+ y'_A y'_B y''_A y''_B L_{A,B:A,B} \end{aligned} \quad (2-3)$$

Similar to the expression of the solution model, on the right side of Eq. 2-3, the first term in the expression of the sublattice model represents the reference state of Gibbs free energy, and the second term indicates the contribution of configurational entropy to the Gibbs free energy. The summation of the last three terms is the excess Gibbs free energy. ${}^oG_{i;j}^\phi$ is the Gibbs free energy of the “end members”, which are the stoichiometric compounds that consist of the constituents of each sublattice [85]; m and n are the ratio of sites on each sublattice, y_i' and y_i'' represent the mole fraction of component i in the first and second sublattices, respectively; L are the coefficients of interaction between the sublattices.

After establishing the thermodynamic description of the binary system, one can extend the excess Gibbs free energy model to a higher-order multi-component system, of which the descriptions of excess Gibbs free energy are extrapolated using the geometrical Muggianu method [86]. A more detailed discussion about the models of Gibbs free energy can be found in [87].

The one-dimension kinetic modeling was performed in the diffusion module (DICTRA) [88] implemented in Thermo-Calc using both TCNI8 thermodynamic and MOBNI4 kinetic databases. The DICTRA module was developed to simulate the diffusion-controlled phase transformations in a multicomponent system. In DICTRA, the flux of a component k along the Z direction in the volume-fixed frame of reference is described as

$$J_k = - \sum_{i=1}^n L'_{ki} \frac{\partial \mu_i}{\partial z} \quad (2-4)$$

where $\frac{\partial \mu_i}{\partial z}$ is the chemical potential of component i along the Z direction in the system. L'_{ki} is a matrix of kinetic coefficients and is given by

$$L'_{ki} = \sum_{j=1}^n (\delta_{jk} - c_k V_j) L_{ji} \quad (2-5)$$

where δ_{jk} is the Kronecker delta with $\delta_{jk} = 1$ when $j = k$, and $\delta_{jk} = 0$ otherwise. V_j is the partial molar volume of element j , and c_k is the concentration of k . L_{ji} is a function of the atomic mobility of component k .

Since it is usually more convenient to use the concentration gradient in the expression of flux rather than the chemical potential, the chain rule of derivation is applied to Eq. 2-4 and then gives

$$J_k = - \sum_{i=1}^n L'_{ki} \sum_{j=1}^n \frac{\partial \mu_i}{\partial c_j} \frac{\partial c_j}{\partial z} \quad (2-6)$$

if we rewrite Eq. 2-6 as

$$J_k = - \sum_{i=1}^n D_{kj} \frac{\partial c_j}{\partial z} \quad (2-7)$$

by comparing Eq. 2-6 and Eq. 2-7, one can get

$$D_{kj} = \sum_{i=1}^n L'_{ki} \frac{\partial \mu_i}{\partial c_j} \quad (2-8)$$

here D_{kj} is the matrix of chemical diffusivity of element k . Because L'_{ki} is related to the atomic mobility of k and $\frac{\partial \mu_i}{\partial c_j}$ is a thermodynamic factor; the diffusivity in DICTRA is, therefore, consisted of one thermodynamic part and one kinetic part. In the MOBNI4 database, the atomic mobilities assessed by experimental data are stored to reduce the number of parameters in the database. Hence, when performing the kinetic simulation, the mobility and thermodynamic factors from both kinetic and thermodynamic databases will be invoked by DICTRA to generate the matrix of chemical diffusivity D_{kj} and the description of the flux J_k can be readily obtained from Eq. 2-7. As a result, the concentration changes of component k for the time and distance can be solved according to Fick's second law

$$\frac{\partial c_k}{\partial t} = \frac{\partial}{\partial z} (-J_k) \quad (2-9)$$

A more detailed and comprehensive discussion about the diffusivity theory employed in DICTRA can be found in the work of Andersson and Ågren [89].

The phase precipitation simulation was performed on the TC-PRISMA [90] precipitation module. The TC-PRISMA module was developed based on the Langer-Schwartz (LS) model and is implemented in the Thermo-Calc software. It uses the Kampmann-Wagner numerical (KWN) model, which is a modification and extension of the LS model, to predict phase transformation attributes such as particle size, phase fraction, number density as a function of time during concomitant precipitation processes including nucleation, growth, and coarsening. The parameters needed for the TC-PRISMA simulation are invoked from the thermodynamic and kinetic database. Additionally, experimentally measured parameters, e.g., the interfacial energy between two phases, the morphology factors of precipitates, and the elastic parameters can also be input in the

precipitation simulation for non-spherical particles for improved prediction. Details of the theoretical models and software functions of TC-PRISMA are introduced in ref. [90].

2.3 Summary of Methodology

Table 2-2. Summary of methodology in this dissertation.

Alloy Preparation	Process	Variables	Models	Measurements
		As-received		
Suction-cast LPBF	Homogenization	Homogenization (1180°C-20 min 1180°C-1 h 1180°C-12 h)	Thermo-Calc DICTRA	XRD, SEM/EDS, EBSD, TEM
Suction-cast LPBF	Continuous Cooling	Homogenization (1180°C-20 min or 12 h) Continuous Cooling (0.1, 1, 2, 5, 7, 10, 15 K/s)	Classical nucleation & growth theory TC-PRISMA	Dilatometry, SEM, Hardness
LPBF	Aging	1180°C-1 h+718°C-10 h 1065°C-2 h+718°C-10 h	-	SEM, EBSD, TEM, Tensile tests
LPBF	Heat treatment optimization	1180°C-1 h+718°C-15 h+650°C-10 h	-	SEM, EBSD, TEM, Hardness, Tensile tests
LPBF	High-throughput experiment	1180°C-1 h with multiple aging	-	SEM, EBSD, TEM, Hardness

Table 2-2 is the summary demonstrating the methodology of this dissertation. The processes of homogenization, continuous cooling, and aging were investigated. The microstructure evolution during various homogenizations (1180°C for 20 min, 1 h, and 12 h) in both suction-cast

and LPBF alloys was studied. The Thermodynamic modeling performed by Thermo-Calc and kinetic modeling performed by DICTRA were conducted to guide the experimental design of homogenization time under a certain temperature, whereas it was not intended to achieve an accurate prediction of the homogenization time. The experimental results of elemental segregation, phase fraction, and grain morphology obtained through SEM, EDS, and EBSD were used as inputs for the DICTRA simulation and were analyzed to understand the microstructure evolution of the alloys during homogenization. XRD was used to identify the phases in the as-received alloys. TEM characterization was conducted to analyze the Zener pinning effects and dislocation behaviors. The study on the homogenization process will be discussed in Chapter 3.0.

The effects of the homogenized microstructure on the microstructure evolution during continuous cooling were further investigated, as demonstrated in Table 2-2. Two homogenizations (1180°C for 20 min or 12 h) were applied on both the suction-cast and LPBF alloys followed by multiple continuous cooling processes (with cooling rates of 0.1, 1, 2, 5, 7, 10, 15 K/s) to explore the effects of homogenization conditions and manufacturing methods on the microstructure evolution during continuous cooling. Dilatometer and SEM were used to determine the CCT diagrams for the alloys with different homogenization conditions. The precipitation kinetics during continuous cooling was further analyzed with the assistance of classical nucleation and growth theory as well as TC-PRISMA simulation. A specific study on the phase transformations during continuous cooling processes will be provided in Chapter 4.0.

Additionally, the microstructure evolution of the LPBF alloy during the aging process was found to be impacted by homogenization and the influence was studied through microstructure characterization and mechanical testing. The homogenizations of 1180°C-1 h and 1065°C-2 h were performed on the alloys with the same subsequent single-step aging of 718°C-10 h to explore the

homogenization effect on the microstructure and property of aged alloys. The SEM, TEM, and EBSD characterizations served for the phase transformation and grain morphology analysis and the mechanical testing provided the understanding with regards to the process-structure-property relationships. An optimized heat treatment strategy (1180°C-1 h+718°C-15 h+650°C-10 h) was proposed according to the research on homogenization and the aging process, and the mechanical properties of the alloys were measured. Moreover, a high-throughput experiment was developed to accelerate the heat treatment optimization for LPBF alloys. Detailed discussions about the aging process will be shown in Chapters 5.0 and 6.0.

3.0 Study on Homogenization Process Assisted by DICTRA Simulation

This chapter is modified from the following published journal papers:

1. Y. Zhao, K. Li, M. Gargani, W. Xiong, A comparative analysis of Inconel 718 made by additive manufacturing and suction casting: microstructure evolution in homogenization, *Additive Manufacturing* 36 (2020) 101404 [1].
2. S. Sridar, Y. Zhao, W. Xiong, Phase transformations during homogenization of Inconel 718 alloy fabricated by suction casting and laser powder bed fusion: a CALPHAD case study evaluating different homogenization models, *J. Phase Equilib. Diffus.* 42 (2021) 28–41 [91].

As discussed in Chapter 1, the Laves_C14 phase with a high Nb segregation degree formed during the LPBF process can increase the cracking initiation probability and consume the critical element of Nb for forming strengthening phases, i.e., γ'' and γ' . Hence, an effective homogenization process is critical to dissolve the Laves_C14 phase and release the beneficial elements into the γ matrix.

The common practices for developing the optimum parameters of homogenization for either newly developed or existing alloys processed using new fabrication techniques is often trial and error method, or employing a past practice followed for alloys of similar composition processed using existed manufacturing methods. However, both methods lack efficiency. Computational techniques are found to be beneficial in reducing the number of attempts required for optimizing the parameters for homogenization heat treatment. Jablonski and Cowen [68] have reported that DICTRA simulation can be used for homogenization design by predicting the

segregation degree as a function of time. In their work, the segregation across the dendrite arm during the solidification of Nimonic 105 alloy was obtained computationally using the non-equilibrium Scheil simulations. The composition profiles of the segregated species were used as inputs for the DICTRA simulations. With the results obtained from the DICTRA simulations, a two-step homogenization heat treatment was designed and applied to homogenize the Nimonic 105 successfully [68].

Few computational studies have been conducted, however, on Inconel 718 alloys to investigate the dissolution kinetics of the Laves_C14 phase, especially for the alloys fabricated by LPBF. Moreover, although some authors [54,92–96] have indicated through experiments that a high-temperature homogenization is required to improve mechanical properties of AM Inconel 718 alloys, a systematic experimental investigation on the microstructure evolution during the high-temperature homogenization is still lacking, which impedes the further improvement of the homogenization heat treatment.

In this chapter, three different models to estimate the dissolution kinetics of the Laves_C14 phase into the γ matrix in Inconel 718 alloys produced by LPBF are discussed and compared with experimental observations. The main goal of the kinetic simulation is to guide the experimental design and to evaluate the applicability of the modeling using DICTRA. Microstructure evolution at high-temperature homogenization, including phase transformations, and the evolution of grain morphology, residual stress, and dislocation behaviors were studied experimentally by materials characterization. It is noteworthy that alloys under the LPBF process experience multiple cyclic heating and cooling cycles with different heating/cooling rates depending on the laser scanning pattern, while regular casting typically has one single melting and cooling for sample preparation. Suction casting can be regarded as an extreme case of the casting methods, as it can produce

solidification rates at the order of $10^2\sim 10^4$ K/s [97,98], which are much faster than those of the traditional casting methods (0.1~0.01 K/s) [99]. It can also refine the microstructure and extend the solid solubility [100]. Nevertheless, the LPBF-processed alloys have a much faster solidification rate at a magnitude of 10^6 K/s [101] than the suction-cast alloys. Consequently, it is interesting to compare the microstructure evolution between the extreme casting case, i.e., the suction casting and the LPBF method, and it is conducive to achieve a better understanding of the uniqueness of microstructure evolution in the LPBF samples. Hence, suction-cast alloys are used as a reference for comparison in this work.

3.1 Homogenization Kinetics for Inconel 718 Alloys

3.1.1 Microstructure Characterization of As-fabricated Inconel 718 Alloys

Microstructure characterization of as-cast and as-built Inconel 718 alloys was firstly performed to understand their initial microstructures and was adopted as the basis of the kinetic simulations. The X-ray diffractograms for the as-cast and as-built Inconel 718 samples are shown in Fig. 3-1. The as-cast sample consists of Laves_C14 and NbC phases in the γ matrix. On the other hand, the as-built sample comprises the Laves_C14 phase along with the γ matrix whereas NbC is not observable. Figure 3-2 shows a comparison of the microstructure between the as-cast and as-built samples. The as-cast sample shows the presence of blocky NbC phase and irregular Laves_C14 phase dispersed in the γ matrix (Fig. 3-2(a)). These secondary phases were found to form as co-existing precipitates, predominantly along the grain boundaries. In the as-built Inconel 718 sample, Laves_C14 phase was observed as shown in Fig. 3-2(b). It was found to form along

the boundaries of columnar and cellular subgrains due to the segregation of Nb. NbC cannot be observed in the as-built alloys. Although a slight carbon loss was found in a high carbon steel [102] processed by selective laser melting, it was not reported in the study on Inconel 718. In addition, as will be discussed in Chapter 3.2.1, the NbC can precipitate during the long-time homogenization, and its phase fraction is close to the equilibrium phase fraction predicted by thermodynamic modeling using the carbon composition from commercial Inconel 718 alloy. Therefore, it is reasonable to conclude that the carbon loss is not the reason causing the missing NbC, whereas it is the fast solidification rate during the LPBF process that suppressed its precipitation in the as-built alloys. Besides, little amount of oxides can be found in neither the suction-cast nor the LPBF alloys. Moreover, the grains formed during the solidification were found to be equiaxed with a diameter in the range of 10-20 μm for the as-cast sample, whereas, large columnar grains consisting of fine columnar subgrains of $\sim 1 \mu\text{m}$ width and cellular subgrains of $\sim 2 \mu\text{m}$ diameter were observed in the as-built sample. The phase evolution in both as-cast and as-built samples observed under SEM correlates well with the phases determined using XRD.

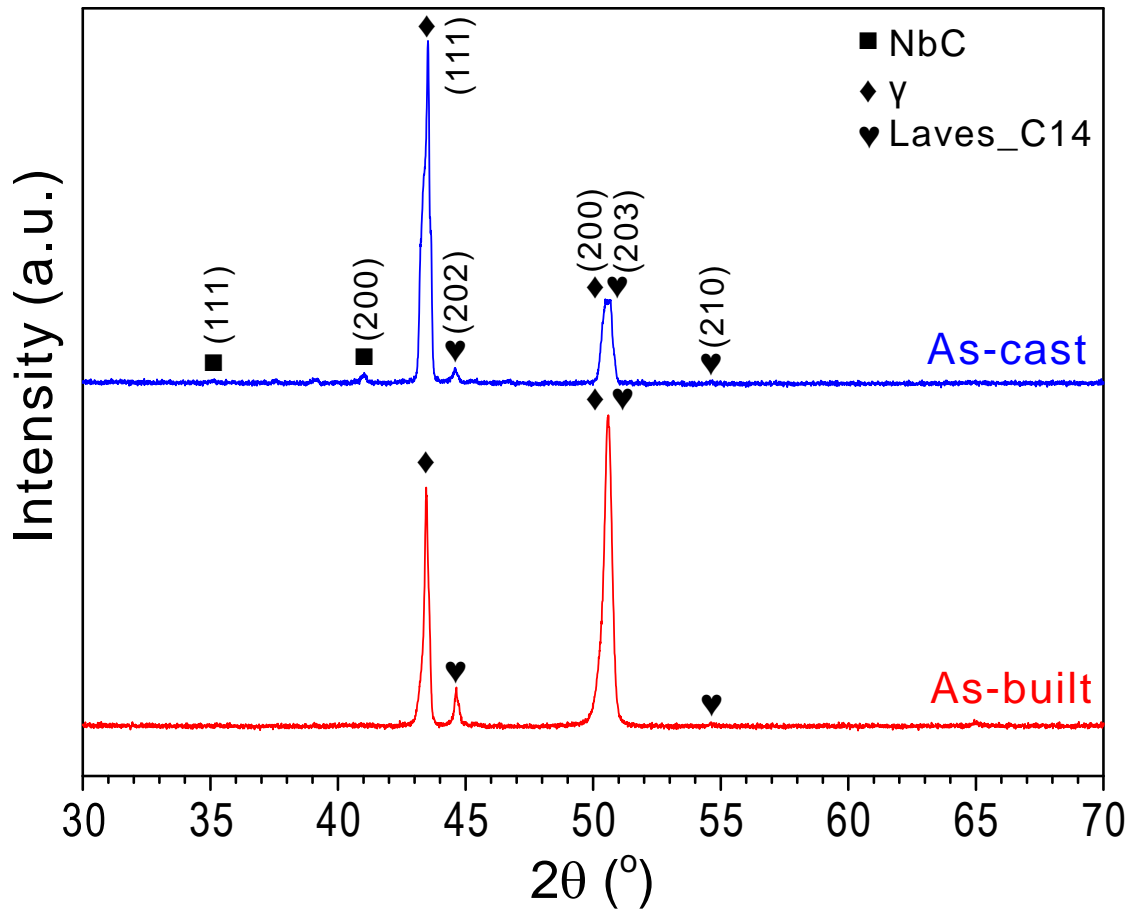


Figure 3-1. X-ray diffractograms for as-cast and as-built Inconel 718 alloys.

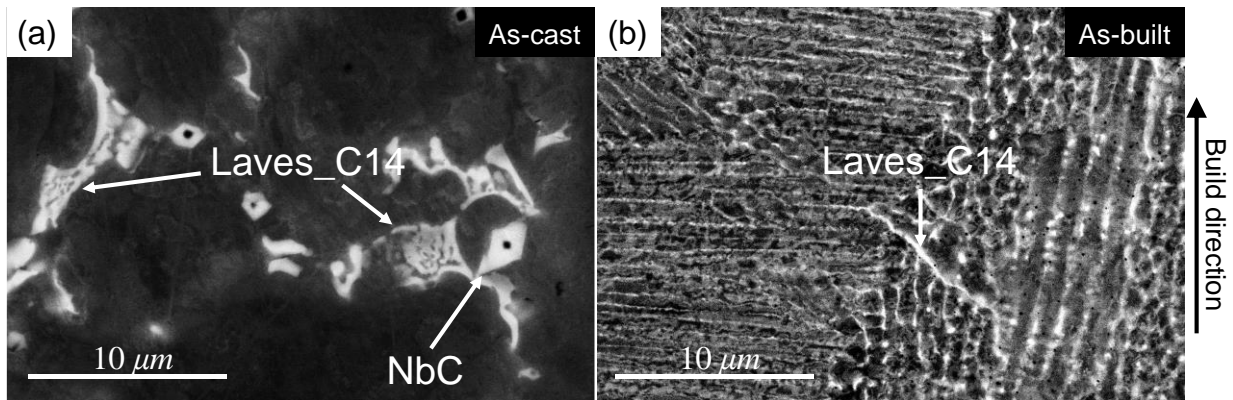


Figure 3-2. SEM-BSE micrographs of (a) as-cast and (b) as-built Inconel 718 alloys.

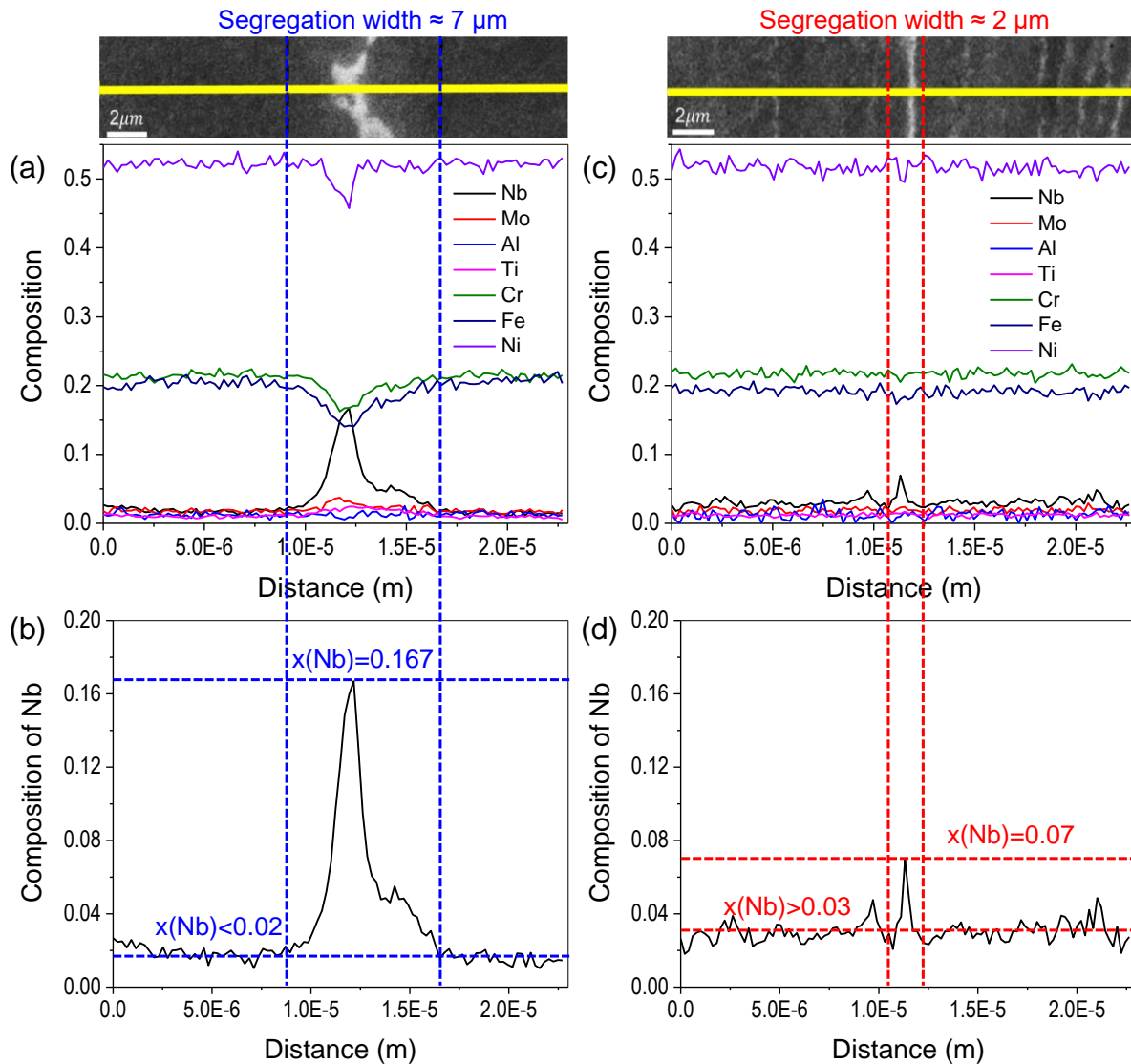


Figure 3-3. Composition profiles (mole fraction) obtained using EDS in as-cast Inconel 718 alloy for (a) all alloying elements and (b) Nb; as well as the as-built Inconel 718 alloy for (c) all alloying elements and (d) Nb.

The composition profiles obtained by performing EDS line scan across a region in the γ matrix with the Laves_C14 phase in as-cast and as-built Inconel 718 samples are shown in Fig. 3-3. For each alloy, several line scans were performed from different locations within the samples and the scans with the highest Nb segregation of each alloy are shown in Fig. 3-3 as representatives. It is evident that the Laves_C14 is enriched with Nb, accompanied by the

maximum segregation of Nb in that location. The composition profile of Nb crossing phase boundaries in as-cast and as-built states are shown in Figs. 3-3(b)&(d), respectively. It was found that the composition of Nb in the Laves_C14 of the as-cast sample is more than two times higher than that of the as-built sample. On the contrary, the Nb concentration in the γ matrix of the as-built sample is slightly higher in comparison with the as-cast Inconel 718 alloy. Moreover, the width of the segregation region is found to be nearly 7 μm and 2 μm for the as-cast and as-built Inconel 718 alloys, respectively. This can be attributed to the fast solidification during the LPBF process leading to high velocity of the solid-liquid interface resulting in the solute trapping effect [59]. This ensures better homogeneity of the γ matrix in the as-built Inconel 718 alloys in comparison with the as-cast sample. These composition profiles serve as useful inputs for the kinetic simulations using DICTRA to predict the homogenization time.

3.1.2 Kinetic Simulations Using DICTRA

Table 3-1. Compositions (in at.%) of the cast and LPBF Inconel 718 alloys measured using EDS.

Processing route	Composition (at.%)						
	Al	Ti	Cr	Fe	Ni	Nb	Mo
Cast	0.55	1.02	18.3	18.5	Bal.	4.99	3.04
LPBF	0.46	0.94	18.87	18.26	Bal.	4.97	2.97

The compositions of Inconel 718 alloys to be used in the simulations for two manufacturing processes were determined using EDS and are listed in Table 3-1. The alloy processed by LPBF was labeled as “AM”. The compositions were obtained from a large-area scan to ensure accuracy. The thermodynamic calculations were carried out using the Thermo-Calc software with the TCNI8 database developed for Ni-base alloys. In addition, the non-equilibrium Scheil-Gulliver [103,104]

model as implemented in the Scheil module of Thermo-Calc software was used to predict the solidification paths as well as the segregation profiles required as inputs for Model 2 as will be described in Section 3.1.2.2. The assumptions in the Scheil-Gulliver model are infinitely fast diffusion in the liquid phase and negligible diffusion in solid that forms from the liquid phase during solidification. As carbon is an interstitial atom, its back-diffusion was considered in this calculation [105].

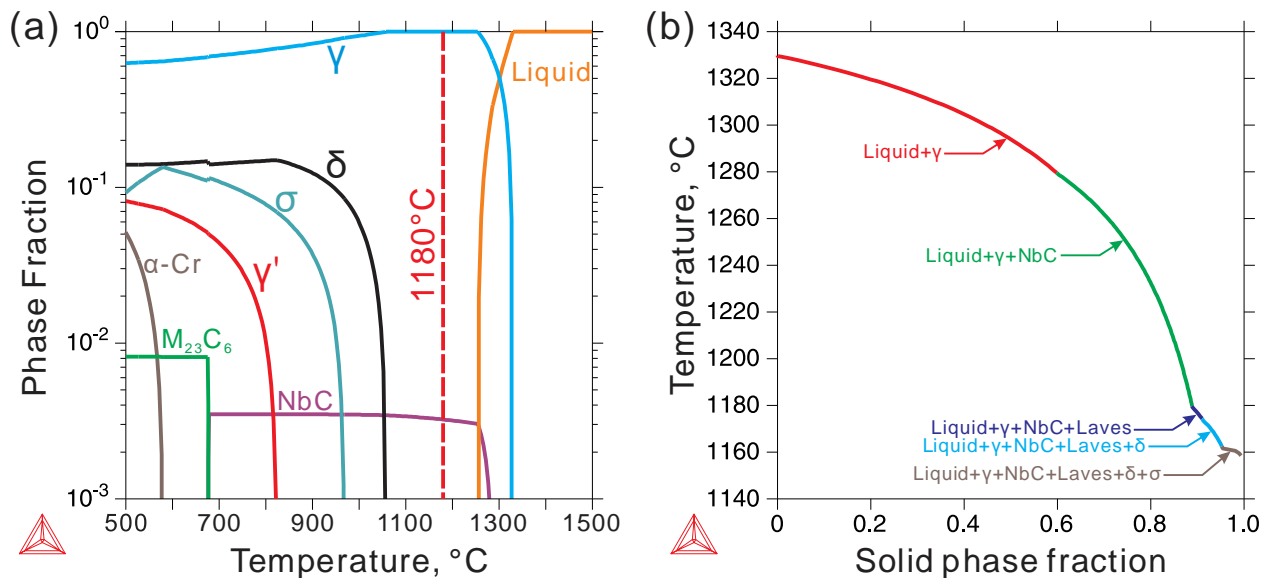


Figure 3-4. (a) Equilibrium phase fraction as a function of temperature and (b) Scheil solidification diagram for the composition of cast Inconel 718 measured using EDS.

The equilibrium phase fraction as a function of temperature and the Scheil solidification diagram for the cast Inconel 718 alloys using the composition determined by EDS are shown in Fig. 3-4. It is worth noting that the carbon content cannot be measured accurately from EDS, thus the content of 0.169 at.% carbon (equivalent to 0.035 wt.% of the commercial Inconel 718 alloys) was assumed in the calculation to include the phase transformations involving carbon. Since the composition of the cast and LPBF Inconel 718 alloys are similar, only the calculated results for

cast Inconel 718 are given in Fig. 3-4. It should be noted that considering the model simplification with infinite diffusion in liquid and no diffusion in solid phases, the predicted incipient point of 1160°C by Scheil-Gulliver modeling is slightly lower than the experimental value of 1165°C, which was reported for the as-cast samples [106]. Such a difference is acceptable by considering the approximation applied in the Scheil simulation. In order to achieve the homogeneity more effectively, a temperature lower than the solidus shown in Fig. 3-4(a) but higher than the incipient melting point, i.e., 1180°C, shown in Fig. 3-4(b) is chosen. It is anticipated that this will ensure complete dissolution of detrimental phases such as δ and Laves_C14. Moreover, though the equilibrium phase fraction plot and Scheil solidification path predict the formation of δ and σ phases in Inconel 718, neither of them were found to form in the as-cast and as-built alloys, as discussed in Chapter 3.1.1.

In order to predict the homogenization time, i.e., the dissolution time of the Laves_C14 phase, for the suction-cast and LPBF Inconel 718 superalloys to guide the experimental design, kinetic simulations were performed. DICTRA module of the Thermo-Calc software was used for this purpose. The thermodynamic and mobility databases used for these calculations were TCNI8 and MOBNI4, respectively. DICTRA module can simulate the kinetics of diffusion-controlled phase transformations. Many studies have confirmed that the dissolution of the Laves_C14 phase in Ni-based superalloys is a diffusion-controlled process [24,25,107,108], though another work also indicated the importance of interfacial reaction when the Nb segregation becomes lower during the dissolution process [109]. In the present work, rather than pursuing an accurate prediction about the dissolution time of Laves_C14 phase, the main purpose of the simulation is to provide a guidance for the experimental design and to evaluate the applicability of different DICTRA models for describing the homogenization process. Therefore, it is rational to assume

the dissolution process of the Laves_C14 phase in Inconel 718 is diffusion-controlled and the dissolution process can be reasonably described by the DICTRA simulation. Three different models have been tested in this study to predict the homogenization time required to dissolve the Laves_C14 phase into the γ matrix and attain homogeneity in suction-cast and LPBF Inconel 718 samples at 1180°C, as shown in Fig. 3-5. Two types of DICTRA calculations were performed as shown in Fig. 3-5(a). In the first type, the single-phase γ matrix was used with variation in composition obtained either from experiments (Model 1), the lever rule calculations (Model 1), or non-equilibrium Scheil simulations (Model 2). In the other type of simulation, a two-phase setup (γ +Laves_C14) with a moving boundary (Model 3) was considered. A detailed description of each model can be found in Sections 3.1.2.1-3.1.2.3.

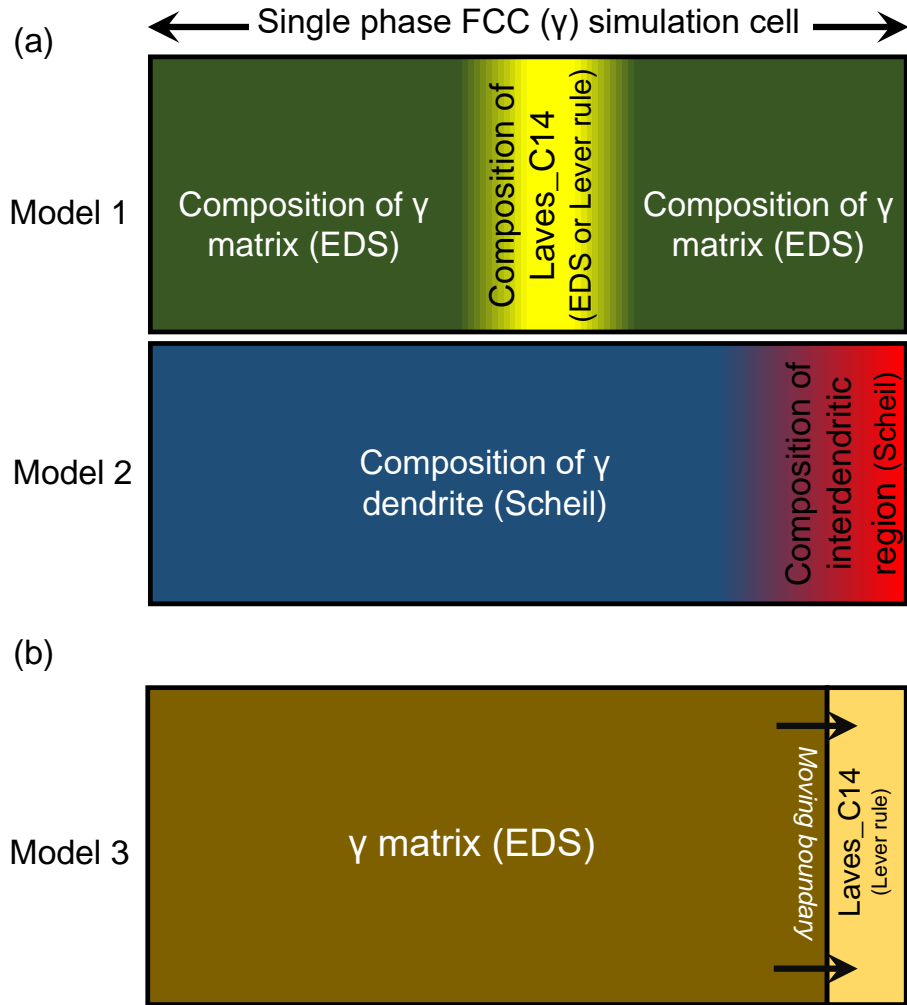


Figure 3-5. Schematic illustration of the simulation setup used for estimating the homogenization time in the suction-cast and LPBF Inconel 718 alloys (a) Single-phase simulations using the composition of Laves_C14 phase from experiments or the lever rule and composition of γ from experiments (Model 1) as well as segregation profiles obtained from Scheil simulations (Model 2) and (b) moving boundary simulations with the composition of γ from experiments and composition of Laves_C14 phase from the lever rule (Model 3).

3.1.2.1 Model 1: Single-Phase Simulations with Laves Phase Composition from the EDS or Lever Rule

Since the mobility data for the Laves_C14 phase is not available in the current commercial mobility database for Ni-based superalloys, the dissolution of the Laves_C14 phase was modeled as a homogenization process within the single-phase γ matrix. Therefore, the simulation cell was assigned with the γ matrix only, rather than a two-phase (γ +Laves_C14) setup. The maximum inhomogeneity in composition was found in the region of the matrix with the Laves_C14 phase present, and hence, it was considered for predicting the homogenization time in the as-cast and as-built Inconel 718 samples. EDS line scans performed in the region of the Laves_C14 phase with the highest Nb segregation in the as-cast and as-built samples were used as inputs for these calculations. Since the phase fraction of Laves_C14 is low in both as-cast (13.1%) and as-built (6.5%) alloys, the EDS line scan can capture the elemental microsegregation tendency across the Laves_C14 particles. The simulations were performed for 10^5 seconds with 113 grid points for the LPBF alloy and 100 grid points for the cast alloy based on the EDS line scan results. Additional inputs such as the width of the simulation cell, the position of grid points within the cell, and the composition at each grid point were adopted from the EDS line scan.

The liquid phase was excluded in the simulation because the formation of liquid is limited by its instability at 1180°C, and the incipient melting could be surpassed by the fast dissolution of the Laves_C14 phase with lower Nb segregation into the γ matrix [96]. More importantly, no evidence of liquation was observed experimentally in the homogenized microstructures, which will be discussed later in detail (Section 3.1.3). This confirms that excluding the liquid phase in the simulation is a reasonable assumption. Since the formation of the Laves_C14 phase is promoted by the segregation of Nb along the grain boundaries, its content determined in the

Laves_C14 phase region was treated the same as Nb concentration segregated in the γ matrix in the simulation. Such a simplification is a compromise to the missing mobility data of Laves_C14 and can make the results deviate from the actual microstructure observed experimentally. However, it still provides a valuable insight to guide the design of the homogenization process. Therefore, the concentration profiles determined by EDS crossing the Laves_C14 phase in the γ matrix (Figs. 3-3(a)&(c)) were considered as the inputs for the DICTRA simulations for cast and LPBF alloys. The variation in the composition of Nb as a function of time at the locations with maximum Nb segregation in the cast and LPBF alloys is shown in Fig. 3-6. According to the DICTRA simulations performed using this approach, the estimated time for the as-built sample to reach a complete homogenization is 200 s, while 2500 s is required for the as-cast Inconel 718 alloy.

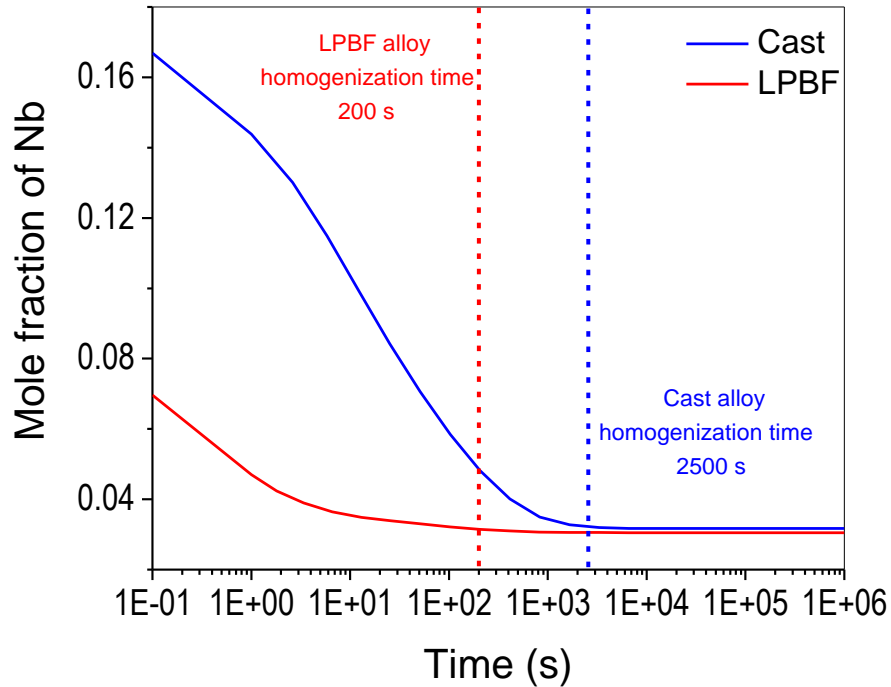


Figure 3-6. Variation of the composition of Nb at the location with the highest Nb segregation as a function of time predicted by DICTRA simulations using Model 1 with Laves_C14 phase composition from EDS line scans for cast and LPBF Inconel 718 alloys. The homogenization times for the LPBF and cast alloys are 200 s and 2500 s, respectively.

It should be noted that when an underestimated composition for the Laves_C14 phase was used as the input for DICTRA simulations, it can lead to the prediction of homogenization time that is shorter than the optimum value. Since the width of the Laves_C14 particles is around 1 μm or even less (Figs. 3-3(c)&(d)), which is of the order of the EDS interaction volume, the compositions of Nb and Mo in the Laves_C14 phase determined by the EDS line scan can be expected to deviate from the actual values as the composition of the matrix can be included. Because the matrix contains much less Nb than the Laves_C14 phase, the homogenization time predicted using the single-phase simulations with the composition of the Laves_C14 phase

obtained from EDS line scans is expected to be underestimated. In order to circumvent this limitation, the composition of the Laves_C14 phase was estimated using the lever rule and was used as input for the DICTRA simulations. For the lever rule calculation of the Laves_C14 phase composition, the fraction of Laves_C14 phase and γ matrix obtained from image analysis of the SEM micrographs, the composition of the alloy measured using EDS, and the average composition of γ matrix obtained by EDS from different locations were used as inputs.

Table 3-2. Comparison between compositions (in at.%) of the Laves_C14 phase measured using EDS and calculated with the lever rule in the cast and LPBF Inconel 718 alloys.

Processing route	Method	Composition (at.%)						
		Al	Ti	Cr	Fe	Ni	Nb	Mo
Cast	The lever rule	0.61	3.78	16.92	11.69	49.35	14.57	3.08
	EDS	0.93	2.43	16.77	14.19	45.75	16.7	3.23
LPBF	The lever rule	1.58	1.99	20.44	15.60	48.41	9.52	2.46
	EDS	0.99	1.40	20.51	18.02	49.80	6.96	2.32

The fractions of Laves_C14 phase were calculated to be 13.13% and 6.52% in the as-cast and as-built Inconel 718 samples, respectively, using image analysis of the SEM micrographs. It is worth noting that though, Laves_C14 and NbC phases were observed in the as-cast alloy (Fig. 3-2(a)), while calculating the phase fractions of Laves_C14 phase using image analysis, the total fraction of the secondary phases (Laves_C14+NbC) are considered since it is hard to differentiate between these phases based on their contrast in the SEM micrographs. Table 3-2 shows the composition of the Laves_C14 phase in suction-cast and LPBF alloys calculated using the lever rule and the composition obtained using EDS line scan at the location where the highest

segregation of Nb and the widest particle width were observed. The calculated and measured compositions were close. The width of the Laves_C14 phase were obtained from the SEM images. The composition profile calculated from lever rule for Laves_C14 phase and the composition of γ matrix measured from EDS in the cast and LPBF Inconel 718 alloys were used as inputs for DICTRA simulations, as shown in Figs. 3-7(a)&(b), respectively. The composition variation of Nb calculated by DICTRA as a function of time at the locations with the highest Nb segregation in the cast and LPBF alloys is shown in Fig. 3-8. According to the DICTRA simulation results, the homogenization times for the as-built sample is 700 s, while 1500 s is required for the as-cast sample. Therefore, the homogenization times predicted using the Laves_C14 phase compositions calculated from the lever rule are comparable with that from the simulations with EDS line-scanned compositions as inputs.

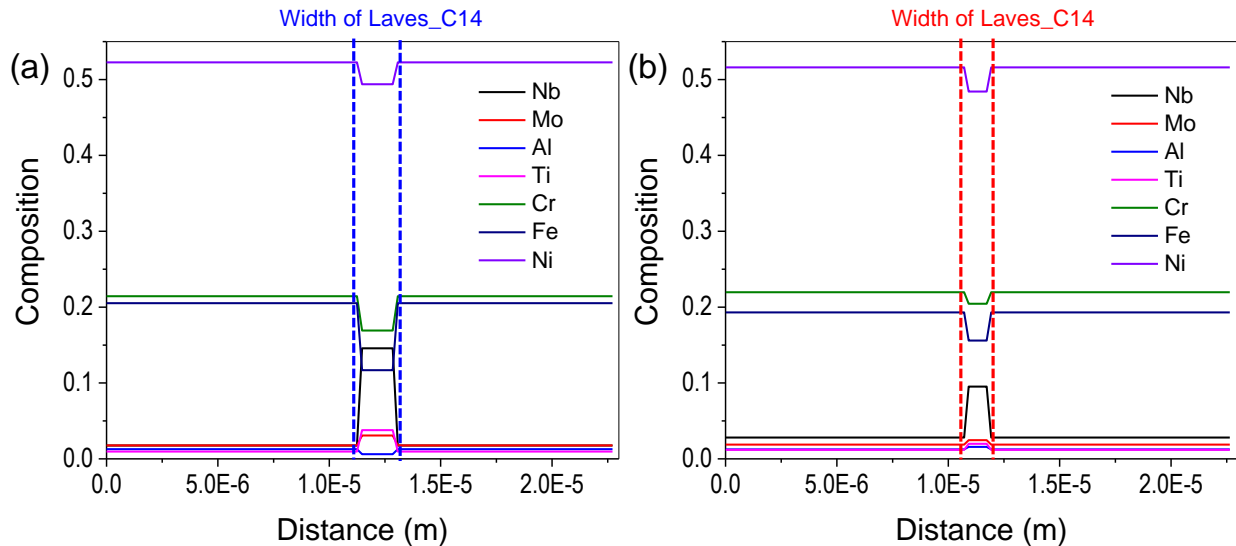


Figure 3-7. Composition profiles (mole fraction) used as inputs for DICTRA simulations using Model 1 where the composition of Laves_C14 phase is determined using the lever rule and the composition of the γ matrix is obtained from EDS for (a) cast and (b) LPBF Inconel 718.

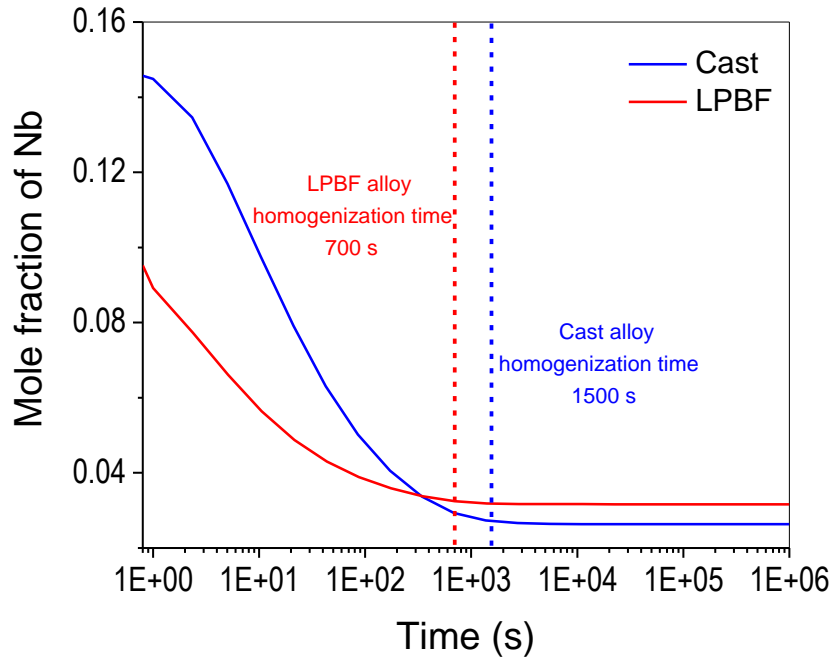


Figure 3-8. Variation in composition of Nb at the location with the highest Nb segregation as a function of time predicted by DICTRA simulations using Model 1 with Laves_C14 phase composition from the lever rule for cast and LPBF Inconel 718 alloys. The homogenization times for the LPBF and cast alloys are 700 s and 1500 s, respectively.

3.1.2.2 Model 2: Single-Phase Simulations with Segregation Profiles from Scheil

Simulations

In this model, a cell with single fcc γ phase was considered and the extents of chemical segregation for the γ matrix predicted using Scheil simulations were used as inputs as proposed by Jablonski and Cowen [68]. From Fig. 3-4(b), it is clear that the primary phase that solidifies from the liquid is the γ phase. The chemical segregation that occurs across the grains of the γ phase comprises the undesired microsegregation which needs to be eliminated using homogenization heat treatment. Hence, the grain size measured using experiments for cast and LPBF Inconel 718 samples were used as the estimate for diffusion distance, i.e., the width of the cell in the DICTRA

simulations. The simulations were performed for 10^5 seconds with 178 grid points for the LPBF alloy and 174 grid points for the cast alloy based on the Scheil simulation results.

Scheil simulations were performed with the compositions measured by EDS, as listed in Table 3-1. The segregation profiles obtained from these calculations were subsequently used as inputs for the single-phase simulations performed using DICTRA in this model. The predicted segregation profile was scaled to the diffusion distance [1]. Because the diffusion was considered to occur in the γ matrix, the diffusion distance was calculated as the product of the γ matrix fraction obtained from the Scheil simulation and the half-width of the grains measured using EBSD (for the cast alloy with equiaxial grains, it was the average grain radius; and for the LPBF alloy, it was the average value of the half-width of three typical columnar grains). The diffusion distance was determined to be 15.3 μm and 28.5 μm for cast and LPBF samples, respectively. The scaled compositions for different alloying elements as a function of diffusion distance for the cast and LPBF alloys are shown in Figs. 3-9(a)&9(b), respectively. It can be found that Nb is the alloying element that undergoes maximum segregation in both the cast and LPBF alloys. The variation in the composition of Nb as a function of time obtained from the DICTRA calculations using this approach is shown in Fig. 3-10. The predicted homogenization time is found to be 2500 s and 15000 s for cast and LPBF alloys, respectively. The time predicted for the cast alloy is fairly comparable with the periods predicted using Model 1. However, the homogenization time is much longer for the LPBF alloy.

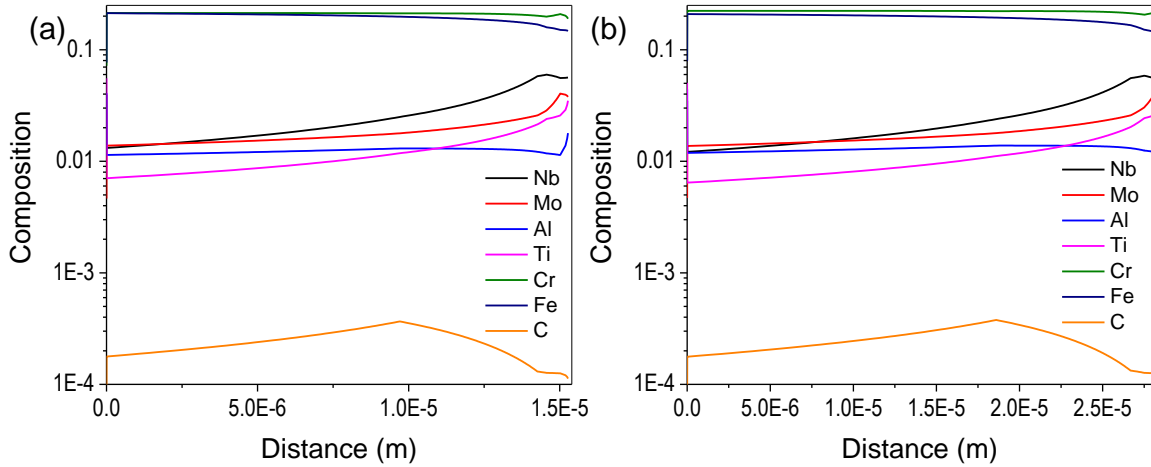


Figure 3-9. Segregation profiles (mole fraction) obtained using Scheil calculations and scaled to diffusion distance for (a) cast and (b) LPBF Inconel 718 alloys that are used as inputs for the DICTRA simulations using Model 2.

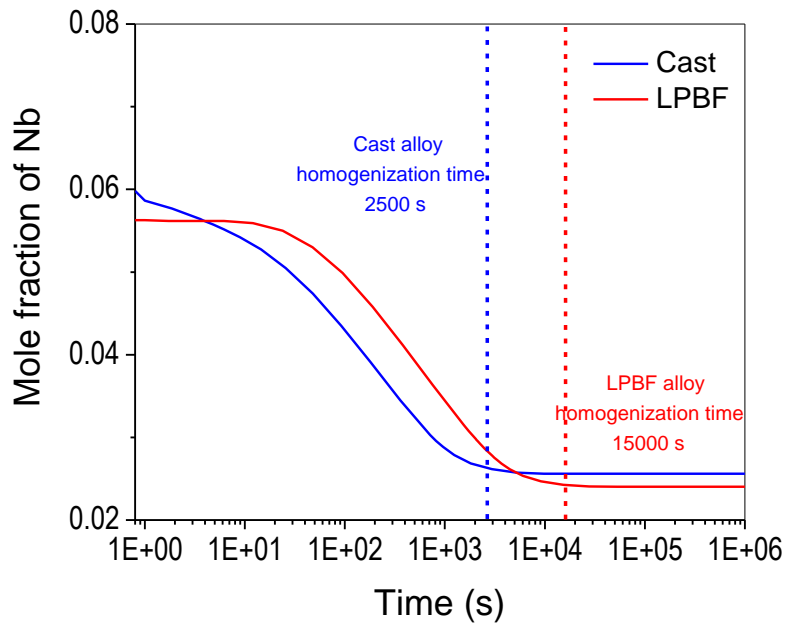


Figure 3-10. Variation in the composition of Nb at the location with the highest Nb segregation as a function of time predicted by DICTRA simulations using Model 2 for cast and LPBF Inconel 718 alloys. The homogenization times for the LPBF and cast alloys are 15000 s and 2500 s, respectively.

3.1.2.3 Model 3: Moving Boundary Simulations with Laves Phase Composition from the Lever Rule

In this model, a cell containing two regions with a planar interface (in order to avoid interfacial energy effects) with one region assigned to the γ matrix and the other one assigned to the Laves_C14 phase was used for the DICTRA simulations, as shown in Fig. 3-5(c). Due to the lack of mobility data, the Laves_C14 region was considered to be a phase without diffusion in the simulation, i.e., a “diffusion-none” phase. The simulations were performed for 50000 seconds with an automatic grid. The composition of the Laves_C14 region was calculated using the lever rule and the composition of the γ matrix was averaged from the EDS measurements performed at different sites of the matrix. The width of the Laves_C14 region in the simulation cell was considered as the half-width of the observed Laves_C14 particle from SEM with the largest width. The width of the γ matrix region was calculated from the width of the Laves_C14 region and the phase fractions of γ and Laves_C14 phases in the as-cast and as-built samples. The position of the interface between the Laves_C14 and γ matrix region as a function of time obtained from DICTRA simulations which indicates the dissolution process in cast and LPBF samples are shown in Figs. 3-11(a)&(b), respectively. The predicted homogenization time for the cast and LPBF Inconel 718 alloys are 1250 and 136 s, respectively, which clearly indicates that the values obtained using this model are underestimated in comparison with the estimated values from Models 1 and 2.

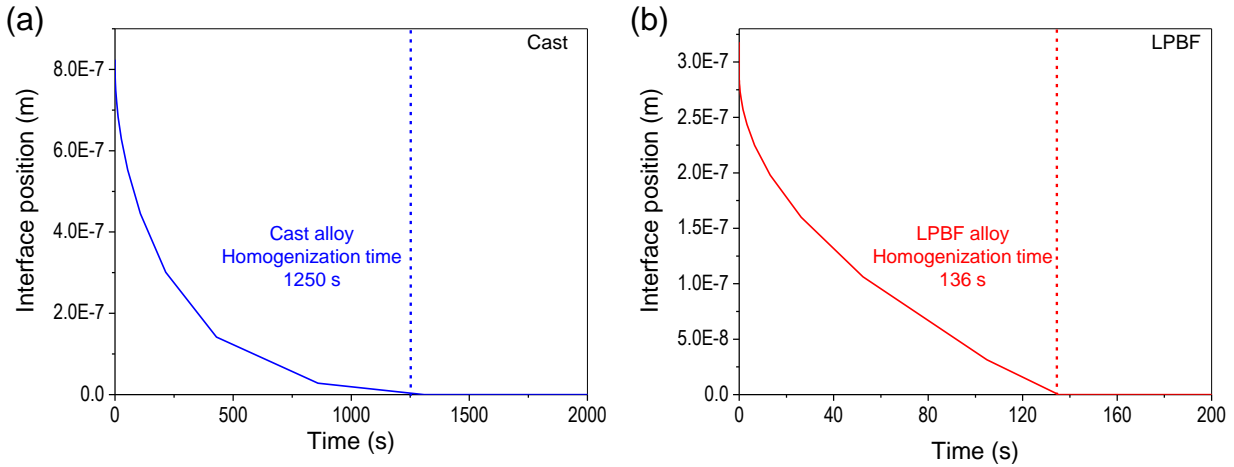


Figure 3-11. Variation of interface position as a function of time indicating the dissolution of Laves_C14 phase predicted by DICTRA simulations using Model 3 for (a) cast alloy with a homogenization time of 1250 s and (b) LPBF alloy with a homogenization time of 136 s.

Moreover, Chen et al. [110] reported that a multiple-cell approach can further improve the accuracy when simulating the dissolution of Si particles during solution treatment of Al-Si binary alloys. In this work, the homogenization time predicted by the moving boundary model with multiple simulation cells was further investigated, in which three simulation cells as same as the one illustrated in Fig. 3-5(c) were established. Ten arbitrarily selected Laves_C14 particles were taken into account to reflect the size distribution of the precipitates. The width of the Laves_C14 region in each cell was set as $w-\delta$, w , and $w+\delta$, where w is the mean value and δ is the standard deviation of the half-width of the Laves_C14 particles. The widths of the γ region in each cell were calculated from the phase fractions as mentioned in the single-cell simulation. Figure. 3-12 shows the calculation results, from which the homogenization time needed for the as-cast alloy is 847 s and for the as-built alloy is 87 s.

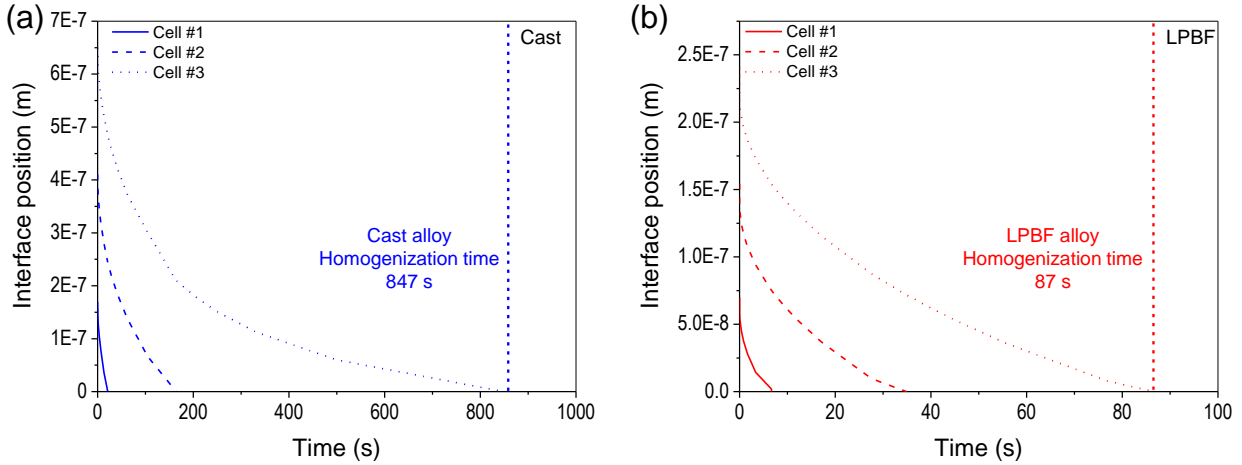


Figure 3-12. Variation of interface positions as a function of time indicating the dissolution of Laves_C14 phase predicted by DICTRA simulations using 3-cell moving boundary model for (a) cast alloy with a homogenization time of 847 s and (b) LPBF alloy with a homogenization time of 87 s. Cell#1, Cell#2, and Cell#3 indicate the simulation cells with the Laves_C14 region width of $w-\delta$, w , and $w+\delta$, respectively.

3.1.3 Experimental Validation of the DICTRA Simulations

In order to validate the DICTRA simulation results, three different homogenization times were chosen based on the results obtained using Model 1: (i) 20 min (1200 s) such that the LPBF sample will attain complete homogeneity and the cast sample will not be completely homogeneous; (ii) 1 h (3600 s) such that both LPBF and cast samples can achieve sufficient homogeneity; (iii) 12 h such that both LPBF and cast samples are homogenized for a sufficiently long duration.

The extent of efficacy attained during homogenization of suction-cast and LPBF Inconel 718 alloys at 1180°C with different durations was deduced by observing the phases present under the SEM-BSE mode as shown in Fig. 3-13. No liquation during homogenization can be found in both suction-cast and LPBF alloys during homogenization.

After homogenizing the cast alloys for 20 min and 1 h, the Laves_C14 phase still can be observed indicating that it has not completely been dissolved into the matrix within these times. Along with the Laves_C14 phase, the presence of the NbC was also found, as shown in Figs. 3-13(a)&(b). After homogenization for 12 h (Fig. 3-13(c)), the Laves_C14 phase dissolves completely, and only NbC is present as the secondary phase in the γ matrix. Hence, it can be ascertained that the homogenization time is between 1 and 12 h for the cast Inconel 718 alloys.

In the LPBF alloys, homogenization at 1180°C for 20 min was found to dissolve the Laves_C14 phase completely, indicating a holding time of 20 min at 1180°C would be sufficient to homogenize the microstructure. NbC carbides precipitate during the homogenization process and their particle sizes are coarsened with extended durations. A more detailed discussion on the phase transformation behaviors will be given in Chapter 3.2.1.

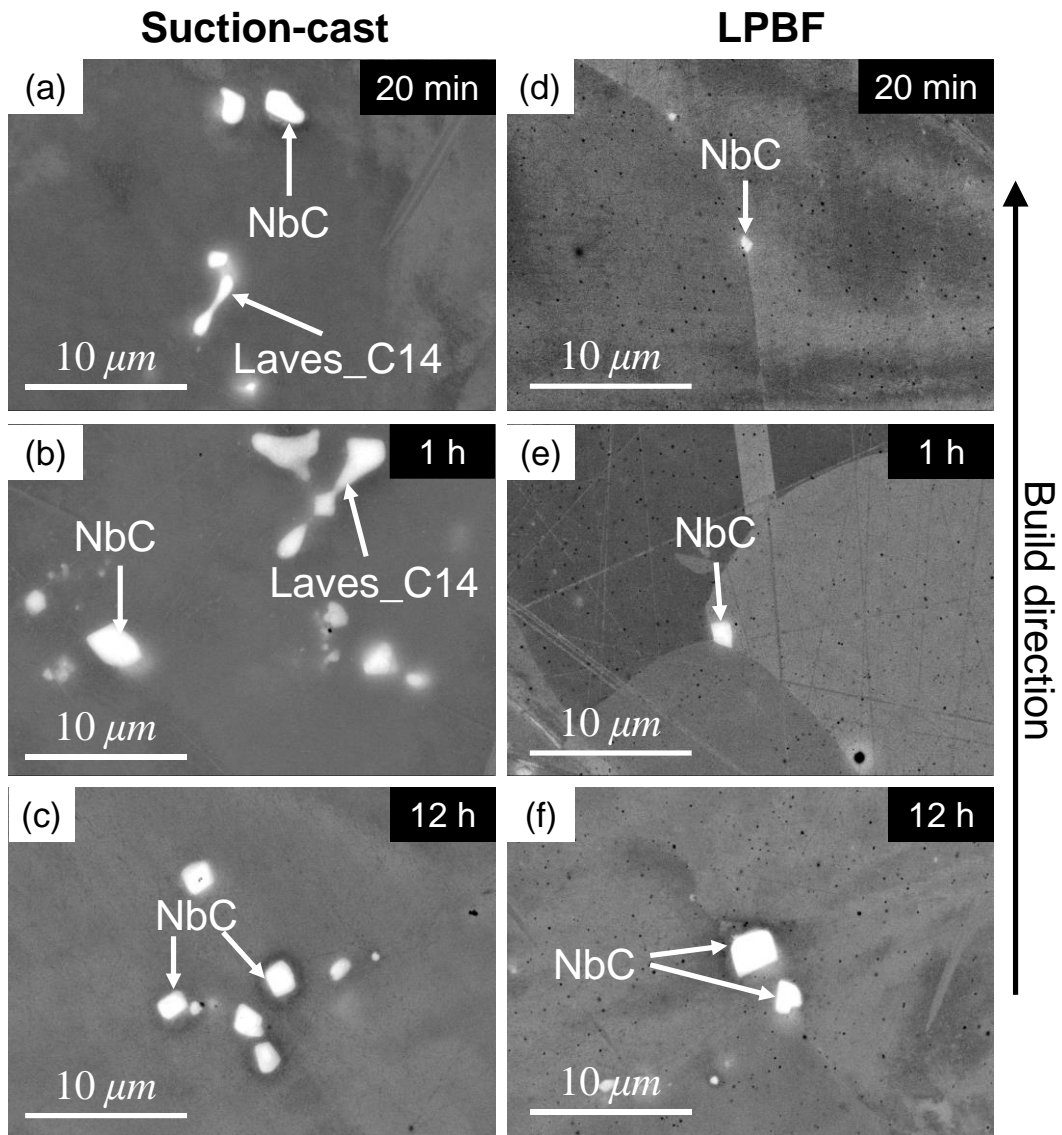


Figure 3-13. BSE-SEM micrographs for cast alloys homogenized for (a) 20 mins, (b) 1 h, and (c) 12 h; and for LPBF alloys homogenized for (d) 20 mins, (e) 1 h, and (f) 12 h.

3.1.4 Discussion

From the aforementioned observations, it can be ascertained that the times required for homogenization heat treatment to dissolve the Laves_C14 phase into the γ matrix for Inconel 718

processed using suction casting and LPBF are drastically different. The estimated time using Model 1 with Laves_C14 phase composition from EDS for the LPBF Inconel 718 alloys fairly correlates with the homogenization time determined using experiments. On the other hand, the estimated homogenization time from the simulations using the Laves_C14 phase calculated from the lever rule in Model 1 is closer to the experimentally determined time for the LPBF alloys. This can be due to the usage of Laves_C14 phase composition calculated using the lever rule which is much closer to the real composition compared to the composition determined using EDS line scan. Hence, the calculation of composition of the secondary phases using the lever rule proves to be helpful for cases where its composition cannot be determined accurately using experiments.

For the suction-cast samples, there is a large difference between the experimental homogenization time and the value predicted by DICTRA simulations using Model 1. This is attributed to the single-phase assumption due to the absence of reliable mobility data for the Laves_C14 phase in Ni-based superalloys, especially for the Laves_C14 particles with higher Nb segregation degrees in the cast alloys. Although in the simulation of LPBF alloys the mobility data of Laves_C14 is also lacking, and the mobility data of the fcc γ phase is used to simulate the Laves_C14 phase in DICTRA simulations, more reliable results are obtained because the segregation widths in the LPBF alloys are much smaller compared with that in the cast alloys. Due to the presence of larger segregation width in cast alloys, approximating the mobility of the Laves_C14 phase region by adopting mobility data for the fcc γ phase cannot provide reliable prediction of homogenization time.

In Model 2, the estimated time for the cast alloy is comparable with the prediction from Model 1, however, it is still not comparable with the experimentally obtained values. This is attributed to the single-phase assumption because of the absence of the mobility values of the

Laves_C14 phase similar to Model 1. The predicted homogenization time for the LPBF alloy is longer when compared to the values predicted using Model 1 as well as the experimental observation. This is mainly because the diffusion distance was overestimated for the LPBF sample. Moreover, the segregation estimated using Scheil simulation is for a simplified solidification process, which does not account for varying solidification velocities, thermal gradients, or subsequent heating and cooling cycles in the solid state that can affect the segregation of the alloying elements. Hence, the Scheil simulations cannot provide reliable segregation profiles for LPBF alloys. This proves that Model 2 is not suitable for estimating the homogenization time for LPBF alloys. The predicted homogenization times from Model 3 for either single or three-cell modeling are underestimated for both the cast and LPBF Inconel 718 alloys because the mobility data for Laves_C14 is not included in the moving boundary simulations. Consequently, the moving boundary simulations are not useful with the absence of reliable mobility data for the Laves_C14 phase, though the simulation setup in this model closely replicated the actual microstructure change. The calculated homogenization times (847 s for cast alloy and 87 s for LPBF alloy) using the three-cell model deviate slightly more from the experimental results compared with those calculated by the single-cell model (1250 s for cast alloy and 136 s for LPBF alloy), indicating that the multi-cell modeling cannot improve the prediction accuracy in this case. This is because the largest particle width is not considered in the multi-cell modeling and the total homogenization time is thus underestimated.

The time taken for completing the DICTRA simulations for implementing different models considered in this study i.e., the run-time was found to deviate significantly for each model. Shorter run-time implies that the model implementation is easier. Hence, along with the accuracy of the predicted value, the run-time should be considered while choosing the model in order to accelerate

the prediction efficiency. It is to be noted that the computational time required for implementing each model depends on the computational power. In this work, for a given computational power (PowerEdge R630 Server including two Intel Xeon E5-2690 processors with 2.9 GHz processor base frequency), it was found that Model 1 took less than 2 mins to complete the simulation, whereas the single-cell modeling of Model 3 took more than 1 h, and the three-cell modeling took more than 10 h. DICTRA simulations using Model 2 were also completed in a few minutes. However, a longer time was required for determining the segregation profiles using Scheil simulations and for scaling of diffusion distance. This makes the implementation of this model harder when compared to Model 1. Therefore, it can be inferred that based on accuracy as well as the convenience in implementation, Model 1 is the most suitable one for predicting the homogenization time with the currently available commercial mobility database.

In a nutshell, these results indicate that there is a necessity for determining mobility values for the atomic diffusion in the Laves_C14 phase of Inconel 718 superalloys with high-fidelity to achieve better prediction capability for the kinetic simulations. For instance, the moving boundary simulations, that mimic the real-time microstructure of the as-cast and as-built Inconel 718 alloy can perform well only when the mobility data for the Laves_C14 phase is available. However, single-phase simulations using DICTRA are capable of estimating the homogenization time more closely to the experimentally determined value for LPBF alloys. Moreover, if the composition of the Laves_C14 phase can be determined accurately, the homogenization time predicted will be closer to the actual value. As a result, the capability of the kinetic simulations using DICTRA is restricted only to LPBF alloys currently. Further determination of the mobilities of different alloying elements in the Laves_C14 phase is expected to extend its applicability to alloys fabricated using different processing routes. It will also enable the simulation setup to mimic the

actual microstructure such as the two-phase setup used for moving boundary simulations. Additionally, taking the interfacial-reaction effect into consideration for the kinetic modeling is expected to further improve the prediction accuracy of the homogenization time.

3.2 Microstructure Evolution during Homogenization at 1180°C

3.2.1 Phase Transformations during Homogenization

Table 3-3. Sample notations and homogenization conditions of the present work.

Sample notations	Manufacturing methods	Homogenization conditions
AC	Suction casting	-
AC20m	Suction casting	1180°C for 20 min with water quench
AC1h	Suction casting	1180°C for 1 h with water quench
AC12h	Suction casting	1180°C for 12 h with water quench
AB	LPBF	-
AM20m	LPBF	1180°C for 20 min with water quench
AM1h	LPBF	1180°C for 1 h with water quench
AM12h	LPBF	1180°C for 12 h with water quench

Based on the analysis in Chapter 3.1, a more comprehensive study was performed to elucidate the microstructure evolution in both suction-cast and LPBF Inconel 718 alloys during homogenization. Table 3-3 summarizes the notations of samples with different manufacturing methods and homogenization conditions. Phase transformation behaviors during homogenization at 1180°C in both suction-cast and LPBF alloys can be analyzed through the SEM-BSE images from Fig. 3-14. As shown in Fig. 3-14, for the suction-cast alloys, 20 min and 1 h homogenization

at 1180°C could dissolve most of the Laves_C14 phase in the as-cast microstructure and could remain the NbC carbides formed during solidification. However, some remaining Laves_C14 particles can still be observed near the NbC carbides, as shown in Figs. 3-14(b)&(c). After 12 h homogenization (Fig. 3-14(d)), the Laves_C14 phase dissolved completely, and only NbC carbides can be observed as precipitates. For the LPBF alloys, no NbC carbide can be observed in the as-built alloy, which is due to its precipitation is suppressed by the fast solidification rate. 20 min homogenization (Fig. 3-14(f)) caused the Laves_C14 phase formed in the as-built condition to dissolve into the γ matrix completely. Meanwhile, only a very small amount of NbC carbides can be found to form along grain boundaries in sample AM20m. Microstructure evolution shown in Figs. 3-14(f)~(h) demonstrates that the homogenizations at 1180°C for a long time can promote more NbC carbide formation. A notable increase of the particle size of NbC carbides can be identified in sample AM12h (Fig. 3-14(h)) after 12 h homogenization by comparing with samples AM20m (20 min, Fig. 3-14(f)) and AM1h (1 h, Fig. 3-14(g)). The formation of coarse carbides in the grain boundaries will lead to the depletion of elements required for forming the strengthening precipitates during subsequent aging treatment. This leads to the formation of a precipitate-free zone around the coarse carbides along the grain boundaries and these zones were found to have lesser strength [111].

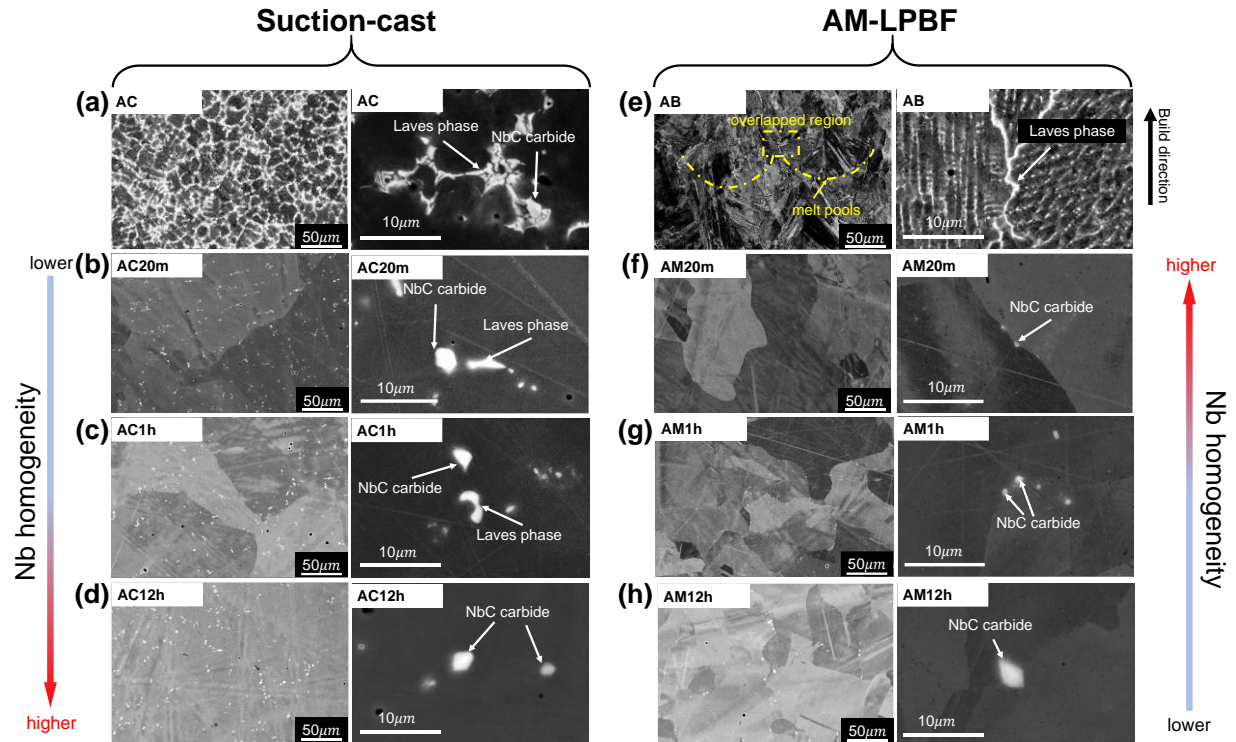


Figure 3-14. SEM-BSE micrographs of Inconel 718 suction-cast alloys with (a) as-cast state, AC; and with homogeneous states at 1180°C for (b) 20 min, AC20m; (c) 1 h, AC1h; (d) 12 h, AC12h. SEM-BSE micrographs of LPBF Inconel 718 alloys with (e) as-built state, AB; and with homogeneous states at 1180°C for (f) 20 min, AM20m; (g) 1 h, AM1h; (h) 12 h, AM12h. The representative NbC carbides and Laves_C14 phase in each sub-figure are shown in the magnified SEM images on the right-hand side thereof.

Table 3-4. Variation of the total phase fraction of both NbC and Laves_C14 phases during homogenization at 1180°C.

Homogenization time	0	20 min	1 h	12 h
Suction casting	13.13% ± 1.3%	0.73% ± 0.07%	0.65% ± 0.07%	0.47% ± 0.05%
LPBF	6.52% ± 0.7%	~0	0.05% ± 0.005%	0.36% ± 0.04%

Table 3-4 summarizes the fractions of Nb-rich phases in suction-cast and LPBF alloys. Since both Nb-rich phases, NbC carbide and Laves_C14 phase, form together, it is challenging to

differentiate them for statistical analysis. Instead, the total fraction of the Nb-rich phases was estimated according to the SEM-BSE images to quantify the difference between suction-cast and LPBF alloys. The total phase fraction of the Nb-rich phases decreases during the homogenization process in suction-cast alloys, while it increases for the LPBF alloys. After 12 h homogenization, the Nb-rich phase fraction of suction-cast alloys becomes close to the phase fraction of the LPBF alloys and approaches a range of 0.36~0.47%, which is consistent with the CALPHAD model-prediction on the amount of equilibrium NbC showed in Fig. 3-4(a). This is because an extended homogenization time will cause the two alloys to approach equilibrium states. However, since there are plenty of NbC carbides in the as-cast alloy, whereas the higher solidification rate results in essentially the absence of NbC carbides in the as-built alloy, the fraction of Nb-rich phases in the suction-cast alloy is decreasing, but in LPBF alloys it is increasing.

From the analysis of the phase transformations above, it can be speculated how the Nb homogeneity change in both alloys during homogenization. In the as-cast sample, the Laves_C14 phase usually locates near NbC carbides. Due to the dissolution of the Laves_C14 phase, as can be observed in samples AC20m (Fig. 3-14(b)) and AC1h (Fig. 3-14(c)), the Nb will be released, and dissolve into the γ matrix, hence the Nb homogeneity around NbC particles should increase. However, for the LPBF samples, owing to the increase of NbC carbides from almost 0% in sample AM20m to 0.36% in sample AM12h (Table 3-4), it can be inferred that the formation of NbC is due to the accumulation of Nb near the NbC nuclei. Such a process will decrease the Nb homogeneity. Consequently, the homogeneity of the Nb content in the Inconel 718 alloy, which only contains 5 wt.% Nb (i.e., 3.4 at.% Nb), can be significantly influenced by the homogenization process. It should be noted that the initial homogeneity of Nb in Inconel 718 can affect its distribution in the homogenized samples and can further influence the precipitation of Nb-rich

phases (such as γ'' and δ phases) in the subsequent isothermal/athermal processes. Therefore, it is essential to further evaluate the evolution of Nb homogeneity during homogenization processes for the heat treatment optimization of Inconel 718.

In order to further quantify the Nb homogeneity, the Nb concentration distribution of the γ matrix in the vicinity of NbC carbides was determined by EDS point identification. For each sample, three NbC carbides were studied, and an average value was taken to represent the Nb homogeneity of the sample. There were three steps in the EDS point identification, which was illustrated in Fig. 3-15(a): (i) a $10\ \mu\text{m} \times 10\ \mu\text{m}$ square matrix was identified with the position of a typical NbC particle at the center; (ii) the EDS point identification was performed for Nb concentrations on 24 nodes which were evenly distributed within the square, the step size between each node was $2.5\ \mu\text{m}$. (iii) the average Nb concentration for each node was calculated for contour diagram plots shown in Fig. 3-15(b). According to this, it was observed that the general trend of the evolution of Nb homogeneity for suction-cast alloys decreases with homogenization time, whereas for LPBF alloys the trend is the opposite.

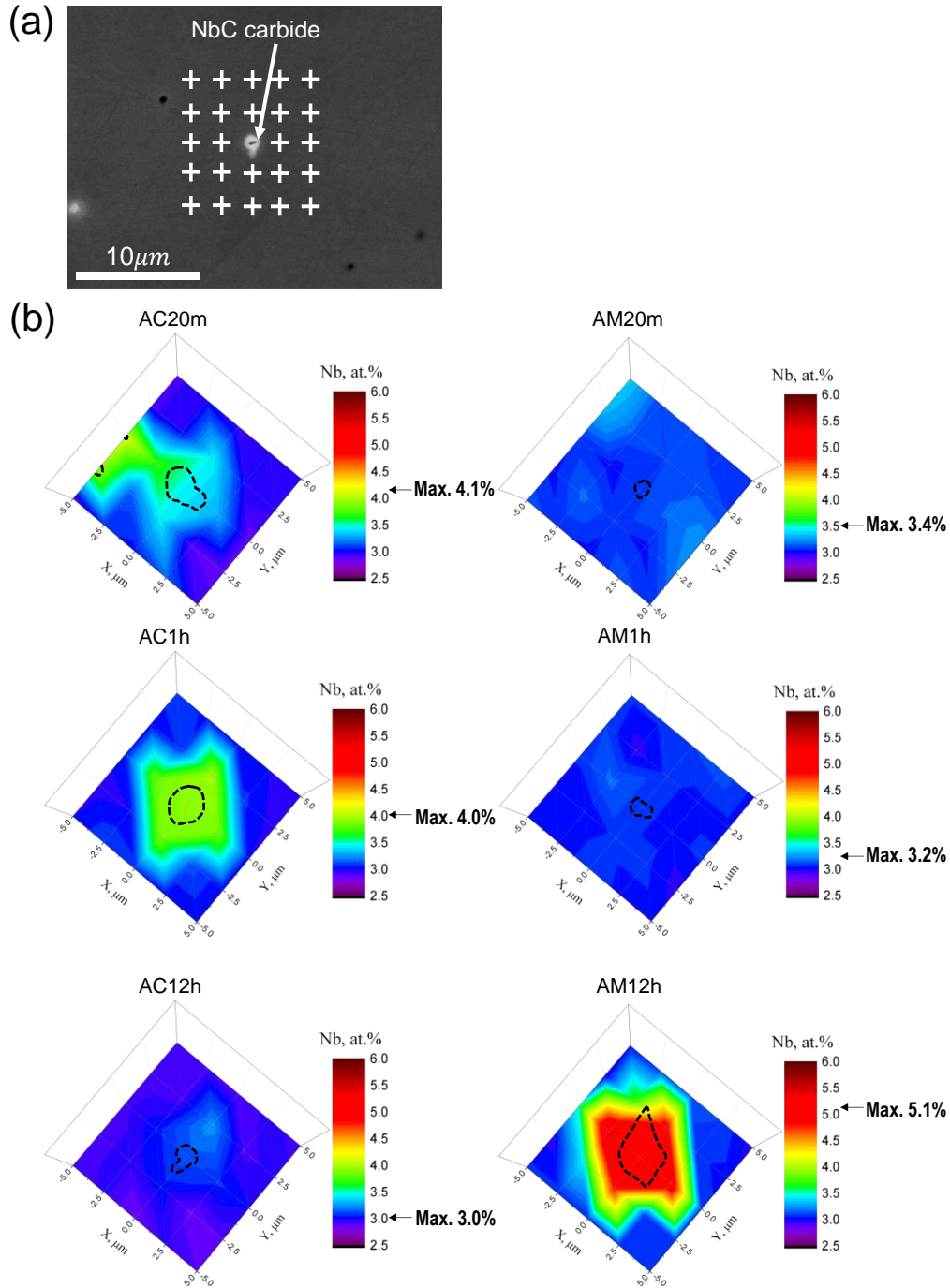


Figure 3-15. (a) Illustration of EDS point identification for Nb homogeneity determination (taking sample AC12h, homogenized suction-cast alloy at 1180°C for 12 h as an example); (b) Nb concentration contour diagrams (10×10 μm) in γ matrix around NbC carbides for presenting Nb homogeneity. The NbC carbides are profiled by dashed black squiggles.

3.2.2 Grain Size Evolution: Recrystallization and Precipitates-pinning Effects

Figures 3-16~3-18 present the grain size evolution and the recrystallization behaviors in both suction-cast and LPBF alloys, which were observed under EBSD. It should be pointed out that because of the large grain size observed in samples AC1h and AC12h, two extra EBSD scans with mapping areas of $2500\ \mu\text{m} \times 2500\ \mu\text{m}$ were conducted in addition to the $1200\ \mu\text{m} \times 1200\ \mu\text{m}$ mapping areas used for all samples. The grain characteristics such as average grain size and grain size distribution of samples AC1h and AC12h were calculated from $2500\ \mu\text{m} \times 2500\ \mu\text{m}$ maps. As depicted in Fig. 3-16, for the suction-cast alloys, the average grain size increases significantly with increased homogenization duration. However, the grain size evolution is opposite in the LPBF samples. Surprisingly, the grain size in the sample AM12h after 12 h isothermal treatment at 1180°C is even smaller than AM20m, which is heat-treated for 20 min.

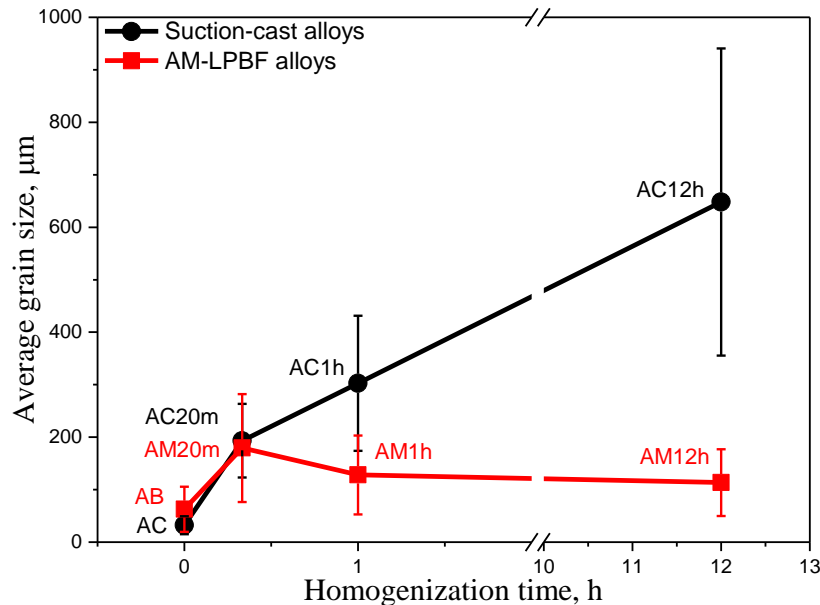


Figure 3-16. The average grain size of suction-cast and LPBF alloys before and after homogenization at 1180°C .

In the left column of Fig. 3-17, i.e., Figs. 3-17(a)~(e), the microstructure evolution of suction-cast alloys during isothermal heat treatment at 1180°C is presented based on the analysis of the inverse pole figure (IPF) orientation maps. The IPF orientation maps with 2500 $\mu\text{m} \times 2500 \mu\text{m}$ mapping areas for samples AC1h and AC12h are shown in the subfigures of Figs. 3-17(d)&(e), respectively. Figure 3-17(a) shows the evolution of grain size distribution for suction-cast alloys with the as-cast state (AC in Fig. 3-16(b)) and homogeneous states at 1180°C for 20 min (AC20m in Fig. 3-17(c)), 1 h (AC1h in Fig. 3-17(d)), and 12 h (AC12h in Fig. 3-17(e)). The area-weighted distribution was used in this work because the long-time homogenization leads to coarsened grains and reduced grain numbers in cast alloy; therefore, it can reflect the relationship between grain characteristics and materials properties in a more suitable way. The unimodal grain size distribution of sample AC20m shown in Fig. 3-17(a) indicates a uniform grain growth during the homogenization of the as-cast samples at 1180°C for 20 min with the microstructure evolution from Figs. 3-17(b) to (c). After 1 h homogenization, a bimodal grain size distribution shown in Fig. 3-17(a) indicates a discontinuous grain growth. The left peak of the grain size distribution curve of AC1h implies the initial grains, and the right peak represents the grown grains from AC20m. This can be observed through a comparison between Figs. 3-17(c)&(d). As illustrated in Fig. 3-17(e), significantly coarsened grains can be found in sample AC12h with some small grains remained at the triple junctions of these coarsened grains. Correspondingly, a trimodal grain size distribution can also be observed in sample AC12h (Fig. 3-16(a)), of which two peaks appearing with smaller grain diameters of 150 μm and 400 μm . The distinct large and small grains observed in sample AC12h (Fig. 3-17(e)) indicate an abnormal grain growth during homogenization.

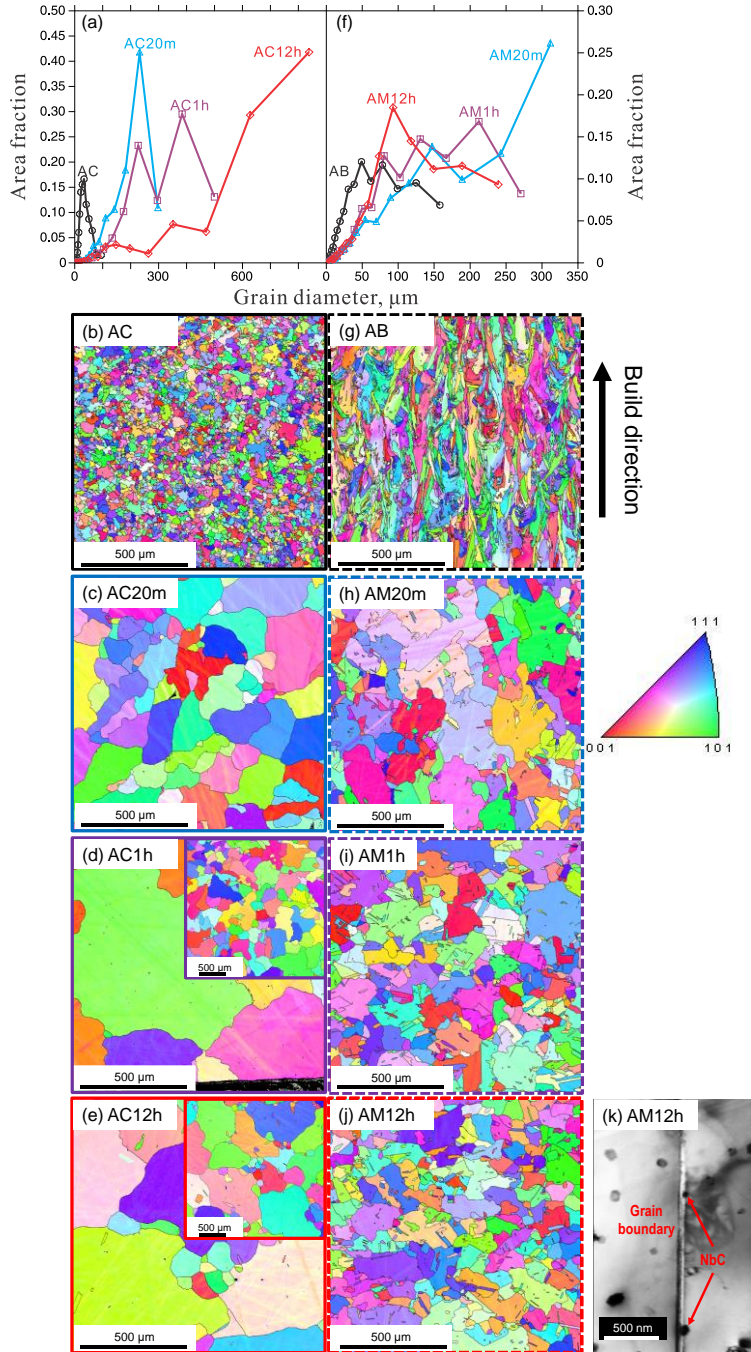


Figure 3-17. Grain size distribution of (a) suction-cast alloys; and inverse pole figure (IPF) orientation maps from EBSD of suction-cast Inconel 718 alloys with (b) as-cast state, AC; and with homogeneous states at 1180°C for (c) 20 min, AC20m; (d) 1 h, AC1h; (e) 12 h, AC12h. Grain size distribution of (f) LPBF alloys; and IPF orientation maps of LPBF Inconel 718 alloys with (g) as-built state, AB; and with homogeneous states at 1180°C for (h) 20 min, AM20m; (i) 1 h, AM1h; (j) 12 h, AM12h. (k) TEM micrograph of sample AM12h.

According to Hillert [112], the abnormal grain growth can be initiated by a continuous decrease of a factor $z=3f/4r$, which represents the dispersion level of secondary phase particles [113]. The f and r represent the phase fraction and particle size of the secondary phase, respectively. The decrease of phase fraction and/or increase of particle size of the secondary phase will lead to a decrease of the dispersion level z and thus reduce the pinning effects of the particles. When there are much larger grains existing in such circumstances, abnormal grain growth can occur. Accordingly, in our case, the occurrence of abnormal grain growth found in suction-cast alloys during homogenization should be attributed to the continuous dissolution of the Laves_C14 phase.

Using the method introduced by Kusama et al. [114], the abnormal grain growth rate was estimated and compared with experimental data. The details of the calculation are given in Appendix A. The calculation shows the experimental abnormal grain growth rate in sample AC12h is 4.7×10^{-9} m/s, which is much slower than the theoretical prediction of 2.067×10^{-5} m/s, indicating the uniformly distributed particles of NbC carbides and Laves_C14 phase can drag the grain boundaries, and thus retard their movement.

In the middle column of Fig. 3-17, i.e., Figs. 3-17(f)~(j), the microstructure evolution of LPBF alloys during isothermal heat treatment at 1180°C is presented based on the analysis of the IPF orientation maps. Figure 3-17(f) shows the evolution of grain size distribution for LPBF alloys with the as-built state (AB in Fig. 3-17(g)) and homogenized state at 1180°C for 20 min (AM20m in Fig. 3-17(h)), 1 h (AM1h in Fig. 3-17(i)), and 12 h (AM12h in Fig. 3-17(j)). In Fig. 3-17(f), the small peak at a grain diameter of 50 μm in the grain size distribution curve of AM20m indicates the initiation of recrystallization in sample AM20m. After 1 h homogenization, three distinct peaks can be observed in the grain size distribution curve for sample AM1h (Fig. 3-17(f)). The average

grain size of sample AM1h (Fig. 3-17) also becomes a smaller value of 128 μm . One possible reason for the further refinement of grain size in sample AM12h compared with AM1h is the small recrystallized grains in sample AM1h grow during homogenization and consume other larger recrystallized grains, of which the grain boundaries are further pinned by NbC formed during recrystallization. After 12 h homogenization, the average grain size value in sample AM12h decreases further down to 113 μm (Fig. 3-17). The grain size distribution of AM12h is close to unimodal (Fig. 3-17(f)). The grain size is not significantly increased after 12 h homogenization at 1180°C from sample AM1h to sample AM12h, especially when compared to that in the cast alloys. This is due to the Zener pinning effects introduced by the NbC particles [112].

The Zener pinning effect [16,18,112,115] of the fine carbide particles, NbC, at the grain boundaries was confirmed by the TEM characterization on sample AM12h, as shown in Fig. 3-17(k). It was found that dispersed NbC particles distributed along and near grain boundaries, indicating that the fine NbC carbides precipitating along with recrystallization at or near grain boundaries can impede grain boundary movement effectively and hence refine the grain size. Contrarily, no pinning effect was found in suction-cast alloys mainly due to the large NbC particle size in the early stage of homogenization and their even distribution inside of the matrix of the grains.

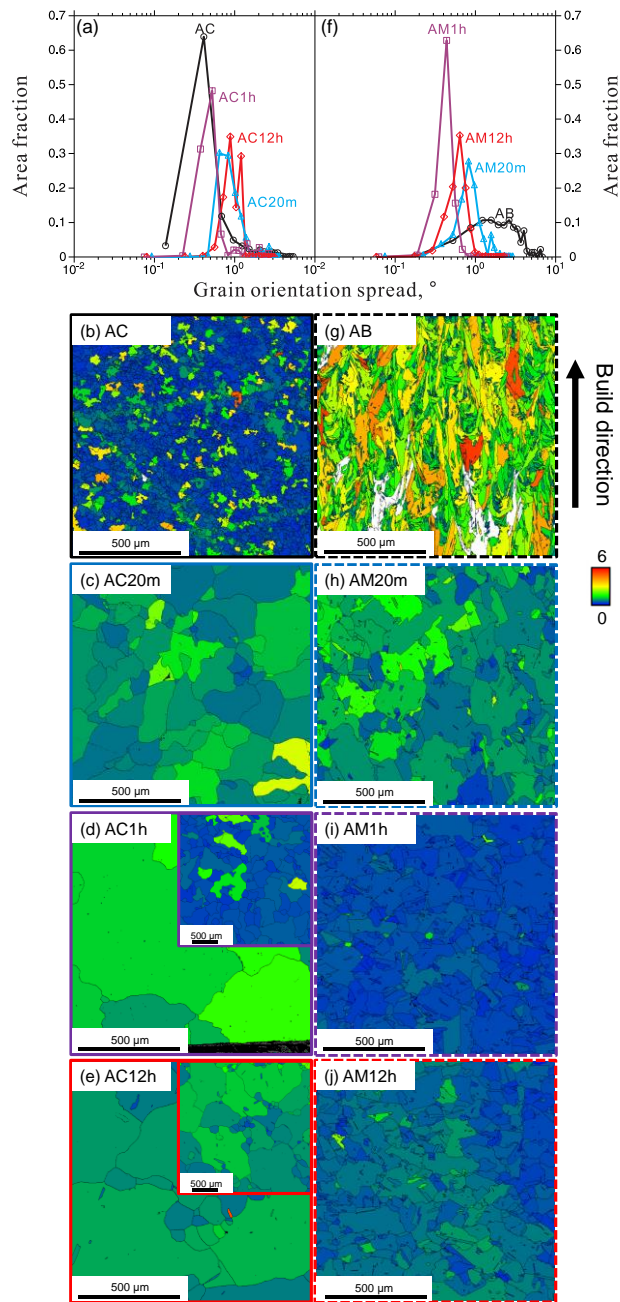


Figure 3-18. GOS distribution of (a) suction-cast alloys; and grain orientation spread (GOS) maps from EBSD of suction-cast Inconel 718 alloys with (b) as-cast state, AC; and with homogeneous states at 1180°C for (c) 20 min, AC20m; (d) 1 h, AC1h; (e) 12 h, AC12h. GOS distribution of (f) LPBF alloys; and GOS maps of LPBF Inconel 718 alloys with (g) as-built state, AB; and with homogeneous states at 1180°C for (h) 20 min, AM20m; (i) 1 h, AM1h; (j) 12 h, AM12h.

Grain orientation spread (GOS) generated from EBSD analysis is useful for quantifying microstructure attributes during recrystallization [116,117,126,118–125]. The average GOS [126] of one grain i is defined as

$$\text{GOS}(i) = \frac{1}{J(i)} \sum_j \omega_{ij} \quad (3-1)$$

of which $J(i)$ represents the pixel numbers of the grain i , ω_{ij} is the misorientation angle between the orientation of pixel j and the mean orientation of grain i .

The GOS value represents the degree of distortion inside a grain. A larger distortion within one grain leads to a higher GOS value. The GOS value for recrystallized grains should be low since less stored energy saved in these grains [119]. As reviewed by Hadadzadeh et al. [119], the threshold of the GOS can be selected between 1~5° for identifying recrystallized grains. Nevertheless, the GOS values are relatively low in the present study, since the samples are free from external deformation. Therefore, it is hard to determine the recrystallized grains by solely defining a threshold of the GOS. Alternatively, the recrystallization behaviors can be studied through a combined analysis of both grain morphology and GOS. The GOS distribution and mapping diagrams of the homogenized samples are presented in Fig. 3-18. The GOS maps with 2500 $\mu\text{m} \times 2500 \mu\text{m}$ mapping areas for samples AC1h and AC12h are shown in the subfigures of Figs. 3-18(d)&(e), respectively. The area-weighted GOS distribution was used following the same reasons proposed in grain size distribution analysis.

A further investigation on the GOS of suction-cast alloys (Figs. 3-18(a)-(e)) shows that it experiences an increase from sample AC to sample AC20m, and then decreases slightly in sample AC1h. The increase of GOS in sample AC20m can be attributed to the strains introduced by grain

growth and dissolution processes of the Laves_C14 phase, of which the phase fraction reduces from 13.13% in the as-cast state to 0.73% in the 20 min homogenized state (Table 3-4). With 1 h homogenization, both GOS and phase fraction of Laves_C14 get reduced. After 12 h homogenization, the GOS in sample AC12h increases, which is due to the increased grain size [126] caused by abnormal grain growth.

The GOS evolution observed in LPBF alloys experiences a decrease from sample AM20m to AM1h, while it slightly increases in sample AM12h, as shown in Figs. 3-18(f)~(j). Sample AM20m has relatively high GOS values because of the distortion accumulation due to residual stress introduced during the LPBF process [127]. Sample AM1h shows the lowest and uniform GOS distribution (Figs. 3-18(f)&(i)), indicating almost all grains are continuously recrystallized and the residual stress has been removed. The GOS in sample AM12h (Figs. 3-18(f)&(j)) increases slightly compared with sample AM1h, whereas it is still at a low level. The reason for such a change is attributed to the deformation induced by Nb accumulation to form more NbC carbides with significantly increased particle size, as shown in Table 3-4 and Fig. 3-14(h).

3.2.3 Dislocation Behaviors in Homogenized Inconel 718

For the homogenized LPBF alloys, a large number of dislocations were found in the vicinity of NbC carbides and grain boundaries. The interactions of dislocation-carbide and dislocation-grain boundary can influence the precipitation and grain boundary hardening remarkably. Figure 3-19 shows multiple dislocation behaviors observed in sample AM12h by TEM. A considerable amount of parallel dislocation arrays/loops are present in the vicinity of larger NbC carbides around 200~300 nm in diameter. However, the dislocation arrays/loops surrounding small NbC carbides are rarely found. This is because small NbC carbides have

coherency with γ matrix, as demonstrated by the selected area electron diffraction shown in the inset of Fig. 3-19(b). The small NbC carbides have similar diffraction patterns to the matrix, with the preferred orientation relationship of $(0\bar{2}2)_{NbC} [\bar{2}33]_{NbC} // (1\bar{1}1)_{\gamma} [\bar{1}12]_{\gamma}$. The comparison of the number of dislocations between carbides with various sizes indicates the generation of dislocations around large NbC carbides results from the loss of coherency of NbC/ γ phase boundaries during the growth of carbides particles, as illustrated in Figs. 3-19(a)&(c), which is consistent with other reported experiments [128–130]. Furthermore, the relief of residual stress during the homogenization process can generate local strains inside of the matrix, while once the local strain field encounters impediment from NbC carbides, dislocations can be emitted to reduce the energy [131]. These two factors contribute to the generation of dislocations and make large NbC carbides be the dislocation sources. Direct evidence of NbC carbides being dislocation sources is noted in Fig. 3-19(a) by the yellow arrow, of which dislocation loops are emitted from NbC carbides with a larger size, about 200 nm in diameter.

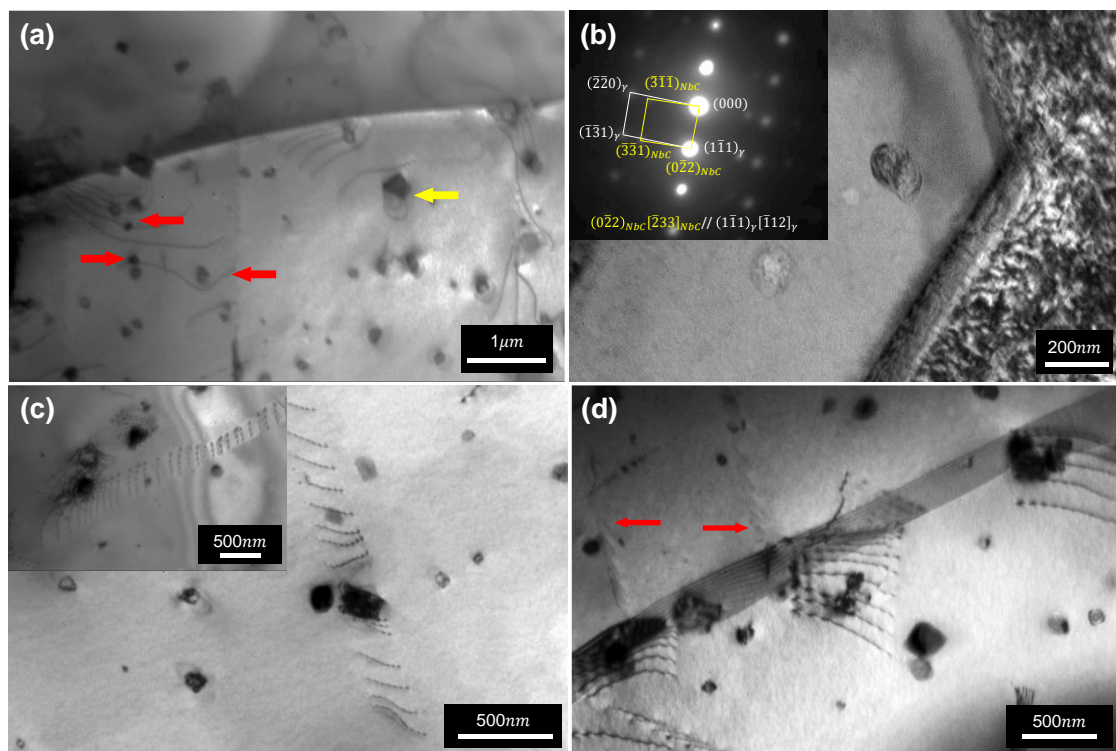


Figure 3-19. TEM micrographs of sample AM12h (homogenized on LPBF alloy at 1180°C for 12 h): (a) grain boundary NbC carbides and dislocation-precipitate interaction; (b) selected area electron diffraction pattern of NbC carbides; (c) planar dislocation arrays; (d) interaction between dislocations and grain boundaries.

The dislocations in sample AM12h mainly appear in planar arrays (Figs. 3-19(a),(c)&(d)), yet tangling and cells caused by a cross slip of dislocations were seldom found. Such a situation agrees with the observation from the work of Sundararaman et al. [132], where the reason lies in the intermediate stacking fault energy of Inconel 718 (50~70 mJ/m²) [132,133], which is sufficiently low to inhibit cross slip during homogenization. In fact, when applying external stresses, dislocation tangling and cells can be formed by cross slip, as reported in the work of Zhang et al. [20]. However, the stacking fault energy of Inconel 718 is not such low to form stacking faults bounded with separated partial dislocations [132]. Likewise, no such stacking fault structure is found in the present work. The present and previous studies indicate that the dislocation

behaviors can be changed depending on various conditions for the range of stacking fault energy in Inconel 718.

The interactions between dislocations and precipitates in sample AM12h were found to follow both Orowan bowing and dislocation cutting mechanisms. As indicated by the red arrows in Fig. 3-19(a), dislocations cut through small particles and bow around large particles while moving to grain boundaries. The dislocation arrays are impeded by grain boundaries then pile up (Figs. 3-19(a)&(d)). According to Kondo et al. [134], the interactions between dislocations and grain boundaries are related to the rotation of the Burgers vector when the dislocation is to cross the grain boundaries, leaving a residual dislocation. The formation of the residual dislocation requires additional energy, making the process energetically unfavorable. Consequently, dislocations are prone to pile up at grain boundaries. Further dislocation pileup leads to new dislocation generation in the adjacent grain, as marked by the red arrows in Fig. 3-19(d), the activation of new dislocations can release local strains and lower the possibility of propagation of cracks.

4.0 Phase Transformations During Continuous Cooling

This chapter is modified from the submitted journal paper: Y. Zhao, L. Hao, Q. Zhang, W. Xiong, Phase transformations during continuous cooling in Inconel 718 alloys manufactured by laser powder bed fusion and suction casting, submitted to Science and Technology of Advanced Materials.

The study in Chapter 3 has shown that the homogenization process can significantly influence the microstructure in both LPBF and suction-cast Inconel 718 alloys, hence, revealing how the manufacturing methods and homogenization conditions affect the phase transformations during continuous cooling is important. Therefore, this chapter aims at a comprehensive evaluation of the phase transformations during continuous cooling processes of Inconel 718 alloys processed by LPBF. The suction-cast alloys were chosen as a reference for comparison for the reasons mentioned in Chapter 3. Both alloys fabricated by LPBF or suction casting were subject to different homogenization conditions and continuously cooled at various cooling rates. Microstructure analysis and quenching dilatometry were conducted on samples to determine CCT diagrams and to investigate the phase transformation behaviors. Microhardness of alloys after cooling were studied to help understand the microstructure-property correlations under different cooling conditions.

4.1 Experiments and Theoretical Analysis

4.1.1 Experiments

The LPBF and suction-cast alloys were fabricated as described in Chapter 2.1. Both alloys were sectioned by EDM wire cutting into cuboids with a dimension of 4×4×10 mm for dilatometry measurements. The length (10 mm) of the cuboids of LPBF alloys was along their build directions.

Table 4-1. Sample notations and heat treatment conditions in the present work.

LPBF samples			Suction-cast samples		
Sample notation*	Homogenization	Cooling rate, K/s	Sample notation	Homogenization	Cooling rate, K/s
AM20m-01		0.1	AC20m-01		0.1
AM20m-1		1	AC20m-1		1
AM20m-2		2	AC20m-2		2
AM20m-5	1180°C for 20 min	5	AC20m-5	1180°C for 20 min	5
AM20m-7		7	AC20m-7		7
AM20m-10		10	AC20m-10		10
AM20m-15		15	AC20m-15		15
AM12h-01		0.1	AC12h-01		0.1
AM12h-1		1	AC12h-1		1
AM12h-2		2	AC12h-2		2
AM12h-5	1180°C for 12 h	5	AC12h-5	1180°C for 12 h	5
AM12h-7		7	AC12h-7		7
AM12h-10		10	AC12h-10		10
AM12h-15		15	AC12h-15		15

* AM20m is used to note a set of alloys with the same homogenization (1180°C for 20 min) but different cooling rates, and thus include seven alloys: AM20m-01, AM20m-1, AM20m-2, AM20m-5, AM20m-7, AM20m-10, and AM20m-15. The same way of notation applies to other alloys.

The cuboid samples were subject to dilatometry with an S-type thermocouple. For each alloy, two groups of samples were further divided with respect to different homogenization

conditions, i.e., 1180°C for 20 min and 12 h, respectively. Samples of each group were then put into a DIL805A quenching dilatometer for the homogenization and subsequent cooling processes to room temperature. The cooling rates were 0.1, 1, 2, 5, 7, 10, and 15 K/s. The sample notations and heat treatment conditions in the present work are summarized in Table 4-1. It should be pointed out that, the samples to be homogenized for 12 h were firstly encapsulated into quartz tubes with backfilled Argon and were then homogenized into the furnace at 1180°C for 11 h. These 11 h homogenized samples were then quenched into ice water and were put into the dilatometer for the remaining 1 h homogenization at 1180°C. This can improve the efficiency of the heat treatment and avoid a long-time experiment in the dilatometer. The continuous cooling processes with different rates were conducted on these samples subsequently.

By checking the similarity of the obtained dilatation curves, typical as-cooled samples were selected from each group for microstructure characterization. These samples were polished using metallographic methods for SEM and EDS characterization. The samples were also etched using a solution of 50 mL $C_3H_6O_3$ +30 mL HNO_3 +2 mL HF to reveal the existence of Nb-rich γ'' and γ' phases [135].

The CCT diagrams were determined through the combined microstructure and dilatometry analysis. The microstructure was characterized to investigate the phase transformations that occur during cooling, and the signals obtained from dilatation curves can be interpreted accordingly. The analysis of sample AM12h-5 was taken as an example, as shown in Fig. 4-1. The SEM micrograph (Fig. 4-1(a)) on the longitudinal plane parallel to the build direction of sample AM12h-5 shows block-shaped NbC carbides and needle-shaped δ precipitates form along the grain boundaries of γ matrix. Neither γ'' nor γ' phase was observed in the etched sample AM12h-5, as their precipitation was suppressed by the fast cooling.

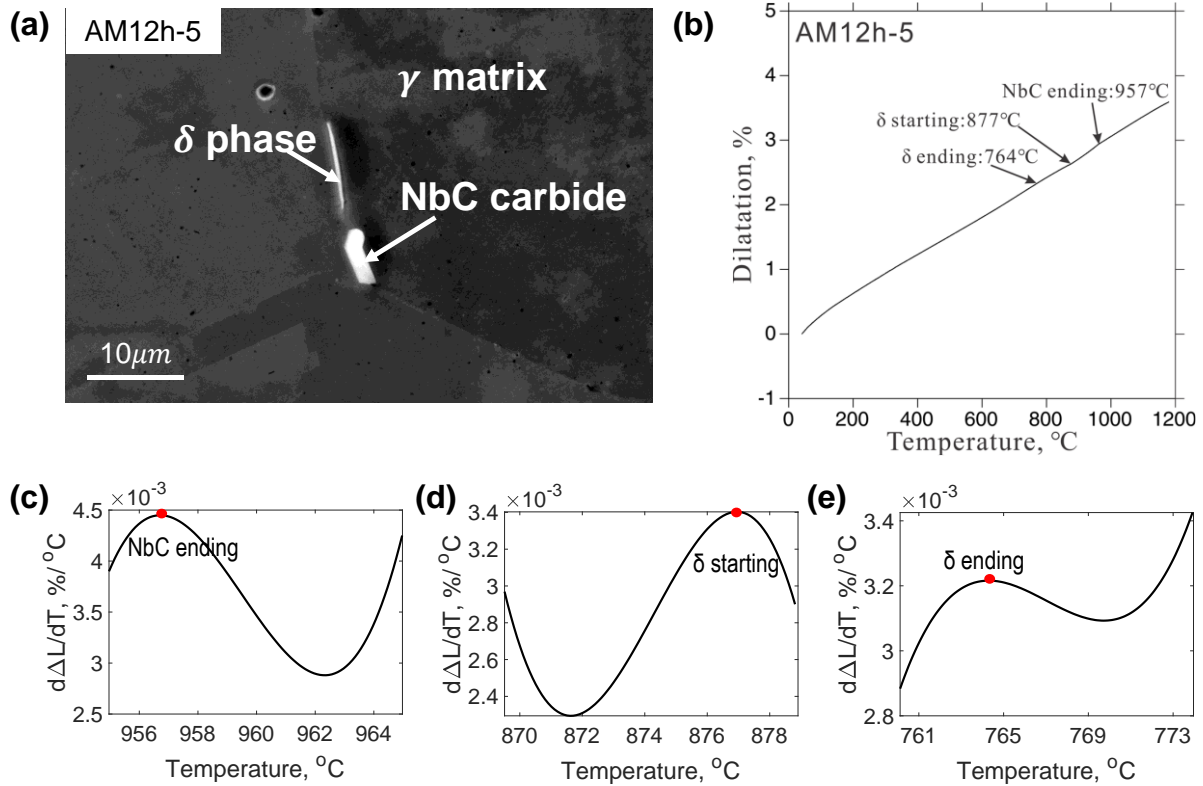


Figure 4-1. Microstructure characterization and dilatometry analysis of sample AM12h-5. (a) SEM micrograph on the longitudinal plane of AM12h-5. (b) Dilatation curve of sample AM12h-5 and its first derivative curves for determining the inflection points of phase transformations for (c) NbC ending; (d) δ starting; and (e) δ ending.

The starting and ending temperatures of phase transformations during continuous cooling were determined by the dilatometry analysis. As indicated by Fig. 4-1(b), the dilatation is plotted as a function of temperature. The slope changes in the dilatation curve represent the occurrence of phase transformations. Because of the small fraction (less than 1% in total) of the precipitates formed during cooling processes, the slope change of dilatation in this work is small, which can reduce the accuracy of the measurement of phase transformation temperature. Hence, the phase transformation temperatures were evaluated to correlate the inflection points which represents the slope change of the dilatation curve. The inflection points locate in where the first derivative of

the dilatation curve reaches the maximal/minimal values, which can be determined by solving the zero points of the second derivative of the dilatation curve [136]. From Figs. 4-1(c)~(e), it can be seen from the 1st derivative curves of the dilatation curve of sample AM12h-5 that there are two inflection points for each curve segment indicating the NbC precipitation ending point, the δ precipitation starting point, and the δ precipitation ending point, respectively. It should be noted that, from Fig. 3-4(a), as the NbC is stable at 1180°C with γ matrix, the formation of NbC carbides should have started during homogenization processes at 1180°C. The starting temperature of NbC carbides during the cooling process is not available, and only the ending temperature can be determined. Therefore, it can be deduced that for the starting of precipitation during the cooling process, the inflection point at higher temperature should indicate the phase transformation point since the dilatation slope should keep constant before the phase transformation happens; on the contrary, for the ending point of precipitation, the transformation point should be indicated by the inflection point at the lower temperature, because the dilatation slope should be a constant after the ending of the precipitation.

In sample AM12h-5 (Fig. 4-1(b)), the ending temperature of NbC precipitation was determined to be 957°C at which the second slope change occurs. Similarly, the first change of the slope at 877°C was determined as the starting temperature of δ precipitation. The ending temperature of δ precipitation was determined as 764°C. The phase transformation temperatures for the rest samples experiencing continuous cooling were determined using the same methods.

4.1.2 Theoretical Analysis

4.1.2.1 TC-PRISMA Simulation Setup

Table 4-2. Parameters of the δ phase precipitation simulation for analyzing the effects of Nb homogeneity.

Conditions	Composition, wt.%	Nucleation sites, /m ³
High Nb homogeneity (e.g., AM20m)	Ni-18.26Fe-18.87Cr-2.97Mo -4.99Nb	3E22
Low Nb homogeneity (e.g., AM12h)	Ni-18.26Fe-18.87Cr-2.97Mo -6.00Nb	3E21

As will be discussed later in Chapter 4.2, the δ phase was found to be the main precipitate during continuous cooling and its precipitation was impacted by Nb homogeneity in the matrix. In order to understand the underlying physics of the δ phase formation observed in experiments of this work, precipitation simulation was performed to qualitatively validate the effects of Nb homogeneity in the matrix near NbC carbides on the CCT diagrams. The simulation was conducted on the TC-PRISMA module implemented in the Thermo-Calc software using the TCNI8 and MOBNI4 databases. The simulation parameters are summarized in Table 4-2, where a lower Nb content of 4.99 wt.% and a higher nucleation site number of $3E22 \text{ m}^{-3}$ were used to simulate the condition of high Nb homogeneity similar to sample AM20m; whereas a higher Nb content of 6.00 wt.% and a lower nucleation site number of $3E21 \text{ m}^{-3}$ were used to simulate the condition of low Nb homogeneity similar to the case of alloy AM12h. A model system Ni-Fe-Cr-Nb-Mo instead of the actual Inconel 718 alloy was considered to improve the simulation efficiency. This would still gain enough insights into the multiphysical influence, particularly Nb homogeneity, on the CCT

diagram of Inconel 718 under different homogenization conditions. A detailed discussion about the simulation results will be given in Chapter 4.3.3.

4.1.2.2 Key Equations in Classical Nucleation and Growth Theory

The classical nucleation theory was applied in this work to gain insights into the mechanisms of phase transformations during cooling processes. The determination of the nucleation rate N_r in this work was based on the classical nucleation theory [137,138]. Assume the nucleation process is steady, N_r is expressed as

$$N_r = Z\beta^*N_0\exp\left(-\frac{\Delta G^*}{k_B T}\right) \quad (4-1)$$

where Z is the Zeldovich factor, which gives the probability of a nucleus to form a new phase, β^* is the attachment rate of atoms to the critical nucleus, N_0 is the number of potential nucleation sites of the δ phase, ΔG^* is the nucleation barrier, k_B is the Boltzmann constant, T is temperature. From the expressions of the Z and β^* [139], at a certain temperature and given a certain phase in an alloy, the two factors can be considered as constants. Hence, according to Eq. 4-1, both increased N_0 and decreased ΔG^* can enhance the nucleation rate N_r .

In addition to the nucleation rate, N_r , the growth rate can also affect the precipitation kinetics. The growth rate of the δ particle J_r is expressed by [140]

$$J_r = \frac{\Delta X_0^{Nb}}{2(X_\delta^{Nb} - X_e^{Nb})} \left(\frac{D}{t}\right)^{\frac{1}{2}} \quad (4-2)$$

of which $\Delta X_0^{Nb} = X_0^{Nb} - X_e^{Nb}$ is the supersaturation of Nb in the matrix, X_0^{Nb} is the Nb concentration in the matrix, X_e^{Nb} is the Nb equilibrium concentration in the matrix adjacent to the δ particles. X_δ^{Nb} is the Nb concentration in equilibrium δ phase, D , and t are the interdiffusion diffusivity of Nb and diffusion time, respectively. Since the δ phase is an intermetallic with the formula of Ni_3Nb , and local equilibrium in the interface is assumed [140], the concentration of Nb in the δ phase and the γ matrix can be considered as constant. Therefore, the diffusivity of Nb, D , is independent of composition and can be regarded as a constant under a certain temperature. According to Eq. 4-2, it is deduced that when the supersaturation ΔX_0^{Nb} increases, the growth rate J_r is increased.

During phase transformation analysis in this work, we applied the above equations to comprehend how the Nb homogeneity in the matrix around NbC carbides influence the nucleation site N_0 , nucleation barrier ΔG^* , the supersaturation ΔX_0^{Nb} to determine their effects on precipitation kinetics.

4.2 CCT Diagrams of LPBF and Suction-Cast Alloys

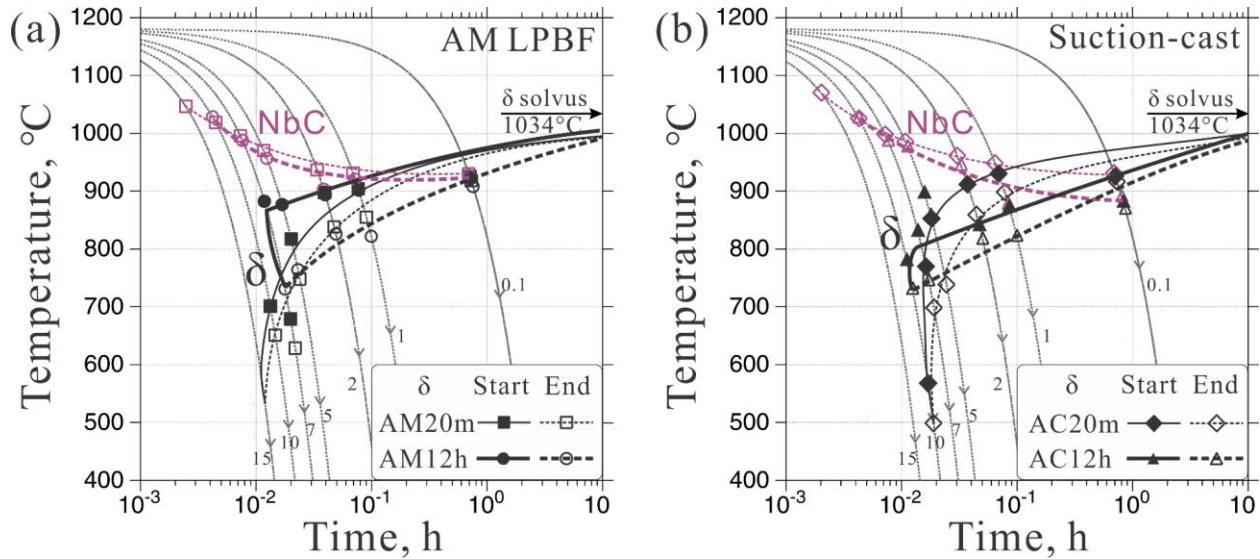


Figure 4-2. Effects of homogenization on the CCT diagrams of (a) LPBF alloys homogenized for 20 min and 12 h; and (b) suction-cast alloys homogenized for 20 min and 12 h. The solvus temperature of the δ phase is predicted using the Thermo-Calc software TCNI8 database. Cooling rates in the unit of K/s (from 0.1 to 15) are indicated in cooling curves superimposed to the CCT diagram plot.

Figure 4-2 summarizes the experimental CCT diagrams of Inconel 718 processed by LPBF and suction casting after homogenization at 1180°C with different durations. NbC and δ phases are the two major precipitates observed in samples after cooling. Since the signal of the γ''/γ' formation was undetectable in the dilatation curves, the CCT curves of γ''/γ' are not given in Fig. 4-2. This is distinctly different from the work by Garcia et al. [62], in which multiple phases (i.e., the Laves phase, the M(C, N) phase, the δ phase, and the γ''/γ' phases) were found to precipitate in sequence during cooling as shown in Fig. 1-8. One of the reasons for such a difference can be the large casting ingot (with a diameter of 530 mm) used in Garcia's work, of which the segregation of Nb was much higher than that in the present work due to the slow cooling rate. The higher Nb

segregation degree caused faster precipitation kinetics for the phases such as the γ''/γ' . The formation of the Laves phase during the cooling process in [62] remains a question because it usually forms during the solidification process [1,25] and no evidence of their formation during the solid-solid phase transformations has been reported to the best of the author's knowledge.

In this work, the solvus temperatures of the δ phase in the suction-cast alloys were calculated to be 1034°C by the TCNI8 database, and it was used to represent the δ solvus temperature for both LPBF and suction-cast alloys as they have identical compositions. This is considered as the limitation during the CCT diagram construction for the case, of which the slowest cooling rate approaches to equilibrium (Figs. 4-2(a)&(b)).

According to Fig. 4-2, the phase transformation ending curves of NbC show a small difference in all CCT diagrams. These curves tend to lower temperature with a slower cooling rate because the longer heating durations from a slow cooling rate can promote the precipitation of NbC more sufficiently. However, a remarkable difference between CCT curves of the δ phase in the alloys under different homogenization durations can be observed (Fig. 4-2). It should be pointed out that although the δ phase was observed in sample AM20m-15, no phase transformation signals can be detected by dilatometer, which is because of the little phase fraction formed. Therefore, the CCT curve of alloy AM20m is extrapolated to the cooling rate of 15 K/s (Fig. 4(a)). Moreover, the manufacturing methods are also found to influence the CCT diagrams of the δ phase, as shown in Fig. 4-3. These findings indicate that the homogenization and manufacturing conditions can have significant effects on the phase transformation of the δ phase during continuous cooling. Such effects will be discussed in detail in the following sections.

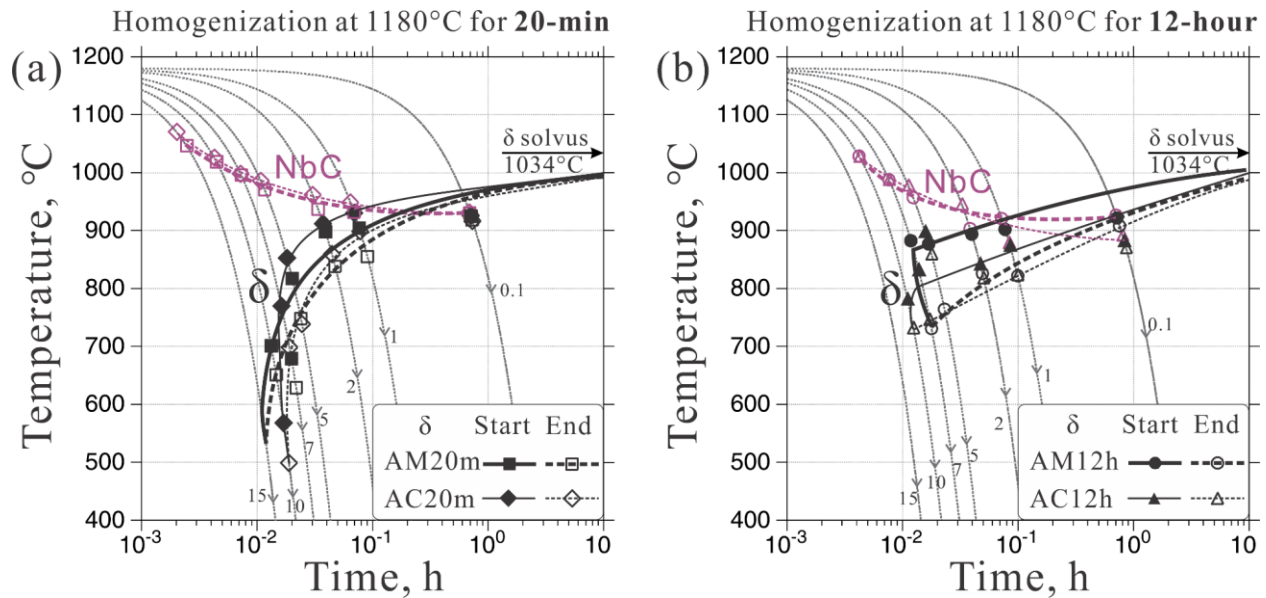


Figure 4-3. Effects of manufacturing methods on the CCT diagrams of (a) LPBF & suction-cast alloys homogenized for 20 min; and (b) LPBF and suction-cast alloys homogenized for 12 h. The solvus temperature of the δ phase is predicted using the Thermo-Calc software TCNI8 database. Cooling rates in the unit of K/s (from 0.1 to 15) are indicated in cooling curves superimposed to the CCT diagram plot.

4.3 Effects of Homogenization on the δ Phase Transformation upon Cooling

4.3.1 Nb Homogenization in Alloys

According to Fig. 4-2, Table 4-3 summarizes the influence of homogenization on the phase transformation starting temperature, phase formation range, and critical cooling rate (as defined in Fig. 1-8(a), Chapter 1.3) of the CCT curves of the δ phase. Long (12 h) and short (20 min) homogenization has opposite effects on the characteristics of CCT curves.

Table 4-3. Comparison of the effects of homogenization durations on the CCT characteristics of the δ phase.

Experimental Information		Phase Formation and Growth Analysis				CCT Diagram Characteristics		
Sample*	Homogenization Time	Nb Homogeneity	Nucleation Potency	Growth Rate	Supercooling	Starting Temperature	Formation Range	Critical Cooling Rate \diamond
AM20m	20 min	Higher +	Higher +	Lower –	Larger +	Lower –	Smaller –	Highest +
AM12h	12 h	Lower –	Lower –	Higher +	Smaller –	Higher +	Larger +	Lowest –
AC20m	20 min	Lower –	Lower –	Higher +	Smaller –	Higher +	Larger +	Medium \circ
AC12h	12 h	Higher +	Higher +	Lower –	Larger +	Lower –	Smaller –	Medium \circ

* AM20m and AM12h are homogenized samples manufactured by laser powder bed fusion, AC20m and AC12h are homogenized samples manufactured by suction casting.

\diamond Critical cooling rates are rough values reading from the evaluated CCT diagram based on experimental data.

As summarized in Table 4-3 and Fig. 4-2(a), when comparing two LPBF alloys, i.e., AM20m and AM12h, the CCT curve of alloy AM20m has a lower starting temperature and a smaller formation range of the δ phase, but higher critical cooling rate. However, such effects of homogenization time on the starting temperature and the formation range of suction-cast alloys are reversed, as shown in Table 4-3 and Fig. 4-2(b). It should be noted that the difference in critical cooling rates between two suction-cast alloys, AC20m and AC12h, are found to be negligible.

Although the determined CCT diagrams by Garcia et al. [62] are distinctly different from this work, the homogenization condition clearly shows a significant impact on the solid-solid phase transformation during continuous cooling. In addition, as discussed in Chapter 3.2.1, the Nb homogeneity degrees in the vicinity of NbC particles in Inconel 718 can vary with different manufacturing methods and homogenization conditions. As shown in Fig. 4-4, for the LPBF alloys, the Nb homogeneity will decrease with extended homogenization durations (Figs. 4-4(a)&(b)), whereas, in the suction-cast alloys, the Nb homogeneity will increase during homogenization with longer time (Figs. 4-4(c)&(d)). As the major element of the δ phase, Nb content and its homogeneity level in the matrix can affect the nucleation and precipitation kinetics of the δ phase.

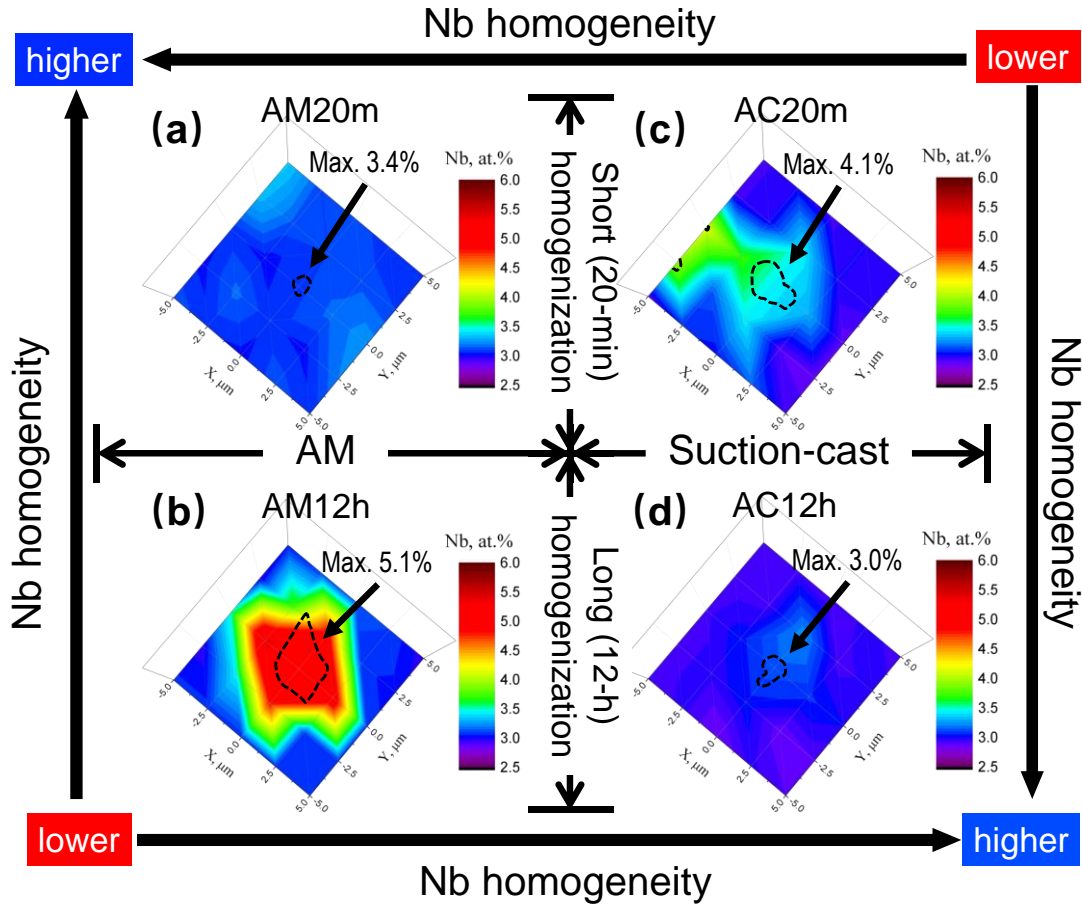


Figure 4-4. (a) AM20m, the LPBF alloy with homogenization for 20 min; (b) AM12h, the LPBF alloy with homogenization for 12 h; (c) AC20m, the suction-cast alloy with homogenization for 20 min; (d) AC12h, the suction-cast with homogenization for 12 h. All the homogenizations are done at 1180°C. Dashed black squiggles profile the NbC carbides. The Nb concentration contour maps are developed using the EDS point identification with a grid size of $10 \times 10 \mu\text{m}$.

Figure 4-5 takes the comparison between alloys AM20m and AM12 as an example to illustrate the way Nb homogeneity affecting the precipitation kinetics. As shown in Fig. 4-5, the homogenized sample AM20m has a higher Nb homogeneity than sample AM12h, thus each Nb atom in sample AM20m shares the same probability of becoming the potential nucleation site, which increases N_0 , and the nucleation rate N_r in Eq. 4-1 rises accordingly. Nevertheless, the

relatively high Nb homogeneity around the nuclei leads X_0^{Nb} in Eq. 4-2 to be low as the concentration fluctuation of Nb will be negligible. The supersaturation ΔX_0^{Nb} in Eq. 4-2 is hence reduced, resulting in a decrease in the growth rate. Therefore, the δ phase formation in alloy AM20m during continuous cooling primarily depends on the nucleation process while limited by the growth process. It is noteworthy that, some other defects, such as dislocations or stacking faults, can also act as heterogeneous nucleation sites during isothermal phase transformations [141] for the precipitates since the nucleation barrier can be effectively reduced and the diffusion of the solute atoms can be promoted. However, in the present work, the continuous cooling processes offer the driving force for the nucleation and limit the diffusion of the atoms, which is different from the case in the isothermal phase transformations. Therefore, it can be presumed that the effect of defects on the phase transformations during continuous cooling processes is not as important as that in the isothermal phase transformations, and it is reasonable to apply a homogenous nucleation mechanism for analysis.

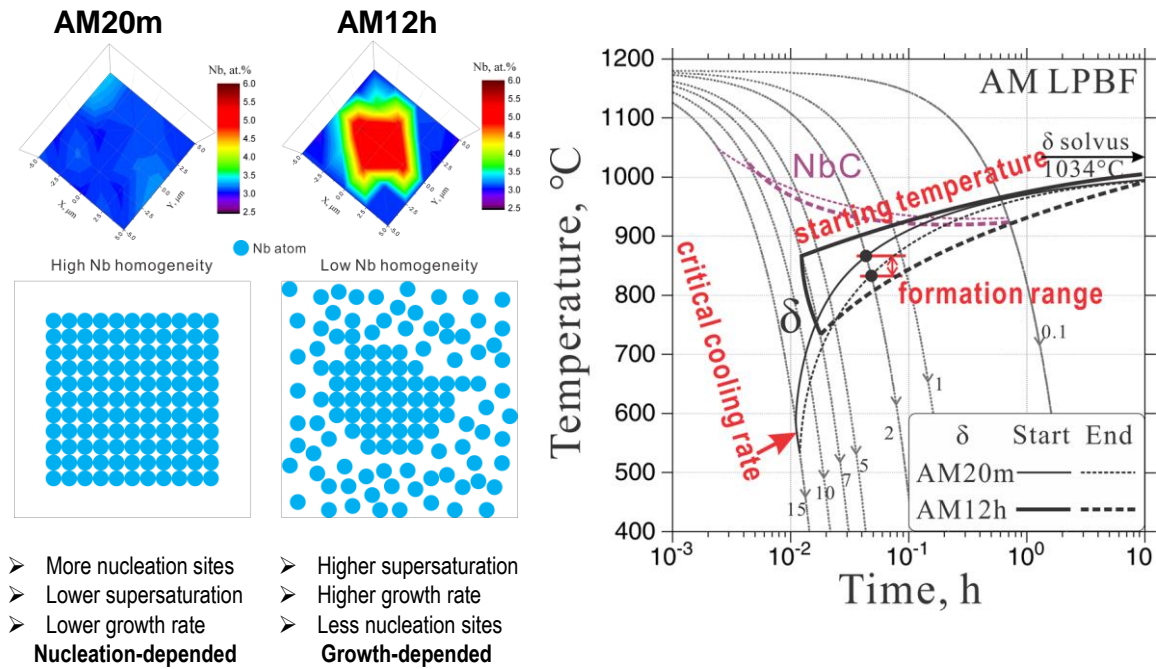


Figure 4-5. Illustration of the effects of Nb homogeneity in the matrix near the NbC particles on precipitation kinetics of the δ phase (taking alloys AM20m and AM12h as an example).

4.3.2 Analysis Based on Classical Nucleation and Growth Theory

From Eq. 4-1, the nucleation rate N_r can be significantly influenced by the nucleation barrier ΔG^* , which can be reduced through obtaining an increased supercooling during the nonequilibrium cooling process. In alloy AM20m, the starting temperature of the CCT curve of δ was found to be lower than that in AM12h, as shown in Table 4-3 and the CCT diagram in Fig. 4-5. It indicates that the alloy AM20m has a larger supercooling degree during cooling when the δ phase starts to form, which is beneficial to the nucleation process. This is because of the low Nb supersaturation in this alloy, with which a larger supercooling should be achieved to provide enough nucleation driving force to decrease the nucleation barrier. In addition, when the cooling

rates for AM20m become faster, the supercooling of δ precipitation further increases with a higher driving force for nucleation. Because the precipitation in alloy AM20m mainly depends on the nucleation process, a higher cooling rate can hence promote nucleation by offering a higher nucleation driving force to reduce the nucleation barrier, making the nucleation easier. This allows the δ phase to form at high cooling rates, which explains the higher critical cooling rate observed for the δ phase in alloy AM20m (Table 4-3 and Fig. 4-5). In contrast, since the growth process of the δ phase is limited in alloy AM20m during cooling, the precipitation process finishes faster, leaving a relatively smaller formation range (Table 4-3 and Fig. 4-5).

In alloy AM12h, as can be seen in Fig. 4-5, due to the lower Nb homogeneity, the number of potential nucleation sites N_0 is less, as the Nb atoms close to the center of the Nb-rich area are more likely to become the nucleation sites. However, the local supersaturation around the nuclei can be higher. The growth process becomes the promoting factor of the precipitation, while the nucleation process limits the phase transformation. The precipitation kinetics of δ depends more on the precipitate growth in alloy AM12h during cooling. Under such circumstances, a small supercooling degree is beneficial to the diffusion of solute atoms during the growth process. Accordingly, in experiments, the CCT curve of the δ phase in alloy AM12h has a smaller supercooling, leading to a higher starting temperature comparing with that in alloy AM20m. The growth process in alloy AM12h can also last a longer time, and the formation range is thus larger (Table 4-3). In addition, when the cooling rates become higher in alloy AM12h, the phase transformation will be suppressed due to the diffusion of solute atoms is retarded, causing a lower critical cooling rate of 7 K/s (Table 4-3 and Fig. 4-5).

For the suction-cast alloys, AC12h and AC20m, a similar explanation of the difference of the CCT curves can be applied. As can be seen in Figs. 4-4(c)&(d), Nb homogeneity increases

with longer homogenization durations, so that the alloy AC12h has a higher Nb homogeneity than alloy AC20m. According to the analysis above, for the suction-cast alloys homogenized for 20 min, the growth process dominates the precipitation process of the δ phase, while for the suction-cast alloys homogenized for 12 h, the nucleation process dominates the precipitation kinetics of δ phase. This is opposite to the case in the LPBF alloys, as shown in Table 4-3.

4.3.3 Analysis Based on Precipitation Simulation

Figure 4-6 is the simulated CCT diagram of the δ phase performed using TC-PRISMA according to the introduction in Chapter 4.1.2. It shows that the low Nb homogeneity in the alloy, similar to AM12h, has higher starting temperatures and a lower critical cooling rate than the condition like AM20m with high Nb homogeneity. The simulation results agree reasonably well with the experimental observation shown in Fig. 4-2(a). This proves that the Nb homogeneity can affect the CCT diagrams of the δ phase in the way depicted by Fig. 4-5. It is noted that the difference of formation range observed in experiments (Fig. 4-2(a)) is not reflected by the simulation. This is because the whole precipitation system in the precipitation simulation was considered homogeneous (either for the case of 4.99 or 6.00 wt.% Nb). Therefore, the more sufficient diffusion of Nb in sample AM12h compared with sample AM20m at a lower temperature due to the higher Nb supersaturation cannot be captured by the simulation. However, in the practical case, the lower Nb homogeneity in sample AM12h increases the Nb supersaturation, leading to a higher diffusion driving force and allowing Nb to diffuse at a relatively lower temperature to form δ phase.

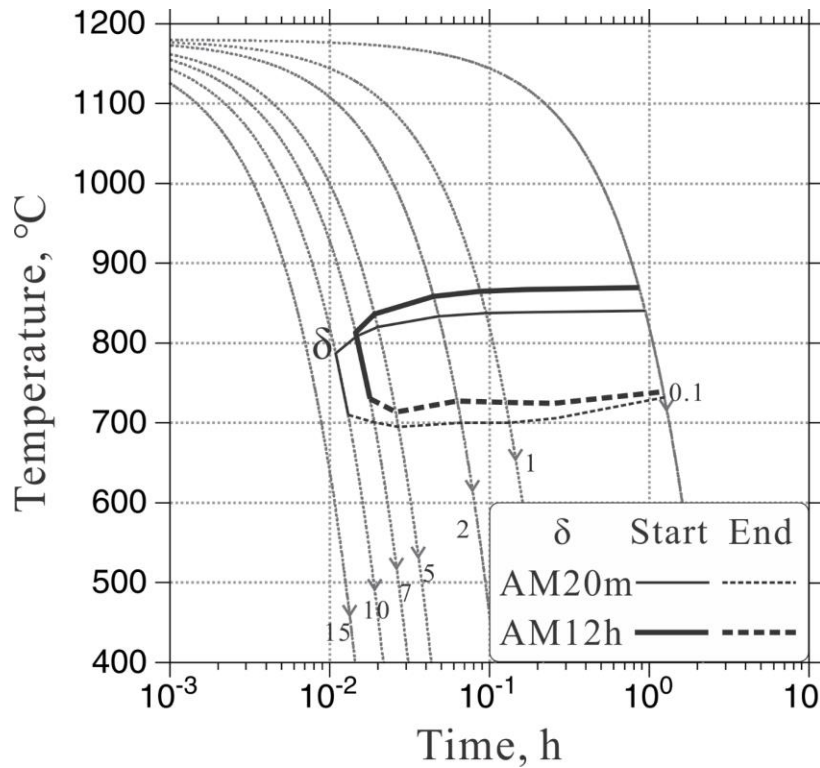


Figure 4-6. Precipitation simulation of the δ phase for the qualitative analysis of Nb homogeneity effects on the CCT diagrams. AM12h and AM20m represent the conditions of low Nb homogeneity and high Nb homogeneity, respectively.

In summary, with the same manufacturing method, the homogenization durations can affect the phase transformation behaviors of the δ phase during continuous cooling processes. This effect is achieved by varying the Nb homogeneity. For the LPBF alloys, extending the homogenization duration leads to the reduction of Nb homogeneity, making the precipitation kinetics of the δ phase depends more on the growth process, yet for the suction-cast alloys, the extension of homogenization durations results in an increase of Nb homogeneity, and the precipitation kinetics mainly depends on nucleation process.

4.4 Effects of Manufacturing Methods on the CCT Diagrams of δ Phase

The manufacturing methods were also found to influence the precipitation of the δ phase in the alloys subject to the same homogenization durations. As shown in Figs. 4-3(a)&(b) and listed in Table 4-3, with the same homogenization duration of 20 min (Fig. 4-3(a)), the CCT curve of δ phase in the LPBF alloy (AM20m) has a lower starting temperature, smaller formation range, but higher critical cooling rate compared with the suction-cast alloy (AC20m). However, under homogenization for 12 h (Fig. 4-3(b)), the LPBF alloy (AM12h) has a higher starting temperature, larger formation range, but a lower critical cooling rate than the suction-cast alloy (AC12h).

Such a difference can be readily explained through the Nb homogeneity analysis similar to Section 4.3. Figures 4-4(a)&(c) indicate alloy AM20m has a higher Nb homogeneity than alloy AC20m; therefore, it can be inferred that the nucleation process is the main factor contributing to the precipitation of δ phase in alloy AM20m. The supercooling degree in alloy AM20m should thus be large to provide sufficient nucleation driving force, which causes the reduction of starting temperature and increased critical cooling rate, as listed in Table 4-3. Meanwhile, the growth rate in AM20m is limited attributed to a lower Nb supersaturation, which leads to a smaller formation range. The effects of manufacturing methods on the CCT curves of samples homogenized for 12 h listed in Table 4-3 can be interpreted in the same way.

In general, with the same homogenization durations, the manufacturing methods can influence the precipitation kinetics of the δ phase during continuous cooling by generating different Nb homogeneities. For the short duration of homogenization (20 min), the LPBF alloy has a higher Nb homogeneity, and the precipitation kinetics of the δ phase depends more on the nucleation process, yet the Nb homogeneity is lower in the suction-cast alloy, and the precipitation

is more dependent on the growth process. The circumstances for long durations of homogenization (12 h) are reversed.

4.5 Effects of Cooling Rates on Microhardness

The Microhardness of alloys after continuous cooling was investigated by Vickers microhardness testing, and the results are presented in Fig. 4-7. For the tested alloys, as illustrated in Figs. 4-7(a)~(d), the cooling rates of 1~15 K/s result in comparable hardness values (229.5 HV to 272.1 HV) with the as-homogenized samples. However, the hardness values achieved in the samples cooled at 0.1 K/s are evidently higher. Sample AM20m-01 exhibits the highest hardness of 421.1 HV, whereas the hardness values of the rest three samples cooled at 0.1 K/s vary from 349.8 HV to 402.8 HV. This indicates some significant microstructure differences among these samples.

Since the samples cooled at 0.1 K/s all have relatively high hardness (Fig. 4-7) compared to other samples cooled at higher cooling rates, these samples were etched for microstructure observation. In the etched microstructures, a large number of δ precipitates can be found to form along grain boundaries in all these samples, as seen in the subfigures of Figs. 4-8(a)~(d). Moreover, the appearance of subgrain boundaries can be observed in all samples with a cooling rate of 0.1 K/s (Fig. 4-8). Such subgrain boundaries were not observed in the samples cooled at higher rates, which implies they may be related to the high hardness in the samples cooled at 0.1 K/s. The subgrains is deduced to form through the tangling of dislocations, which are generated through the loss of coherency of δ/γ phase boundaries during the precipitation of the δ phase [129,142]. The δ particles can further pin the subgrain boundaries and regard their movement. As a result, small

subgrains form due to the δ precipitation, and the hardness is elevated accordingly. Conversely, precipitation of the δ phase is more limited at cooling rates faster than 0.1 K/s, so the subgrains are less likely to form. This explains the lower hardness obtained in the rest as-cooled samples.

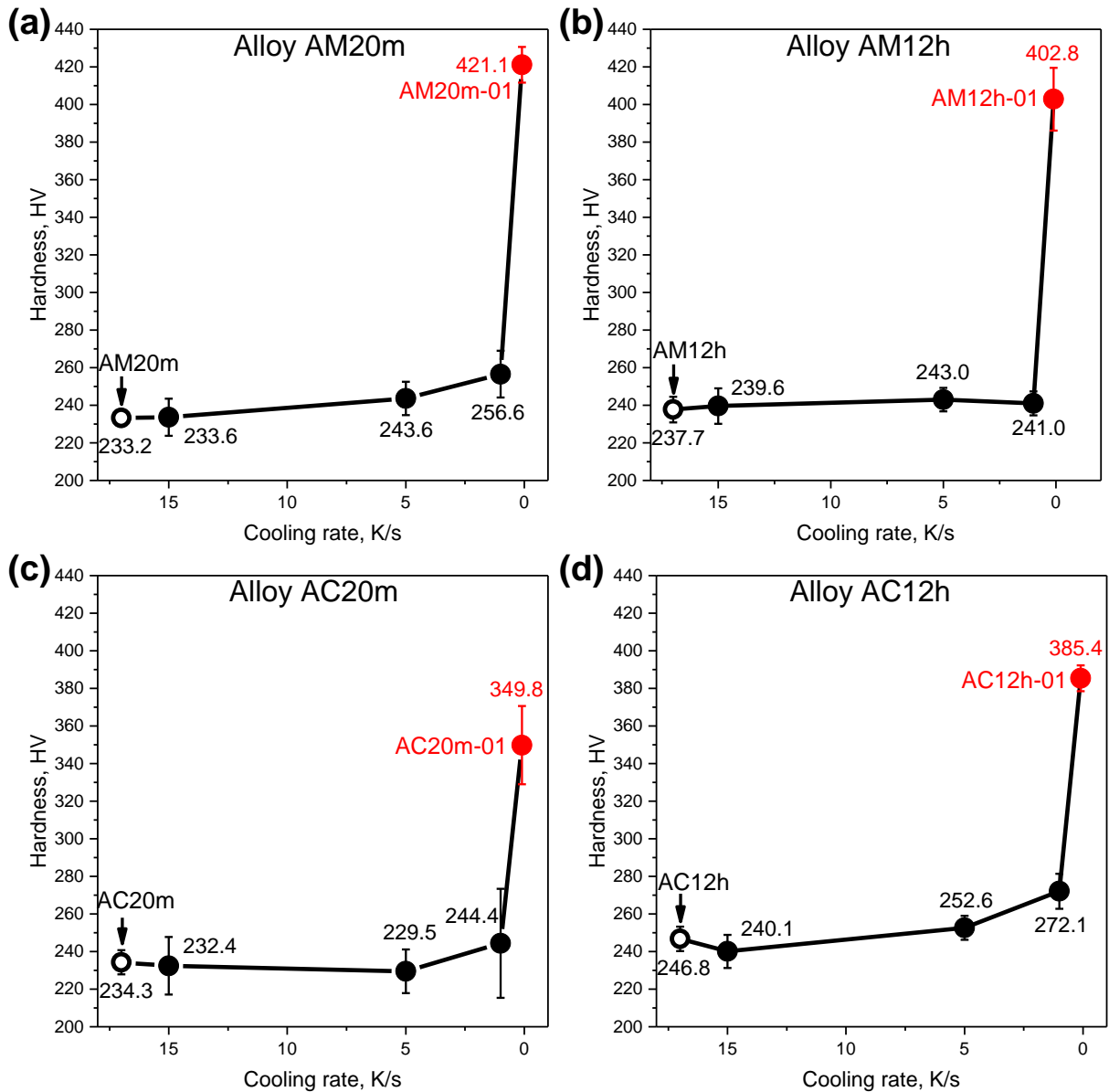


Figure 4-7. Vickers hardness testing results of continuously cooled Inconel 718 samples after homogenization at 1180°C with 20 min or 12 h: (a) alloy AM20m; (b) alloy AM12h; (c) alloy AC20m; (d) alloy AC12h. AC means the alloys are prepared using suction casting and AM is noted for the samples prepared by LPBF.

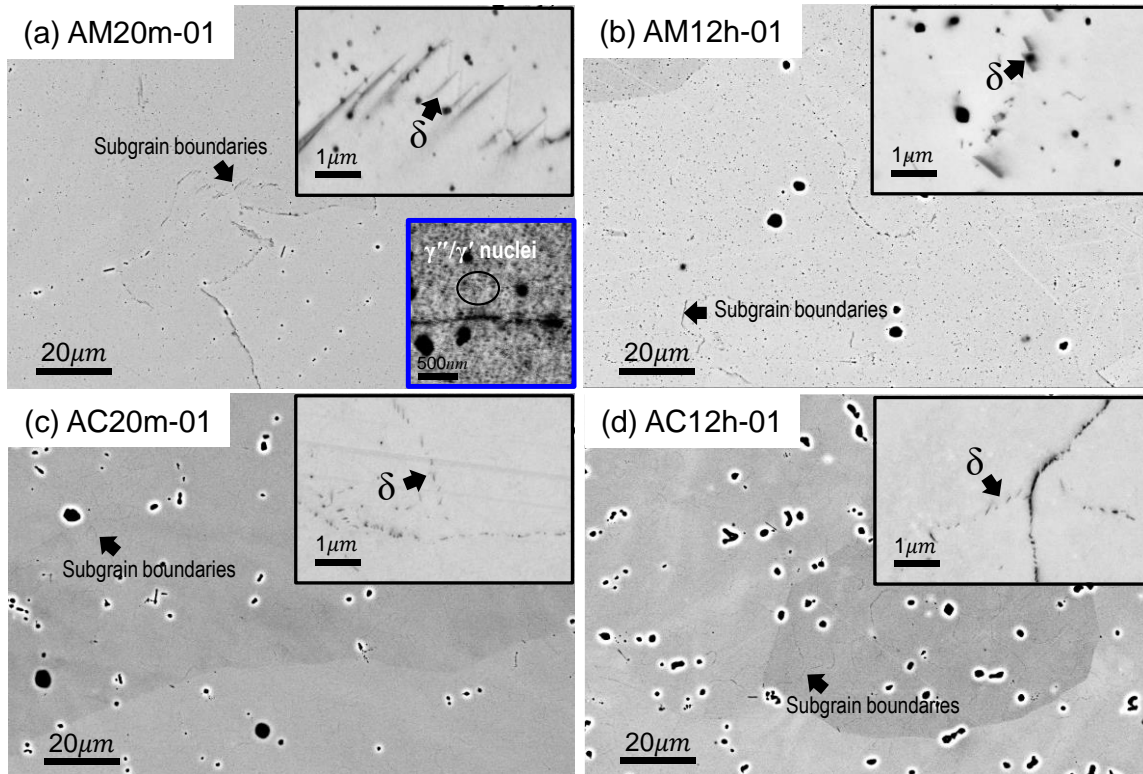


Figure 4-8. SEM micrographs on etched Inconel 718 samples cooled at 0.1 K/s: (a) sample AM20m-01; (b) sample AM12h-01; (c) sample AC20m-01; (d) sample AC12h-01.

Moreover, the precipitation strengthening due to γ''/γ' formation could be one of the reasons that cause the sample AM20m-01 to have the highest hardness values among all the samples cooled at 0.1 K/s (Fig. 4-7). As shown in Fig. 4-8(a), a trace of γ''/γ' nuclei can be observed in sample AM20m-01, although their dilatation signals are too weak to be detected. Geng et al. [69] reported that the γ'' precipitation was observed at cooling rates between 0.1~20 K/min (0.0017~0.33 K/s), which is consistent with the observation in sample AM20m-01. However, in Figs.4-8(b)~(d), no γ''/γ' nuclei can be observed in samples AM12h-01, AC20m-01, and AC12h-01. Hence, the occurrence of γ''/γ' nuclei can explain the highest hardness in sample AM20m-01 among all

samples cooled at 0.1 K/s. The exclusive precipitation of γ''/γ' in sample AM20m-01 is due to the homogenized alloy AM20m has the largest amount of Nb dissolved into the matrix, since the least amount of Nb-rich phases, i.e., Laves_C14 and NbC carbides, was found in this alloy (Chapter 3.2.1). Consequently, it leads to a higher Nb concentration in the γ matrix of sample AM20m-01 compared to other homogenized alloys shown in Fig. 4-8 and makes the γ''/γ' precipitate readily.

5.0 Microstructure and Mechanical Property Evolution During Isothermal Aging Processes

The previous chapters have shown that high-temperature homogenizations at 1180°C can effectively introduce recrystallization, remove columnar grain texture, and reduce the residual stress level in LPBF Inconel 718 alloys. Meanwhile, the homogenization conditions were found to affect the phase transformation behaviors during continuous cooling processes. Nevertheless, whether such high-temperature homogenizations are conducive to improving the mechanical property of LPBF Inconel 718 alloys after aging needs more verification, and how the homogenization process affects microstructure evolution during aging is not well studied. Therefore, specific research should be done to address the problems and to assist with optimizing the heat treatment for LPBF Inconel 718. In this chapter, in order to investigate the homogenization effects on the microstructure and property change after subsequent aging processes, two different homogenizations were firstly performed on LPBF Inconel 718 alloys and their effects on microstructure and property in aged samples were studied. The first homogenization process was selected at 1180°C for 1 h because it can effectively reconstruct grain morphology, reduce residual stress, and simultaneously keep refined grain size within a short time compared with other homogenization conditions, as shown in Chapter 3.2. It also has a relatively low phase fraction of NbC, indicating that a large amount of Nb is released into the γ matrix, which allows more strengthening phases to form during aging. It is thus presumed that the homogenization at 1180°C for 1 h can improve the anisotropy of microstructure and mechanical properties of the aged samples. In addition, the homogenization at 1065°C for 2 h was employed as a benchmark for comparison, because it is a representative homogenization process used for wrought or cast Inconel 718 alloys in industry, and the temperature is lower than the recrystallization temperature of

1100°C for LPBF Inconel 718. A single-step aging process at 718°C for 10 h was performed after each homogenization process to achieve a better understanding of the homogenization effects on the aging process. Based on the research results, an optimized heat treatment method was proposed, and the mechanical properties were investigated.

5.1 Impact of Homogenization on Microstructure-Property Relationships

This chapter is modified from the submitted journal paper: Y. Zhao, F. Meng, C. Liu, S. Tan, W. Xiong, Impact of homogenization on microstructure-property relationships of Inconel 718 alloy prepared by laser powder bed fusion, submitted to Mater. Sci. Eng. A.

5.1.1 Grain Structure Evolution

5.1.1.1 Grain Texture in the As-built Condition

In the present work, EBSD characterization was used to study the evolution of grain morphology and grain size. The sample notations in the work discussed in Chapter 5.1 are listed in Table 5-1. Figure 5-1 presents the grain morphologies of the as-built, homogenized, and aged samples along different directions. The grain morphologies in the as-built sample differ much on the different planes, which are shown in Figs. 5-1(a)&(b). On the XY plane (Fig. 5-1(a)), i.e., perpendicular to the build direction Z, the grains demonstrate an equiaxial shape. The large grains with diameters of around 70.5 μm are enclosed by small grains. Due to the strong temperature gradient in melting, on the XZ plane, i.e., along the build direction Z (Fig. 5-1(b)), the grain morphology is dominated by columnar shape with an average length of about 263.5 μm . As

mentioned in Chapter 3.1.1, the relatively larger columnar grains on the XZ plane consist of smaller sub-columnar and sub-equiaxial grains with Nb segregating along the grain boundaries and the Laves_C14 phase forming. The columnar grain texture developed can cause anisotropic mechanical properties with differences along directions parallel and perpendicular to the build direction [49,50].

Table 5-1. Sample notations and heat treatment conditions of the present work.

Sample/heat treatment notations	Heat treatment conditions
#AB	As-built
#H1180	1180°C-1h
#H1065	1065°C-2h
#HA1180	1180°C-1h+718°C-10h
#HA1065	1065°C-2h+718°C-10h

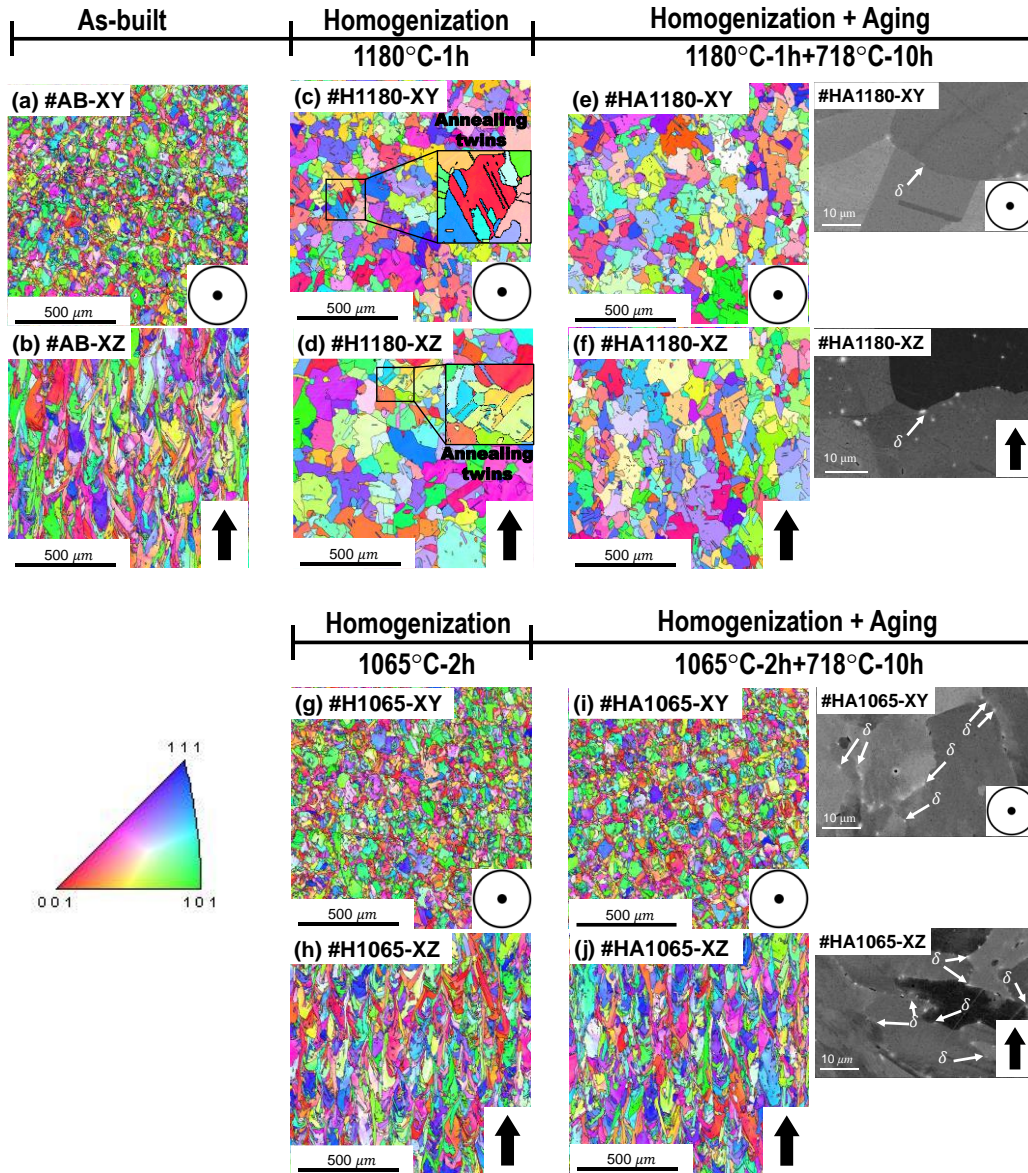


Figure 5-1. The Inverse Pole Figures (IPF) of the Inconel 718 samples. (a) XY plane, and (b) XZ plane of the as-built sample; (c) XY plane, and (d) XZ plane of sample #H1180 with 1180°C-1 h homogenization; (e) XY plane, and (f) XZ plane of sample #HA1180 with 718°C-10 h aging after 1180°C-1 h homogenization; (g) XY plane, and (h) XZ plane of sample #H1065 with 1065°C-2 h homogenization; (i) XY plane, and (j) XZ plane of sample #HA1065 with 718°C-10 h aging after 1065°C-2 h homogenization. The microstructures of the aged samples are shown in the SEM-BSE micrographs on the right-hand side of figures (e), (f), (i), and (j). The annealing twins in sample #H1180 are shown in Figs. 5-1(c)&(d).

5.1.1.2 Grain Texture Evolution After Homogenization

After homogenization under 1180°C for 1 h, according to Figs. 5-1(a)&(c) and Table 5-2, the average grain diameter of 29.5 μm on the XY plane of the sample #AB (as-built, Fig. 5-1(a)) increases significantly to 88.4 μm in sample #H1180 (Fig. 5-1(c)), whereas the grains keep the equiaxial shape. On the XZ plane, as shown in Figs. 5-1(b)&(d), the columnar grain texture in the as-built sample #AB (Fig. 5-1(b)) disappears after 1 h homogenization at 1180°C with the formation of the new equiaxial grains (Fig. 5-1(d)). The grain morphology change indicates the recrystallization has occurred and is almost finished after the homogenization. Hence, it can be inferred that the homogenization at 1180°C for 1 h leads to the equiaxial grain on both the XY and the XZ planes.

Table 5-2. Average grain size (diameter, μm) of samples on different planes.

Sample condition	As-built	1180°C-1 h	1180°C-1h+718°C-10 h	1065°C-2 h	1065°C-2 h+718°C-10 h
Observed plane	Perpendicular to the build direction Z (noted as XY plane)				
Sample label with plane	#AB-XY	#H1180-XY	#HA1180-XY	#H1065-XY	#HA1065-XY
Average grain size	29.5±19.2	88.4±50.9	92.0±56.9	32.7±22.4	30.7±19.2
Observed plane	Along the build direction Z (noted as XZ plane)				
Sample label with plane	#AB-XZ	#H1180-XZ	#HA1180-XZ	#H1065-XZ	#HA1065-XZ
Average grain size	61.4±38.0	129.1±67.3	94.5±54.3	49.0±31.6	54.1±41.5
Grain aspect ratio		1.46	1.03		

Moreover, some annealing twins can be readily observed after homogenization on both XY and XZ planes, as shown in the insets of Figs. 5-1(c)&(d). These twins can improve the strength and ductility of the materials [95,143], and can act as the nucleation sites of recrystallized grains

during homogenization to promote grain refinement [56]. However, a large number of twins will be harmful to the fatigue life of the materials [144] because cracks can easily nucleate at the twin boundaries. In addition, Zhang et al. [145] reported that twin boundaries in a Ni-based superalloy can be the sites where γ'' can precipitate abnormally as a V-shape with a coarsened size. This precipitation behavior can cause premature dislocation activities and pronounced strain localization at the twin boundaries, and consequently initiates cracks.

In order to quantitatively evaluate the grain morphology, the ratio of the average grain diameters on the XZ and XY planes of the homogenized sample #H1180 (1180°C for 1 h) was defined as the grain aspect ratio (GAR) and was used to determine the anisotropy of grain morphology. From Table 5-2, the GAR value of the homogenized sample #H1180 is 1.46, indicating that even though the recrystallization occurs in sample #H1180, the grains are still elongated to some extent along the build direction, the anisotropy of the recrystallized grains is not removed completely.

#HA1180 is the aged sample after homogenization at 1180°C for 1 h (#H1180). As shown in Figs. 5-1(e)&(f), the grain of sample #HA1180 remains equiaxial on both XY and XZ planes after aging at 718°C for 10 h. Table 5-2 shows that the average grain diameter on the XY plane in sample #HA1180 is 92.0 μm , which is close to the grain diameter of 88.4 μm on the XY plane of sample #H1180. Nevertheless, on the XZ planes, the grain diameter in #HA1180 is 94.5 μm , which is smaller than that in sample #H1180 that has an average grain diameter of 129.1 μm . The grain refinement observed after aging in sample #HA1180 is because the smaller recrystallized grains continuously grow during aging and consume the volume of larger grains of which the grain boundaries have been pinned by NbC particles and the grain growth is limited, as discussed in Chapter 3.2.2. The GAR value of sample #HA1180 is 1.03, which is smaller than that of 1.46 in

sample #H1180. The reduced GAR value in sample #HA1180 indicates that the anisotropy of grain morphology is further reduced after the aging process.

Similarly, the microstructure evolution in sample #H1065 (1065°C for 2 h) and its correspondingly aged sample #HA1065 (1065°C-2 h+718°C-10 h) are also analyzed. As shown in Figs. 5-1(g)&(h), the grain morphologies on XZ and XY planes in sample #H1065 are quite similar to that in the as-built sample #AB. Equiaxial and columnar grains are dominant on the XZ and XY planes, respectively. The results demonstrate that the homogenization at 1065°C for 2 h is not able to introduce recrystallization and reconstruct the grain morphology effectively. Figures. 5-1(i)&(j) show that after the further aging step at 718°C for 10 h, the grain morphology remains the same.

Besides causing the various grain morphology and grain size, the different heat treatments can also result in the change of grain boundary amount. Here, a parameter named grain boundary density (GBD) is used to study the evolution of grain boundary amount under different heat treatments, which is defined as

$$GBD = L_{GB}/S \quad (5-1)$$

where L_{GB} represents the total grain boundary length within a specific scan area and can be obtained from the EBSD results, and S represents the scan area.

Table 5-3. Grain boundary density (GBD, /m) of samples on different planes.

Sample condition	As-built	1180°C-1 h	1180°C-1 h+718°C-10 h	1065°C-2 h	1065°C-2 h+718°C-10 h
Observed plane	Perpendicular to the build direction Z (noted as XY plane)				
Sample label with plane	#AB-XY	#H1180-XY	#HA1180-XY	#H1065-XY	#HA1065-XY
Grain boundary density	21.15E4	8.31E4	7.97E4	20.39E4	20.00E4
Observed plane	Along the build direction Z (noted as XZ plane)				
Sample label with plane	#AB-XZ	#H1180-XZ	#HA1180-XZ	#H1065-XZ	#HA1065-XZ
Grain boundary density	15.25E4	5.19E4	7.72E4	17.19E4	16.55E4

Table 5-3 summarizes the GBD values on different planes of each sample. Regarding homogenized samples, on the XY plane, the GBD decreases from 21.15E4 /m of the as-built sample #AB (#AB-XY) to 8.31E4 /m of the sample #H1180 (#H1180-XY); on the XZ plane, the GBD value decreases from 15.25E4 /m of the as-built sample #AB (#AB-XZ) to 5.19E4 /m of the sample #H1180 (#H1180-XZ). After further aging at 718°C for 10 h, the GBD value on the XY plane in sample #HA1180 (#HA1180-XY) is 7.97E4 /m, which is comparable with the value of 8.31E4 /m in the homogenized sample #H1180 (#H1180-XY). However, on the XZ plane, the GBD value of sample #HA1180 (#HA1180-XZ) is 7.72E4 /m, which is increased from the 5.19E4 /m of sample #H1180 (#H1180-XZ). It is intriguing that, in contrast to the observation in samples #H1180 and #HA1180, the GBD shows a negligible reduction in samples #H1065 and #HA1065, which are homogenized at 1065°C for 2 h. According to Table 5-3, the GBD on the XY and XZ planes of sample #H1065 (#H1065-XY: 20.39E4 /m, #H1065-XZ: 17.19E4 /m) are close to the corresponding values in sample #AB (#AB-XY: 21.15E4 /m, #AB-XZ: 15.25E4 /m). This indicates the homogenization heat treatment at 1065°C for 2 h does not change the GBD of the sample. After the aging step, the GBD values in sample #HA1065 are also similar to their counterparts in sample

#H1065. A further comparison between the aged samples after different homogenization conditions from Table 5-3 indicates that the GBD on the XY and XZ planes in sample #HA1065 are $20.00E4$ /m and $16.55E4$ /m, respectively, which are more than double of the corresponding values in sample #HA1180 (#HA1180-XY: $7.97E4$ /m, #HA1180-XZ: $7.72E4$ /m). Overall, the change of GBD is consistent with the grain size evolution in different heat treatment steps, and fine grains are prone to have higher GBD. Moreover, the homogenization at 1180°C enables more effective grain morphology reconstruction and anisotropy elimination.

In order to investigate the relationships between the secondary phase precipitation and grain morphology, the SEM-BSE images of the aged samples are given on the rightest side of Fig. 5-1. As can be seen in the SEM figures, the detrimental δ precipitates form along grain boundaries during the aging processes [22,142]. On the XZ plane, the number density of δ particles of sample #HA1180 is $9.54\pm 2.7E8$ /m², which is less than the value of $4.96\pm 0.54E9$ /m² in sample #HA1065. The reduction of δ particles in sample #HA1180 is mainly due to the lower GBD value than that in sample #HA1065. The same conclusions can also be made on the XY plane. Therefore, it can be concluded that the homogenization at a higher temperature of 1180°C can efficiently suppress the precipitation of the δ phase with improved material properties.

5.1.2 Evolution of the Residual Stress

The cyclic rapid heating and cooling of LPBF with large temperature gradients can easily introduce residual stresses [40,146], which will promote crack propagation and thus degrade the material properties. Therefore, isothermal heat treatments [42] are usually applied to reduce the residual stress, which can be evaluated using grain orientation spread (GOS) [147–149] through EBSD characterization.

The GOS maps and the average GOS values of each sample obtained from EBSD are shown in Fig. 5-2 and Table 5-4, respectively. The as-built sample #AB has a relatively higher residual stress level. Its XY plane (#AB-XY in Table 5-4) has an average GOS value of 2.10° , and the XZ plane (#AB-XZ) has an average value of 2.39° . After homogenization at 1180°C for 1 h (Figs. 5-2 (c)&(d)), the GOS level is notably reduced due to the recrystallization, which implies the residual stress has been decreased by the homogenization at 1180°C . In sample #H1180, the average GOS value becomes 0.63° and 0.57° (Table 5-4) on the XY plane and XZ plane, respectively. The reduction of GOS on the XZ plane after the homogenization is more significant than that on the XY plane. After the aging process at 718°C for 10 h, the GOS values on the XY and XZ planes (#HA1180-XY: 0.35° , #HA1180-XZ: 0.34°) are further decreased in sample #HA1180 compared with that in sample #H1180, indicating the aging process is also contributing to the residual stress reduction.

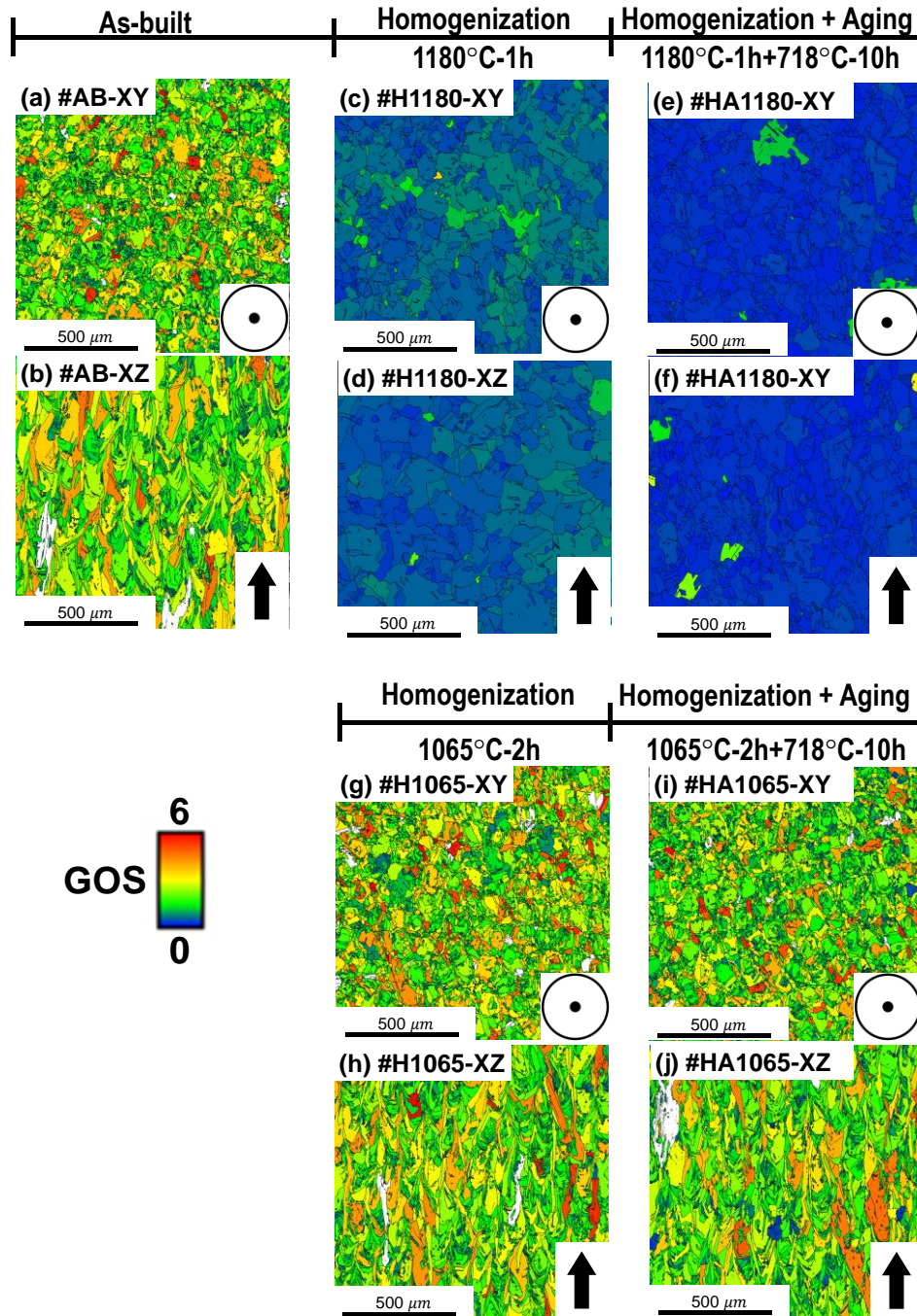


Figure 5-2. The Grain Orientation Spread (GOS) of the Inconel 718 samples. (a) XY plane, and (b) XZ plane of the as-built sample; (c) XY plane, and (d) XZ plane of sample #H1180 with 1180°C-1 h homogenization; (e) XY plane, and (f) XZ plane of sample #HA1180 with 718°C-10 h aging after 1180°C-1 h homogenization; (g) XY plane, and (h) XZ plane of sample #H1065 with 1065°C-2 h homogenization; (i) XY plane, and (j) XZ plane of sample #HA1065 with 718°C-10 h aging after 1065°C-2 h homogenization.

Table 5-4. Average grain orientation spread (GOS, °) of samples on different planes.

Sample condition	As-built	1180°C-1 h	1180°C-1 h+718°C-10 h	1065°C-2 h	1065°C-2 h+718°C-10 h
Observed plane	Perpendicular to the build direction Z (noted as XY plane)				
Sample label with plane	#AB-XY	#H1180-XY	#HA1180-XY	#H1065-XY	#HA1065-XY
Average GOS	2.1±0.91	0.63±0.18	0.35±0.23	2.39±1.03	2.19±1.09
Observed plane	Along the build direction Z (noted as XZ plane)				
Sample label with plane	#AB-XZ	#H1180-XZ	#HA1180-XZ	#H1065-XZ	#HA1065-XZ
Average GOS	2.39±1.04	0.57±0.14	0.34±0.26	2.40±1.14	2.28±1.08

In contrast to the significant GOS reduction in the samples after homogenization at 1180°C for 1 h, from Fig. 5-2 and Table 5-4, the GOS values in sample #H1065 homogenized at 1065°C for 2 h are comparable with the as-built sample on both XY (Fig. 5-2(g)) and XZ (Fig. 5-2(h)) planes (#H1065-XY: 2.39°, #H1065-XZ: 2.4°). After the following aging process, the GOS level of sample #HA1065 (#HA1065-XY: 2.19°, #HA1065-XZ: 2.28°) is still close to that of the as-built sample and sample #H1065. The GOS evolution in homogenized samples #H1065 demonstrates that the lower-temperature homogenization is not able to effectively eliminate the residual stress in the LPBF Inconel 718 alloys.

5.1.3 Phase Transformations during Aging Processes

The strengthening phases of γ'' and γ' usually precipitate during aging of Inconel 718 at the intermediate temperature (around 718°C) [150–152]. The γ'' phase forms as the principal strengthening particle [8], which tends to grow along the [100] and [010] directions, whereas the growth along the [001] direction is limited. Because the lattice mismatches along [100] and [010]

directions usually have the smallest level of ~0.56% comparing with the [001] direction, which can approach ~3% [53]. Such growth characteristics lead the γ'' to be plate-shaped [53], which is simply sketched in Fig. 5-3(a). The three possible variants of γ'' with their orientation relationships with the γ matrix are:

Type I: $(100)\gamma''[001]\gamma''// (100)\gamma[001]\gamma$

Type II: $(100)\gamma''[001]\gamma''// (010)\gamma[100]\gamma$

Type III: $(100)\gamma''[001]\gamma''// (100)\gamma[010]\gamma$

As shown in Fig. 5-3(b), three variants of γ'' particles with different orientations are usually observed in Inconel 718 prepared by conventional manufacturing. It is found by Qin et al. [53] that, when external tension is applied, the stress applied to the Inconel 718 alloys during the aging process can promote the growth of the γ'' precipitates with the short axis parallel to the tensile direction as illustrated in Fig. 5-3. From Fig. 5-3(c), such an applied tension increases the lattice constant of γ matrix along the tensile direction (i.e., [001] in Fig. 5-3(c)) with reduced lattice mismatch with the [001] direction of the type I γ'' precipitate. Therefore, only the type I precipitate will grow during the coarsening stage, and types II and III will dissolve gradually. Such an intriguing orientation preference of precipitation formation can be also observed in samples after homogenization in this work. As shown in Fig. 5-4, the γ'' precipitates form during homogenization under 1180°C (sample #HA1180) show three variants (Fig. 5-4(a)), whereas only one variant of γ'' is dominant under 1065°C (sample #HA1065) (Fig. 5-4(c)). Although no external tension has been applied to both samples, the residual stress evaluated through the GOS maps (Fig. 5-2) is inferred to be the main cause for such a difference. Homogenization at 1180°C can effectively release residual stress (Figs. 5-2(c)&(d)), while the high residual stress with the homogenization at 1065°C for 2 h promotes the coarsening of γ'' with monotonic increase of aspect ratio.

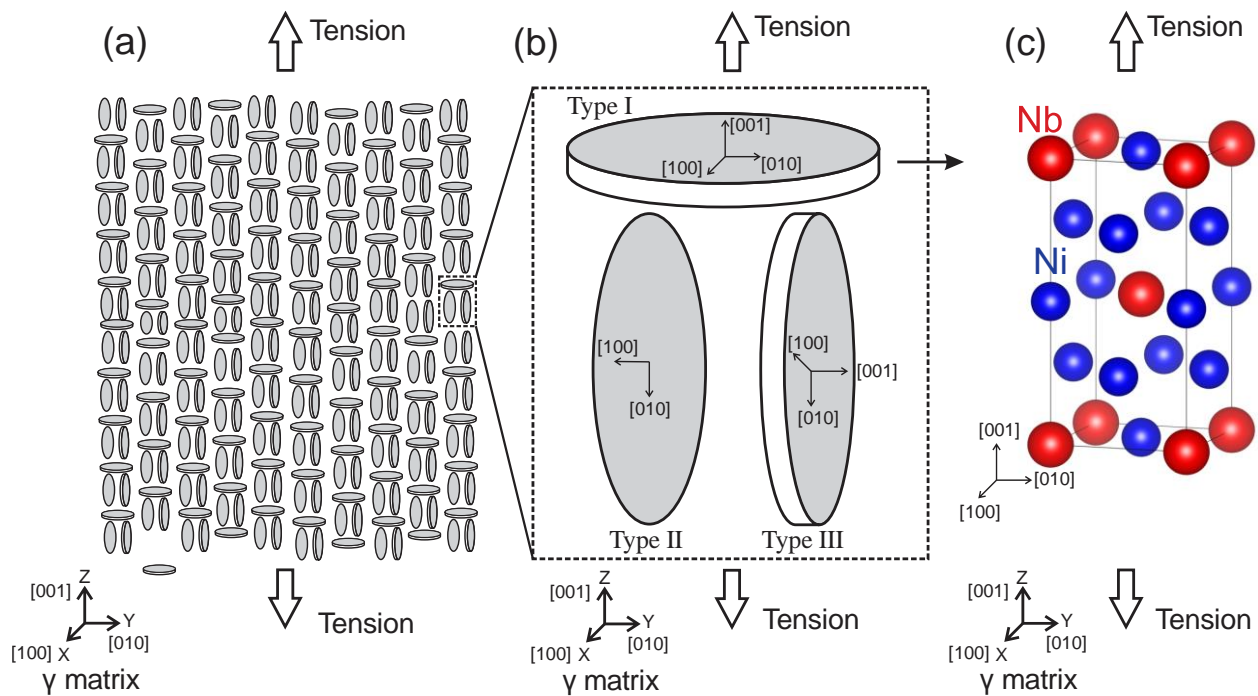


Figure 5-3. Schematic of the single variant γ'' coarsening process under applied stresses. (a) Stress states of the three variants of γ'' under tension in the γ matrix; (b) magnified schematic of the stress states of the γ'' variants; (c) stress states of the unit cell of a Type I γ'' particle.

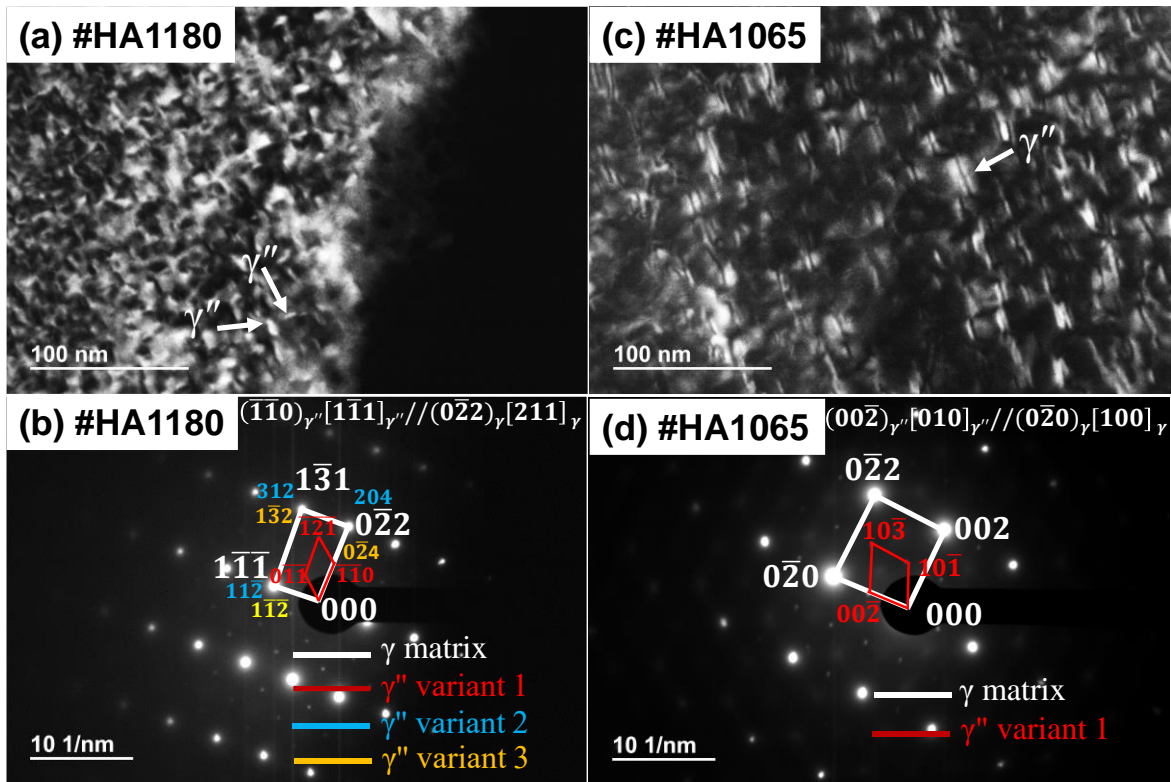


Figure 5-4. TEM analysis for aged alloys at 718°C for 10 h after different homogenizations. (a) Dark field image and (b) selected area electron diffraction pattern of sample #HA1180, which has been homogenized at 1180°C for 1 h; (c) Dark field image and (d) selected area electron diffraction pattern of sample #HA1065, which has been homogenized at 1065°C for 2 h.

5.1.4 Mechanical Properties

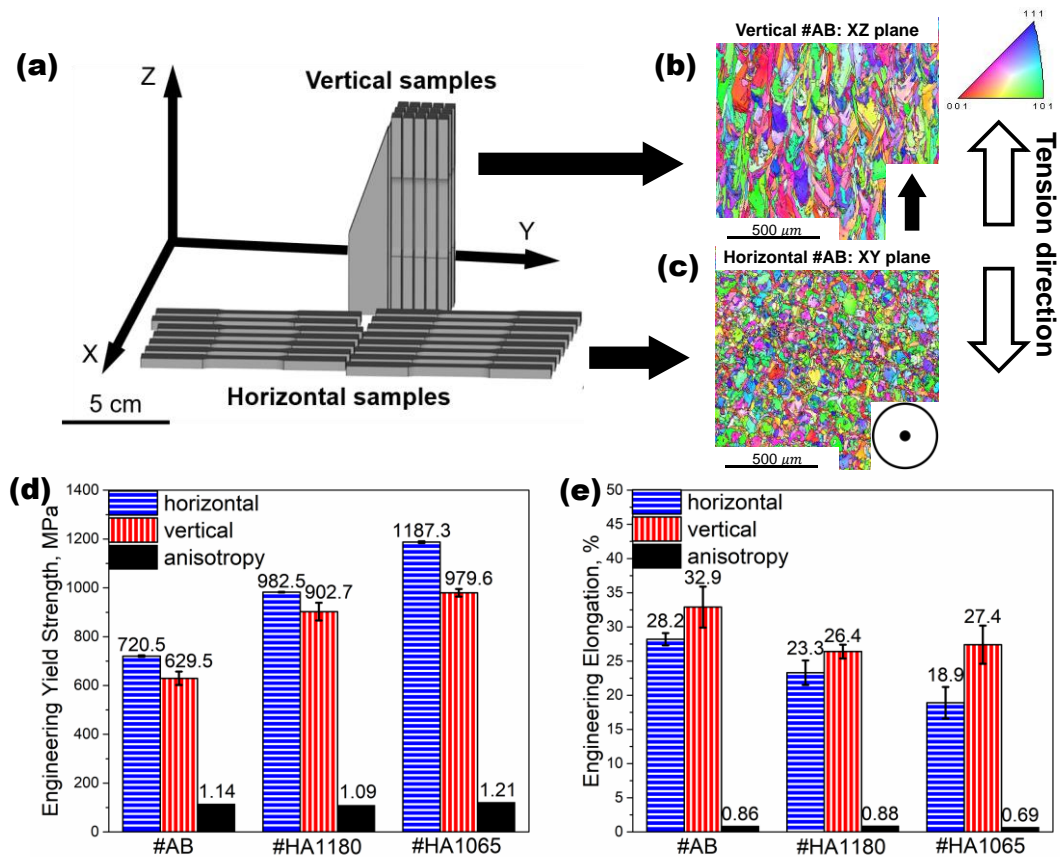


Figure 5-5. Illustration of the process-structure-property relationships of the LPBF Inconel 718 tensile bars.

(a) Demonstration of the vertically and horizontally printed tensile bars; illustration of the relationships between grain morphology and tensile direction for (b) vertical and (c) horizontal tensile bars (taking the as-built samples as examples); (d) engineering yield strength and (e) engineering elongation of horizontal and vertical tensile bars with various heat treatments.

As sketched in Fig. 5-5(a), tensile bars were manufactured both horizontally (perpendicular to the build direction) and vertically (parallel to the build direction). Heat treatments of #HA1180 and #HA1065 listed in Table 5-1 were performed on both types of tensile bars. Tensile tests were conducted to further quantify the processing impacts on mechanical properties. The as-built tensile

bars were used to benchmark the tensile tests. Figures 5-5(d)&(e) indicate the dependence of mechanical properties on build direction. The yield strength of the horizontal samples is higher than that in the vertical samples. Meanwhile, the elongation shows a reversed trend from Fig. 5-5(e) due to the strength-ductility trade-off.

Although phase stability is similar without notable difference in both horizontally and vertically built tensile bars, Figs. 5-5(b)&(c) taken by EBSD show a distinct difference of grain morphology on the planes parallel to the tensile direction, which leads to anisotropic mechanical properties. According to Fig. 5-5(b), the grain morphology on the XZ plane of the vertical sample will determine its tensile properties, whereas the grain morphology on the XY plane (Fig. 5-5(c)) will impact the tensile properties of the horizontal sample. From Figs. 5-5(b)&(c) and Table 5-2, the average grain size (29.5 μm) on the XY plane of the horizontal sample #AB is smaller than that (61.4 μm) on the XZ plane in the vertical sample #AB; thus, the horizontal sample has a higher yield strength than the vertical sample (Fig. 5-5(d)) due to the Hall-Petch effect. Because of the same reason, the higher GBD (21.15E4 /m, #AB-XY in Table 5-3) on the XY plane in the horizontal sample #AB (Fig. 5-5(c)) compared with that (15.25E4 /m, #AB-XZ in Table 5-3) on the XZ plane in the vertical sample #AB (Fig. 5-5(b)) can increase the probability of opening cracking [50] and promotes failure of the horizontal sample #AB during the tensile test, which results in a lower elongation of this sample.

Moreover, the comparison between Figs. 5-5(d)&(e) indicates the tensile properties of samples with the same build direction can be influenced by different heat treatments. It can be found from Fig. 5-5(d) that, due to γ'' precipitation during aging, yield strength gets improved in both heat treatments of 1180°C-1 h+718°C-10 h (#HA1180) and 1065°C-2 h+718°C-10 h (#HA1065). Additionally, since the aged sample #HA1065 has a smaller average grain size than

that of the sample #HA1180 (Table 5-2), the heat treatment with a low-temperature homogenization at 1065°C for 2 h can result in the highest yield strength values in both the horizontal and vertical samples as indicated by Fig. 5-5(d).

The elongation results shown in Fig. 5-5(e) present that the highest elongation (28.2%) among the horizontal samples is achieved in the as-built sample, whereas the heat treatment of sample #HA1065 leads to the lowest elongation (18.9%). For the vertical samples, the as-built condition still leads to the highest elongation of 32.9%, whereas the heat treatment of 1065°C-2 h+718°C-10 h (#HA1065) introduces a higher elongation than the heat treatment of 1180°C-1 h+718°C-10 h (#HA1180). This is because the elongation direction of the columnar grains on the XZ plane in vertical samples #HA1065 is parallel to the tensile direction, which is similar to the case shown in Fig. 5-5(b), impeding the initiation and propagation of the opening cracking and thus leads the sample to be more ductile. Besides, as discussed by Koyama et al. [50,153], the roughness-induced crack termination mechanism can also retard the cracking and improve the ductility of the vertical samples #HA1065 with the heat treatment of 1065°C-2 h+718°C-10 h.

The anisotropic property was evaluated through the ratios of the mechanical properties between horizontal and vertical tensile bars as shown in Figs. 5-5(d)&(e). Such a ratio value equaling 1 represents an ideal isotropic case. Evidently, sample #HA1180 subject to 1180°C-1 h+718°C-10 h can cause the highest isotropy on both yield strength and elongation. The as-built samples have the intermediate anisotropy, whereas the heat treatment of 1065°C-2 h+718°C-10 h makes the sample #HA1065 own the highest anisotropy. The higher anisotropy of tensile property in sample #HA1065 than the as-built sample #AB can be explained by the contribution from the single γ'' variant observed in sample #HA1065 (Fig. 5-4(c)), as these two kinds of samples share

similar grain morphologies. This observation implies the growth of γ'' along a single variant under the residual stress could increase the property anisotropy of LPBF fabricated Inconel 718.

5.2 Optimization of Heat Treatment

In this chapter, the post-heat treatment strategies of Inconel 718 processed by LPBF were optimized based on the results of Chapter 5.1 and industrial heat treatments. The microstructure evolution and mechanical properties of the heat-treated alloys were studied.

5.2.1 Post-Heat Treatment Optimization Based on Microhardness Testing

As shown in Fig. 5-6, the optimization of the heat treatment was based on the homogenization of 1180°C for 1 h, which was found to effectively remove the columnar grain texture introduced during the laser melting process and initiate recrystallization to reduce residual stress and improve the isotropy of grain morphology, as discussed in Chapters 3.2 and 5.1. Following the traditional two-step aging strategy of Inconel 718 alloy, this work re-optimized the combination of the aging temperature and time for the LPBF alloys. For the first aging process, two aging temperature candidates, i.e., 760°C and 718°C were selected based on the traditional aging processes [27–29]. Aging times of 5 h, 10 h, and 15 h were studied under each aging temperature and the Vickers hardness testing of each condition was conducted to determine the optimal aging strategy for the aging step. These three aging times were selected to cover the time ranges that are usually utilized in industry and meanwhile to avoid an overlong duration for energy efficiency. Based on the results of the first-step aging process, various combinations of temperature

and time were tested for the second aging step and the one resulting in the highest hardness was determined as the optimized heat treatment strategy.

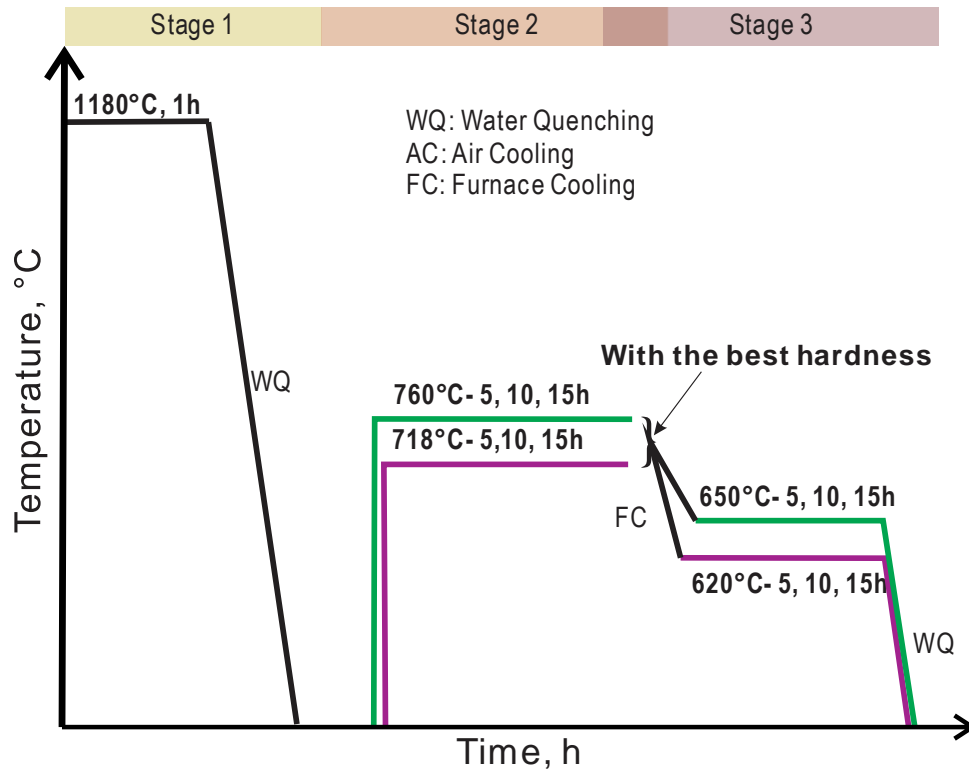


Figure 5-6. Temperature profiles of the heat treatment optimization process.

The Vickers hardness testing results are summarized in Fig. 5-7. From Fig. 5-7(a), under the homogenization condition of 1180°C for 1 h, the temperature and time combination that results in the highest hardness during the first step of aging was determined to be 718°C for 15 h, which could generate a hardness value of 481 HV. Figure. 5-7(b) shows that the second step of aging at 650°C for 10 h can generate the highest hardness with a value of 499.5 HV, which is significantly higher than that in the wrought or cast Inconel 718 alloys treated by various standards [20,27,154]. Hence, it can be concluded that the optimized post-heat treatment strategy under the homogenization of 1180°C-1 h is determined as 1180°C-1 h+718°C-15 h+650°C-10 h.

Microstructure characterization was conducted on the samples after optimized heat treatments with 1 or 2-step aging processes. The sample/heat treatment notations are listed in Table 5-5.

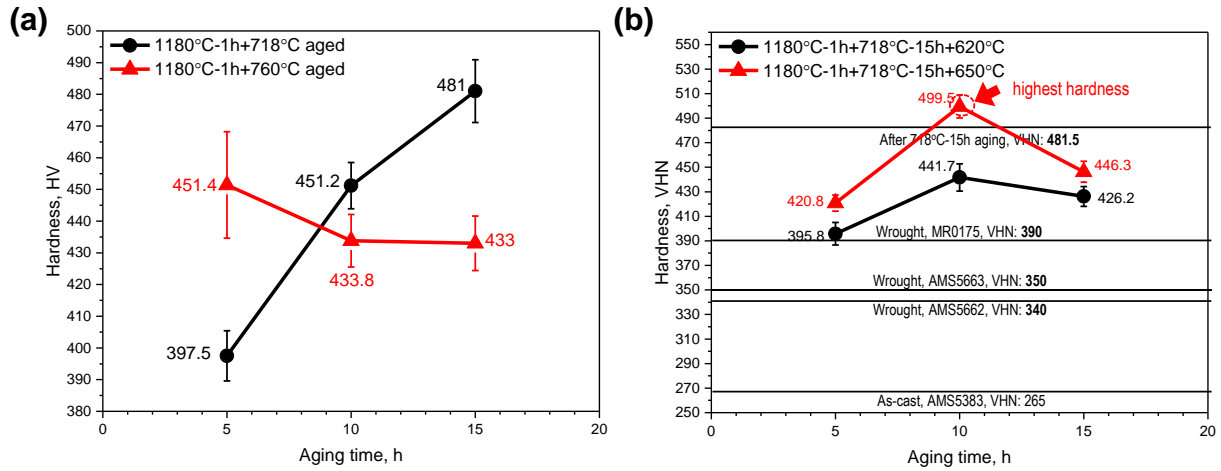


Figure 5-7. Hardness testing results for heat treatment optimization.

Table 5-5. Sample notations and heat treatment conditions.

Sample/Heat treatment notation	Heat treatment conditions
HA1180	1180°C-1 h+718°C-15 h
HAA1180	1180°C-1 h+718°C-15 h+650°C-10 h

5.2.2 Microstructure after Optimized Heat-Treatment

The grain morphologies of the optimized aged samples are demonstrated in Fig. 5-8. From Figs. 5-8(a)&(c), the grains in the samples HA1180 and HAA1180 become completely equiaxed and no columnar grain texture can be found. This is because the homogenization process at 1180°C for 1 h has effectively introduced the recrystallization and removed the columnar grain texture, as

discussed in Chapters 3.2 and 5.1. The grain sizes of the two aged samples are comparable with each other, with $167.53 \pm 114.97 \mu\text{m}$ for sample HA1180, and $156.74 \pm 88.98 \mu\text{m}$ for sample HAA1180, respectively (Table 5-6), indicating a further decrease in grain size happens after the second step of aging. However, the grain size of the aged samples was found to be larger than that in the 1180°C -1 h homogenized sample ($129.1 \mu\text{m}$, Table 5-2), indicating the aging processes in the current work can increase the grain size moderately.

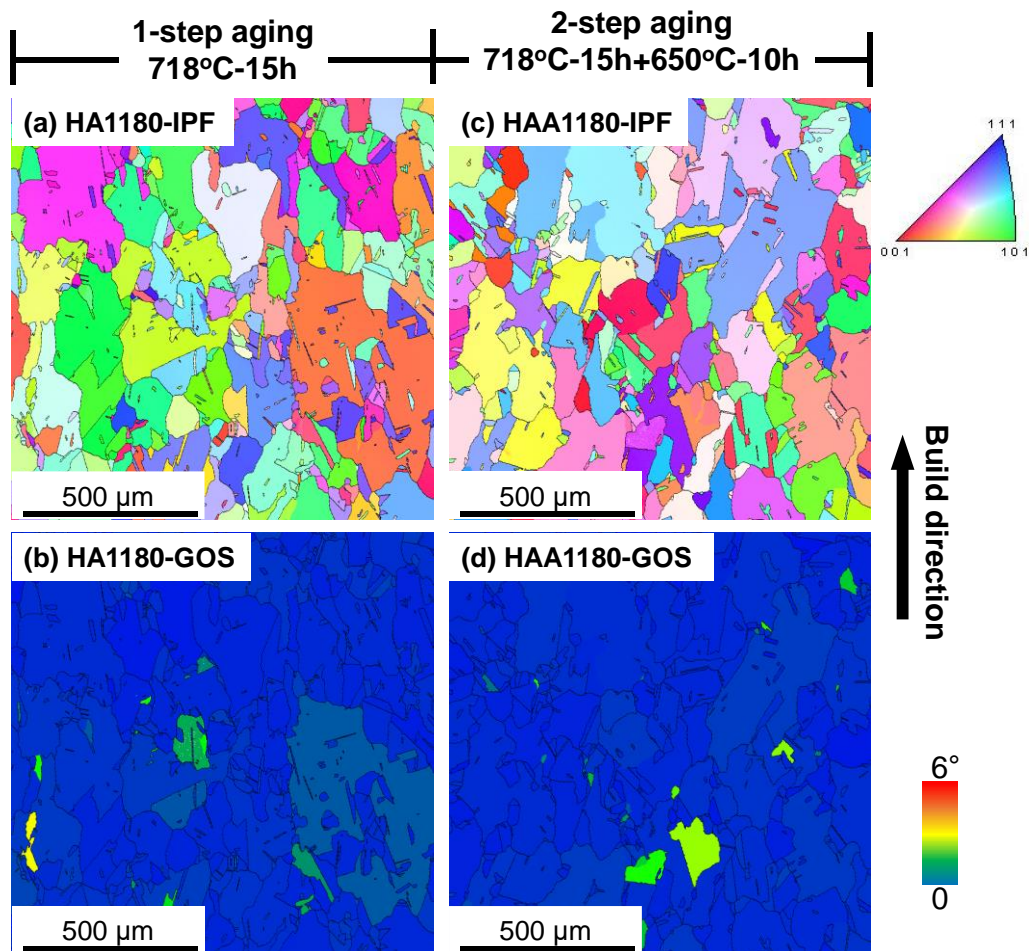


Figure 5-8. (a) Inverse Pole Figure (IPF) and (b) Grain Orientation Spread (GOS) map of sample HA1180 with 718°C -15 h aging after homogenization of 1180°C -1 h; (c) IPF and (d) GOS map of sample HAA1180 with 718°C -15 h+ 650°C -10 h after homogenization of 1180°C -1 h.

Table 5-6. Summary of grain and precipitate properties in the optimized aged samples.

Sample	Average grain size, μm	Average GOS, $^{\circ}$	Mean particle length of γ'' , nm	γ'' particle number density, $/\text{m}^2$
HA1180	167.53 \pm 114.97	0.31 \pm 0.19	16.5 \pm 3.2	6.56E14
HAA1180	156.74 \pm 88.98	0.27 \pm 0.05	18.5 \pm 3.4	8.76E14

The residual stress of the heat-treated samples was revealed by the GOS obtained from EBSD. It can be clearly seen from Figs. 5-8(b)&(d) and Table 5-6 that the aged samples HA1180 and HAA1180 have low average GOS values of 0.31 $^{\circ}$ and 0.27 $^{\circ}$, respectively, which means these aged samples after homogenized at 1180 $^{\circ}\text{C}$ for 1 h are almost stress-free. Moreover, the GOS values after the aging processes are further reduced compared to that of 0.57 $^{\circ}$ in the 1180 $^{\circ}\text{C}$ -1 h homogenized sample (Chapter 5.1.2), inferring the aging process can further assist with reducing the residual stress, which is consistent with the observation discussed in Chapter 5.1.2.

The SEM and TEM characterizations are conducted to further investigate the phase transformations in aged samples. As can be seen in Fig. 5-9, the Nb-rich phases (shown as bright phases in the SEM-BSE images), i.e., the NbC carbides and δ phase, are observed to form in the aged samples, and the δ mainly precipitates along grain boundaries. The phase fractions of the NbC and δ keep almost unchanged after the 2-step aging compared to that in the 1-step aged sample, whereas the fractions of these phases are low in both samples.

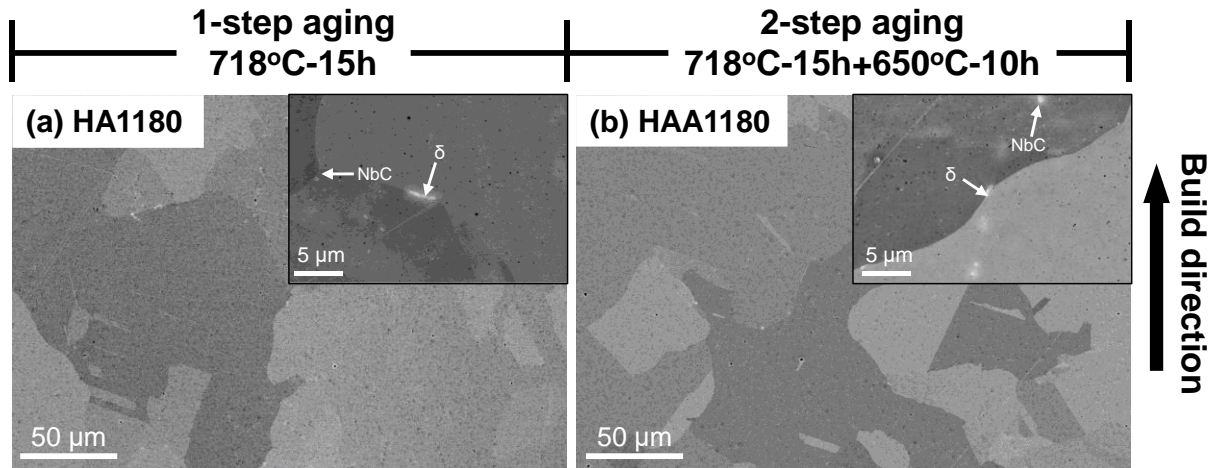


Figure 5-9. SEM images of (a) sample HA1180 with 718°C-15h aging after homogenization of 1180°C-1h; (b) sample HAA1180 with 718°C-15h+650°C-10h after homogenization of 1180°C-1h.

The precipitation attributes of the major strengthening γ'' phase were investigated by TEM characterization, as shown in Fig. 5-10, in which the “coffee-bean” contrast in the images indicates the γ'' precipitates in the aged samples are coherent or semi-coherent with the γ matrix, which generates a strain field around the particles and introduces the strengthening effects. It should be noted that the typical sphere-shaped γ' phase was not observed in the current study. The mean particle length and particle number density of γ'' phase are listed in Table 5-6. It can be found that the mean particle length of γ'' increases slightly from 16.5 nm of sample HA1180 to 18.5 nm of sample HAA1180 after 2-step aging, while it is still limited to a small value. However, the number density of the γ'' precipitates increases about 34%, i.e., from $6.56E14 /m^2$ to $8.76E14 /m^2$ with the 2-step aging applied. This is because the equilibrium status in the γ matrix is changed with the application of the second aging step at a decreased temperature, for which more hardening particles could precipitate [6]. Moreover, considering the slight particle growth after the second-step aging, the hardness increase observed in the samples with the second-step aging (Fig. 5-6) should mainly result from the increase of the number density of the strengthening particles.

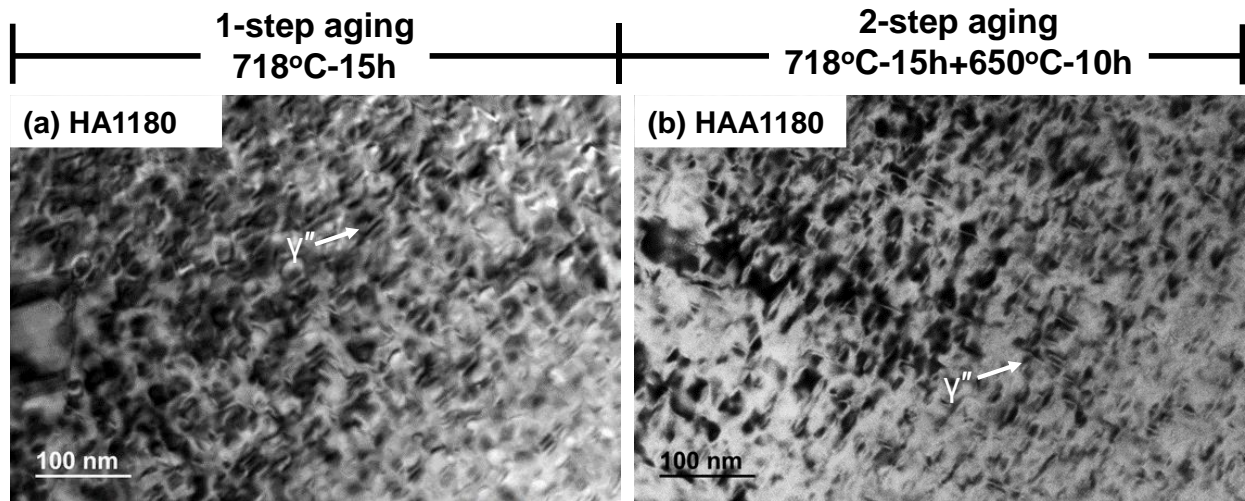


Figure 5-10. Brigh-field TEM images of (a) sample HA1180 with 718°C-15 h aging after homogenization of 1180°C-1 h; (b) sample HAA1180 with 718°C-15 h+650°C-10 h after homogenization of 1180°C-1 h.

5.2.3 Tensile Properties after Optimized Heat-Treatment

The mechanical properties of the two-step aged samples with the optimized parameters were evaluated by tensile testing. Both vertical and horizontal tensile bars were printed in the same way introduced in Chapter 5.1.4 to determine the anisotropy of mechanical properties. The definition of anisotropy has been given in Chapter 5.1.4. The optimized heat treatment of 1180°C-1 h+718°C-15 h+650°C-10 h (HAA1180) was applied to both vertical and horizontal tensile bars. The tensile properties of the samples are summarized in Table 3, which shows both the vertical and horizontal tensile bars own good yield strength and are superior to the as-built alloys as shown in Fig. 5-5(d). Meanwhile, good elongation properties are retained. The yield strength of the horizontal sample (1147.8 MPa) is higher than that of the vertical sample (1092.5 MPa), whereas the vertical sample has a better elongation because of the strength-ductility trade-off. Table 3 shows that the uncertainties of mechanical properties of the vertical sample are relatively low, with

0.8 MPa of the yield strength and 0.1% of elongation, respectively. However, although the horizontal sample has a low uncertainty of 0.6 MPa of yield strength, the uncertainty for the elongation property has a high value of 1.8%. The heat treatment HAA1180 results in a low anisotropy (1.05) of yield strength while the anisotropy of elongation is relatively higher (0.8). The high elongation anisotropy may be related to the high elongation uncertainty in the samples, but an ad-hoc study on this phenomenon should be further conducted.

Table 5-7. Tensile properties of samples with the optimized heat treatment.

Sample	Printing direction	Yield strength (YS), MPa	Elongation (EL), %	Anisotropy of yield strength	Anisotropy of elongation
HAA1180	Vertical	1092.5±0.8	20.6±0.1	1.05	0.8
HAA1180	Horizontal	1147.8±0.6	16.5±1.8		

Figure 5-11 illustrates the comparison of the mechanical properties of additively manufactured Inconel 718 alloys obtained from this work and the literature [3,155–159]. As can be seen in Fig. 5-11, the optimized heat treatment of 1180°C-1 h+718°C-15 h+650°C-10 h in this work can achieve good combinations of yield strength and elongation properties compared to other work in literature and retains low anisotropy properties among the alloys. Consequently, the heat treatment strategy proposed in this work can effectively improve the mechanical properties of Inconel 718 fabricated by LPBF and provides new perspectives for the post-processing design.

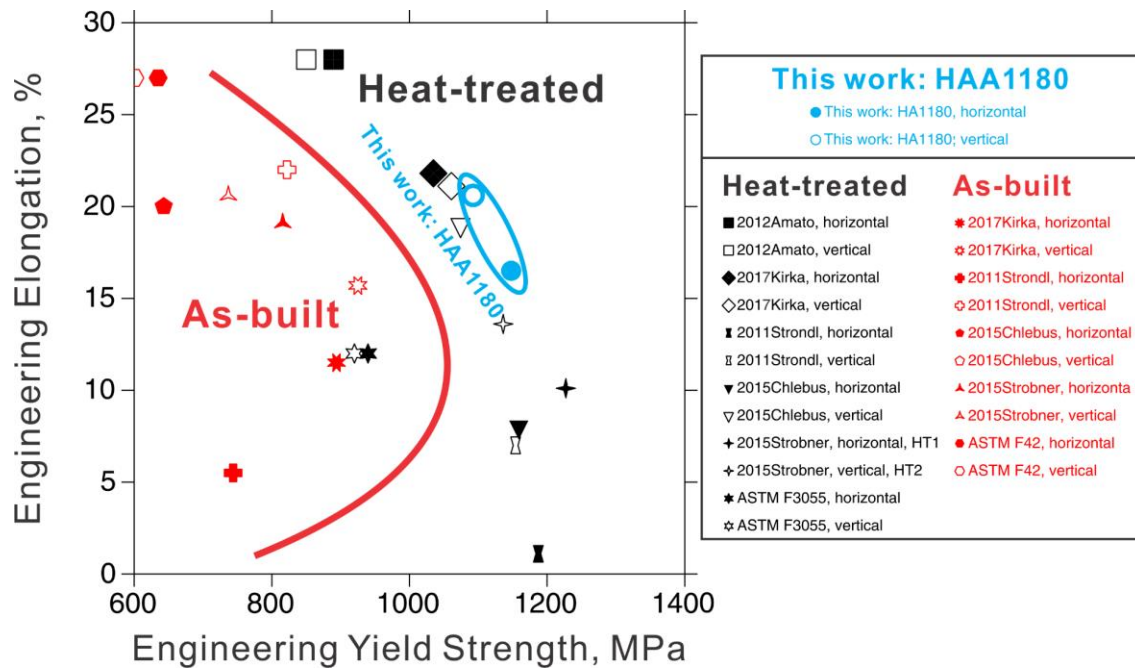


Figure 5-11. Comparison of the mechanical properties between the optimized heat treatments from this work and other studies in the literature.

6.0 Acceleration of Heat Treatment Development Using High-Throughput Experiment

This chapter is modified from the published journal paper: Y. Zhao, N. Sargent, K. Li, W. Xiong, A new high-throughput method using additive manufacturing for alloy design and heat treatment optimization, *Materialia*, 13 (2020) 100835 [160].

Composition design and post-heat treatment optimization are the two main aspects of materials development [19,161]. Materials Genome highlights the importance of the rapid generation of the database to accelerate materials development [19,162]. Therefore, high-throughput (HT) modeling and experiment are critical to design efficiency [163]. In additive manufacturing, the feedstock materials design becomes more important since more processing parameters can directly impact the structure-property relationships of the as-fabricated materials. In this chapter, an HT experiment was developed by coupling the LPBF technique with the gradient temperature heat treatment (GTHT) process [161,164] to effectively accelerate the post-heat treatment design of Inconel 718. The same concept and experimental setup can also be used for the post-heat treatment optimization of other alloys.

6.1 The Setup of the High-Throughput Experiment

In this work, a long-bar Inconel 718 sample was fabricated using the LPBF technique, as shown in Fig. 6-1(a). The Inconel 718 build was designed with twenty-three evenly distributed holes. These holes provided flexibility when choosing monitoring locations. In addition, the holes

increased the surface area of the sample and further improved the convection heat transfer, which reduced the variation in the sample temperature relative to the air temperature. As a result, the air temperature calibration became more representative of the real sample temperature, allowing the preemptive selection of the monitoring locations in the sample according to the actual needs. The flexibility of the setup of the high-throughput experiment was increased by adopting additive manufacturing methods for sample fabrication. Using this methodology, the current work significantly reduced the total time needed for heat treatment.

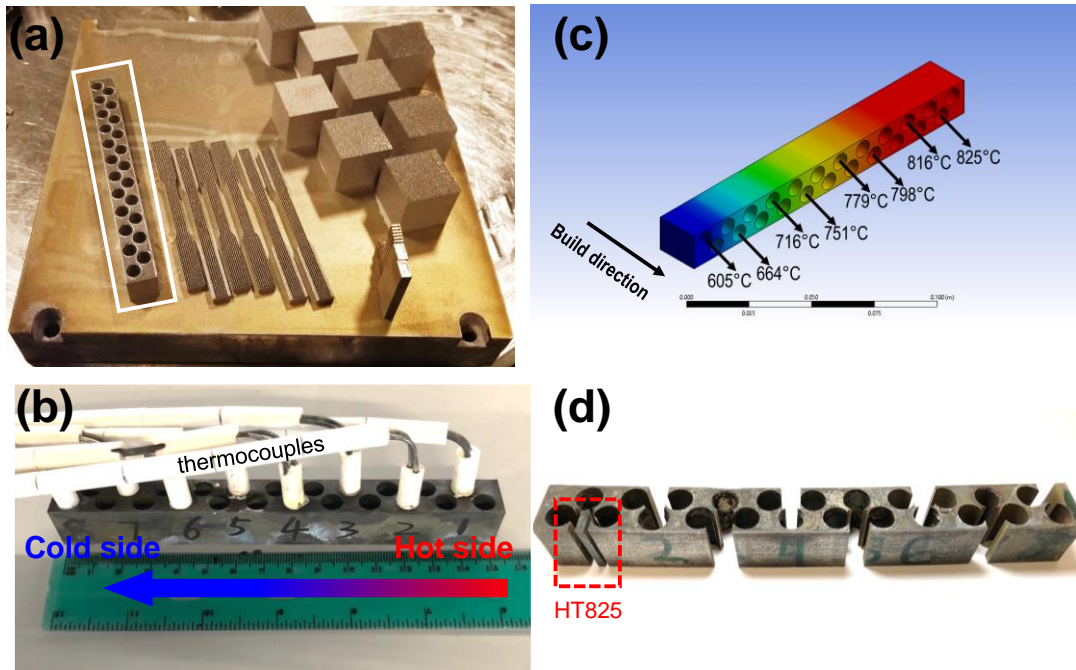


Figure 6-1. Setup of high-throughput experiments. (a) Inconel 718 build printed by LPBF; (b) setup of temperature record and illustration of sample cutting for microstructure characterization (taking sample HT825 as an example; the sample notations and the corresponding heat treatment are shown in Fig. 6-2); (c) setup of the furnace for the high-throughput experiment; (d) experimental temperature distribution inside the bar-sample.

The long bar build was firstly encapsulated in a quartz tube with a backfilled Ar protective atmosphere and then homogenized at 1180°C for 1 h to eliminate the microsegregation and the columnar grain texture from the LPBF process. The microstructures of the as-built sample and the sample homogenized at 1180°C for 1 h were discussed in Chapter 3. Afterward, the sample was quenched into ice water. Before conducting the HT aging heat treatment, eight K-type thermocouples were fixed into eight equidistantly distributed holes using conductive high-temperature cement, as shown in Fig. 6-1(b). The thermocouples were connected to a computer via a data acquisition system to record the aging temperatures at each location throughout the aging process. The uncertainty of the temperature control is $\pm 0.75\%$. The aging heat treatment was then carried out in a tube furnace with one end open to introduce gradient temperatures at different locations in the sample, as illustrated in Fig. 6-1(c). The furnace settings necessary to achieve the desired temperature gradient were calibrated by measuring the temperature as a function of position with a K-type thermocouple. Calibration of the temperature profile was kind of time-consuming as several attempts may be needed to find a good combination of the furnace settings and the plug location to obtain the desired temperature gradient. Thus, the HT experimental method described in this work mainly saves time for long-term heat treatments. It is important to note that the achievable temperature gradient will change depending on the furnace. Therefore, if an experiment must be reproduced, the same furnace and settings should be used. The furnace temperature settings and the position of the sample inside of the furnace tube had been deliberately calibrated to acquire a temperature gradient of 600~800°C, within which the δ , γ' , and γ'' phases can precipitate during the aging processes [165]. The temperature gradient during the aging process was stable without fluctuation, and the distribution of temperatures achieved at each monitored location is illustrated in Fig. 6-1(d). From Fig. 6-1(d), the experimentally obtained

temperature gradient was within 605~825°C, which agreed well with our expectation. The aging process lasted 15 h, followed by quenching into ice water thereafter. The temperature diagram of heat treatment in the present work and the corresponding sample notations are summarized in Fig. 6-2. The alloy located adjacent to each thermocouple (as shown in Fig. 6-1(b) with a highlighted case for HT825) were sectioned individually for microstructure characterization to determine the effect of different aging temperatures.

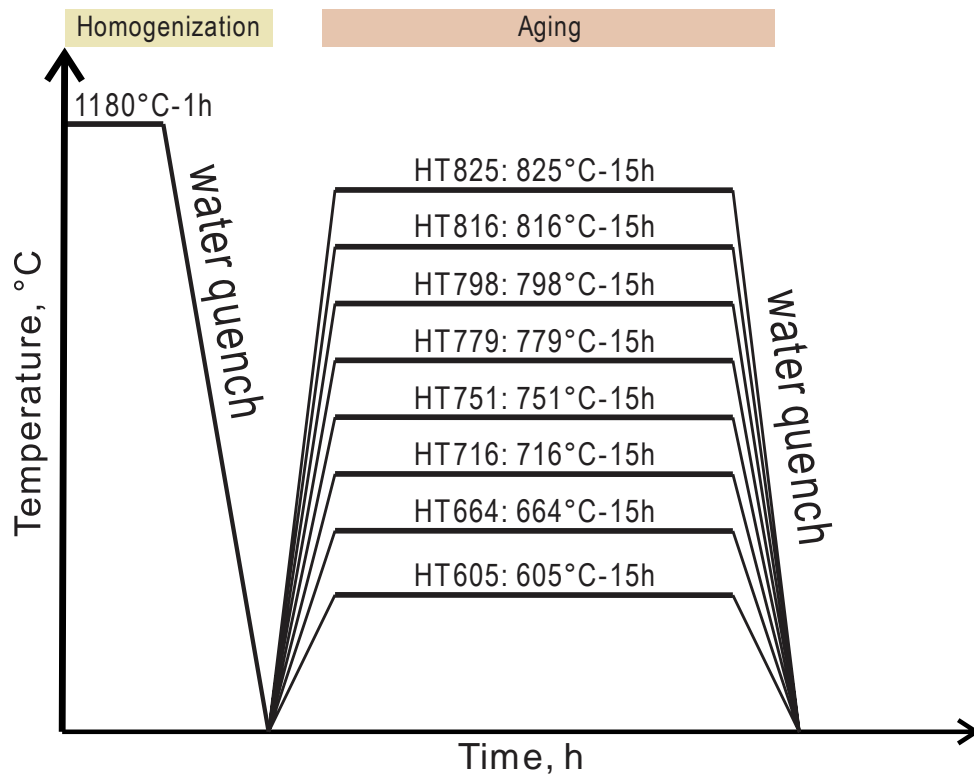


Figure 6-2. Temperature diagram of heat treatment with the corresponding sample notations used in this work.

6.2 Microstructure and Mechanical Property Characterization

EBSD characterization was performed on each aged sample to observe the grain morphology. As presented in Figs. 6-3(b)~(i), coarse grains can be found to form in all aged samples. The average grain diameters measured by EBSD, in a range of 160~210 μm , are plotted as a function of the corresponding aging temperatures in Fig. 6-3(a). The grain size is shown to be independent of the aging temperature. Such observation elucidates that the chosen aging temperatures do not cause significant effects on the grain size and morphology, which has not yet been observed in the studies on Inconel 718. Additionally, the relatively large grain size achieved after heat treatment in this study has little contribution to the microhardness variation.

According to the microhardness testing results shown in Fig. 6-3(a), three representative samples were selected for further microstructure investigation to understand the structure-property relationships: (1) the sample HT605 having the lowest microhardness of 248.4 HV; (2) the sample HT716 having the highest microhardness of 477.5 HV; and (3) the sample HT825 owning the lowest microhardness of 332.2 HV in the high-temperature gradient. As shown in the microstructure under SEM and TEM, Figs. 6-4(a)&(b), except a small amount of NbC carbides, no γ''/γ' and δ precipitates can be observed in the sample HT605. In sample HT716 (Fig. 6-4(d)), the 716°C-aging causes a small amount of the δ phase to precipitate along grain boundaries. However, a large number of plate-shaped γ'' particles were observed in the TEM micrographs (Figs. 6-4(e)&(f)). These γ'' particles are very fine with a mean particle length of 13.8 ± 4.2 nm through image analysis. The typical γ' phase with spherical shape was not found to precipitate in sample HT716. This indicates that the precipitation of γ'' preceded the formation of γ' in the current study. Therefore, the strengthening effect is dominated by γ'' with fine particle size. Figure 6-4(g) and its inset present significant precipitation of the δ phase along the grain boundaries in sample

HT825. As pointed out by the red arrows in the inset of Fig. 6-4(g), some δ particles were observed not to have habit planes parallel to the grain boundaries, and their growth is usually accompanied by grain boundary migration. Hence, the corresponding grain boundaries have a jagged appearance, as discussed in Ref. [142]. Figure 6-4(h) shows the γ'' particles in sample HT825 are significantly coarsened with a mean particle length of 303.9 ± 183.2 nm. Similarly to sample HT716, the γ' phase was not observable in sample HT825, which suggests the precipitation of γ' is still surpassed by γ'' during the aging at 825°C .

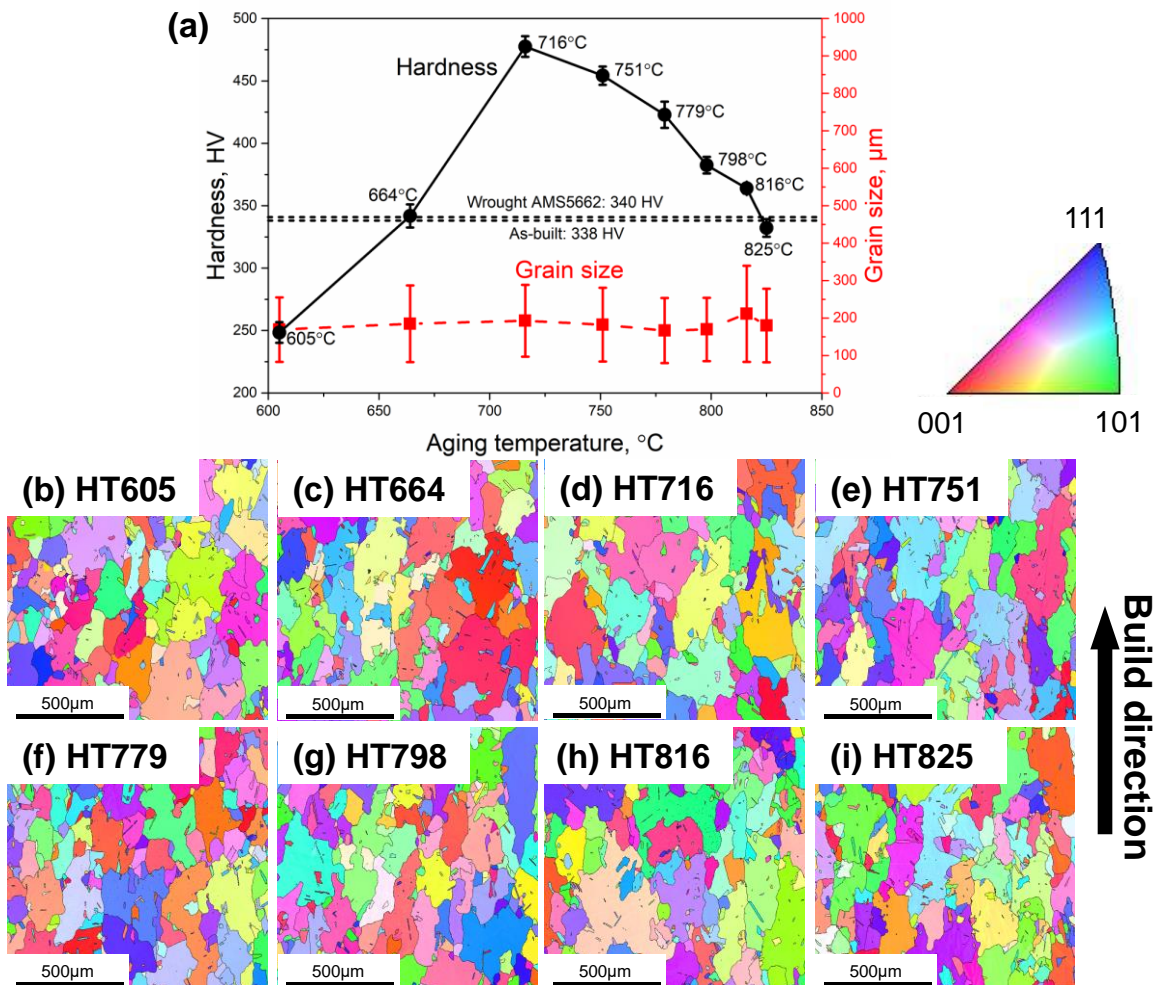


Figure 6-3. (a) Results of Vickers microhardness and average grain size measurements. IPFs of the aged samples with (b) HT605; (c) HT664; (d) HT716; (e) HT751; (f) HT779; (g) HT798; (h) HT816; (i) HT825.

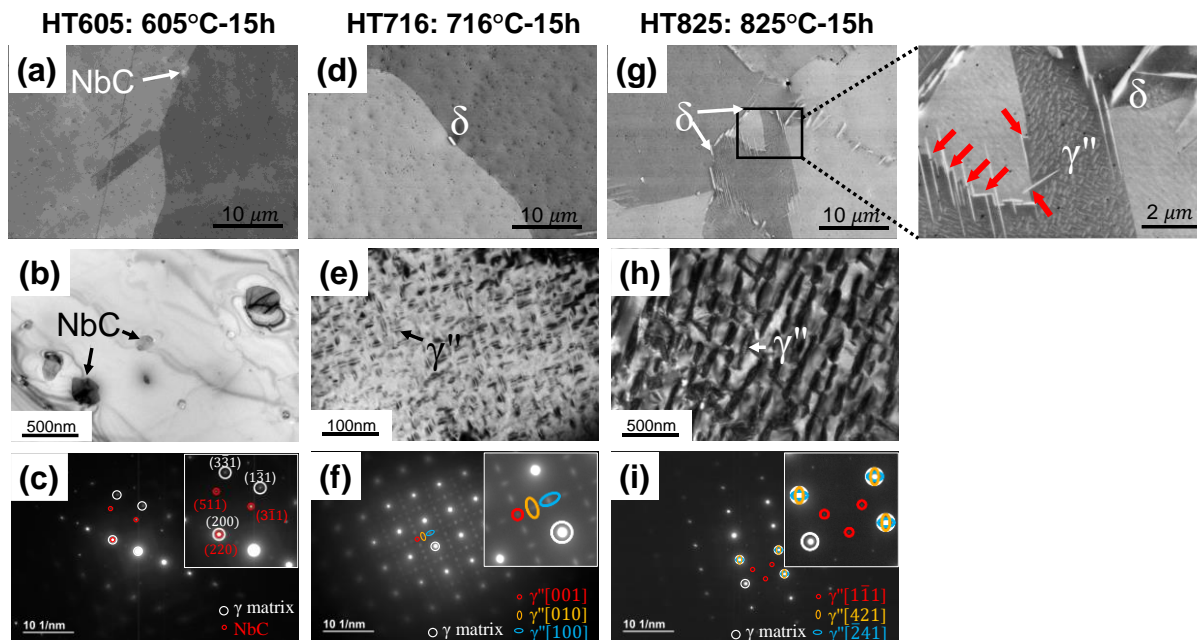


Figure 6-4. Microstructures of HT605 characterized by (a) SEM-BSE; (b) bright-field TEM; (c) selected-area-electron-diffraction (SAED). Microstructures of HT716 characterized by (d) SEM-BSE; (e) bright-field TEM; (f) SAED. Microstructures of HT825 characterized by (g) SEM-BSE; (h) bright-field TEM; (i) SAED. The different γ'' variants in (f) and (i) are shown by different colors, and the corresponding zone axes are indicated.

It is obvious that the different microhardness among the aged samples is due to the various phase transformation behaviors. According to Oblak et al. [166], the coherency strengthening stems from the γ'' phase is the primary mechanism for the hardening effects in Inconel 718. The coarsening of the γ'' precipitates can lead to coherency loss and can weaken the hardening effects [167,168]. The critical mean particle length of the γ'' for coherency loss was reported to be 80~120 nm [76,167–169]. Consequently, it can be inferred that the very fine γ'' particles with a mean particle length of 13.8 nm obtained in 716°C-aging primarily contribute to the highest microhardness, since their particle size is smaller than the critical size, and these particles have high coherency with the γ matrix [168]. Correspondingly, the microhardness reduction in sample

HT825 is mainly attributed to the coherency loss of γ'' [167,168], which is owing to the precipitates coarsening. Besides, the large amount of δ phase formed in sample HT825 is also considered to reduce the microhardness, because the δ precipitates have incoherent phase boundaries with the γ phase, which degrades the hardening effect in the alloy. However, in sample HT605, it is the absence of the strengthening phases that leads to the dramatically reduced microhardness, and this result suggests that the aging process at 605°C for 15 h is insufficient for the precipitation hardening in LPBF Inconel 718.

The aging temperature of 716°C with optimal microstructure is close to the widely used values of 718 or 720°C in the heat treatment of Inconel 718 [20,30], proving the validity in microstructure engineering of the proposed HT method. This work demonstrated that the high-throughput experiment coupling LPBF technique with GTHT can serve as an effective tool with flexibility to accelerate the post-heat treatment optimization and new alloy development for advanced manufacturing, especially for LPBF components.

7.0 Conclusions and Future Work

In this dissertation, the microstructure engineering during heat treatment of Inconel 718 Ni-based superalloys processed by laser powder bed fusion was studied using both modeling and experiments. The following conclusions can be drawn:

- Using DICTRA simulation, the homogenization time of the as-built Inconel 718 alloy was reasonably predicted. The calculated homogenization time from single-phase models with the composition of the Laves_C14 phase obtained using results from either EDS or calculation using the lever rule as input matched reasonably well with experimental observation. The predicted value is closer to the experimental value if the composition of the Laves_C14 phase is determined accurately. However, the single-phase model with the segregation profile determined from the Scheil simulations as the inputs could not give a reliable prediction. This is inferred to be due to the repeated thermal cycling during the LPBF process that results in a modified segregation profile, which deviated from that of the single solidification process predicted by Scheil simulation. The moving boundary simulations underestimated the homogenization time due to the lack of mobility data for the Laves_C14 phase for LPBF alloy. This necessitates the need for determining the mobility parameters for describing the Laves_C14 phase to extend the applicability of kinetic simulations using DICTRA to effectively estimate the homogenization time for different processing.
- A comparative analysis of the microstructure evolution at 1180°C in Inconel 718 alloys processed by suction casting and LPBF was performed. The initial

microstructures of the as-cast and as-built samples were different. Such a difference can influence the Nb homogeneity of the matrix. The Nb homogeneity increased in suction-cast alloys; whereas it decreased in LPBF alloys with increasing time during isothermal heat treatment at 1180°C. In suction-cast alloys, the Laves_C14 phase remained during 1 h (short-time) homogenization and dissolves after 12 h (long-time) homogenization. In LPBF alloys, the Laves_C14 phase dissolved completely within homogenization of 20 min accompanied by the growth of the NbC carbides, which continued during the entire homogenization process. Abnormal grain growth was observed in suction-cast alloys with increased homogenization time due to the dissolution of the Laves_C14 phase, while the grain growth was impeded, and the average grain size was even refined in LPBF alloys for longer homogenization durations. The grain refinement was attributed to recrystallization and the Zener pinning effect by NbC carbides. The columnar grain texture formed during the LPBF process can be removed effectively after 1 h homogenization at 1180°C. Multi-types of dislocation behaviors were observed in the homogenized LPBF alloys. The coherency loss due to the growth of NbC carbides and the release of local strains during homogenization process are two major factors contributing to the dislocation generation. Dislocations generated in the homogenized LPBF alloys were found to be arrays or loops, which can be interpreted by the intermediate stacking fault energy of Inconel 718. Both Orowan bowing and dislocation cutting mechanisms were found regarding the dislocation-precipitate interaction. The pileup of dislocations at grain boundaries can activate

new dislocation arrays in the adjacent grain, which is conducive to local strain relief and preventing the initiation of cracks.

- The CCT diagrams of LPBF Inconel 718 alloys after homogenizations at 1180°C for 20 min and 12 h were established based on microstructure characterization and dilatometry analysis. Corresponding CCT diagrams of suction-cast alloys were determined for comparison using the same method. NbC carbides and δ phase were found to precipitate during the continuous cooling process in all alloys at appropriate cooling rates. Both homogenization durations and manufacturing methods can affect the phase transformation behaviors, i.e., the starting temperature, the precipitation formation range, and the critical cooling rate, of the δ phase during cooling by changing the Nb homogeneity. The precipitation kinetics of the δ phase during cooling depended more on the nucleation process in alloys with higher Nb homogeneity, while the growth process was predominant in alloys with lower Nb homogeneity. Compared to the samples cooled at higher rates, the cooling rate of 0.1 K/s can achieve the highest hardness in all alloys with different homogenization durations and manufacturing conditions. This is deduced to be due to the formation of subgrains as a result of the abundant precipitation of δ phase. This work indicates that the ad-hoc design of a post-heat treatment for microstructure engineering of LPBF alloys is essential. A careful analysis of microstructure influenced by cooling processes is critical for the heat treatment design of LPBF alloys. Moreover, due to the effects of different homogenization and manufacturing on the CCT diagrams, for phase transformation modeling, the CCT diagram may not be the best choice to integrate with other thermal modeling

simulations to understand the microstructure evolution of Inconel 718 alloys in additive manufacturing with cyclic heating and cooling.

- The influence of homogenization conditions on the microstructure-property relationships during the subsequent aging processes in LPBF manufactured Inconel 718 was studied. It was found that the homogenization at 1180°C for 1 h can introduce complete recrystallization and removal of columnar grain texture. Meanwhile, the residual stress generated during the additive manufacturing process can be removed by the homogenization heat treatment, three variants of γ'' strengthening phase can precipitate during the aging process at 718°C for 10 h after homogenization, and the mechanical properties became isotropic. On the contrary, the traditional homogenization at 1065°C for 2 h and the following aging at 718°C for 10 h cannot change the grain morphology from the as-built sample, neither can the heat treatments effectively reduce the residual stress. During the aging process after 1065°C-2 h homogenization, one variant of the γ'' phase was found to be dominant, which is due to the relatively higher residual stress. The tensile tests demonstrated that under the same heat treatment conditions, the tensile bars printed horizontally had higher yield strength but lower elongation than the tensile bars printed vertically. The heat treatment of 1065°C-2 h+718°C-10 h achieved the highest yield strength among the sample tested, while the heat treatment of 1180°C-1 h+718°C-10 h achieved the highest isotropic mechanical properties. The results revealed that the homogenization conditions can significantly influence the microstructure evolution, affect the phase transformations during the aging steps, and change the isotropy of mechanical properties in LPBF Inconel 718 alloys. The

effects of homogenization on the microstructure and property evolution should be specifically considered when designing the post-heat treatment.

- The heat treatment of 1180°C-1 h+718°C-15 h+650°C-10 h was optimized based on the traditional heat treatments and the phase transformation research in the current work. It was found that the second aging step can improve the alloy hardness due to the increase in the number density of γ'' particles whereas the mean particle size only increased slightly. A good combination of strength and ductility were achieved in samples through the heat treatment of 1180°C-1 h+718°C-15 h+650°C-10 h; while good isotropy of tensile properties was maintained.
- A high-throughput experiment was designed by introducing a gradient temperature within LPBF Inconel 718 systems. The optimized aging temperature for the LPBF Inconel 718 was determined to be 716°C, which can result in the highest microhardness and is close to the industrial aging temperature of 718°C for wrought Inconel 718 alloys. The hardening effect at 716°C mainly stemmed from the refined particles of the principal strengthening phase γ'' ; whereas the coarsened particle size at high aging temperature or the slow precipitation kinetics at the low temperature of the γ'' phase degraded material hardness. Grain size was found to be independent of aging temperature between the investigated temperature range of 605°C to 825°C. This high-throughput method proved to be an effective tool for post-heat treatment optimization. The flexibility of the LPBF methods in printing various dimensions and geometries of samples can further expand its applicability in high-throughput experiments for new alloy development.

- In general, the present work was a comprehensive study on the microstructure engineering for LPBF Inconel 718 superalloy and revealed the process-structure-property relationships during various heat treatments. The microstructure and property evolution of LPBF Inconel 718 differed evidently from that of traditionally manufactured alloys. New post-heat treatment strategies should be specifically designed and optimized for LPBF Inconel 718 based on its microstructure characteristics to achieve improved material properties. The high-throughput method is a promising solution to accelerate post-heat treatment development. The additive manufacturing technique can be leveraged as a useful tool for the implementation of high-throughput experiments.

More work is suggested in the future to expand the research:

- By assuming the diffusion-controlled process of homogenization, an improved diffusion database with the Laves_C14 phase involved should be developed to guide the design of post-heat treatment better. Moreover, the interfacial effects during Laves_C14 dissolution can be taken into consideration to further enhance the accuracy of the model-prediction.
- Although the variation of oxidation and carbon content due to the manufacturing processes were not identified with a notable impact on microstructure and mechanical properties in this work, the extent of oxidation and carbon loss can be quantified and their potential influence can be further studied, which will support uncertainty quantification.
- The homogenization temperature and time can be further optimized to achieve a balance of manufacturing cost and materials properties. The current work only

studied the homogenization at 1180°C, which can be potentially lowered, and the homogenization time can be moderately extended to obtain similar microstructure and properties. A set of high-throughput experiments using the method proposed in Chapter 6.0 can be performed to efficiently optimize the combination of temperature and time for the homogenization process.

- Research on the residual stress in Inconel 718 alloys and how it impacts the phase transformation of the γ'' phase should be done in more detail. The type and level of residual stress at various locations and their effects on the precipitation kinetics, preferred orientation, and particle morphology of the γ'' phase should be studied both theoretically and experimentally.
- The mechanism of the relatively higher elongation anisotropy of the samples with the two-step optimized aging process is still unclear. Further dedicated work should be done to elucidate the underlying mechanisms.

Appendix A Calculation and experimental results of abnormal grain growth rate for the suction-cast sample homogenized at 1180°C for 12 h, AC12h

According to Kusama et al. [114], the grain growth rate can be expressed as:

$$\frac{dR}{dt} = M^{gb} \cdot \Delta G \quad \text{Appendix (A-1)}$$

of which R is the radius of a grain, t is the time, M^{gb} is the grain boundary mobility, ΔG is the driving pressure of the grain growth.

The ΔG includes two contributions: ΔG_s , which represents the driving pressure from subgrain boundaries, and ΔG_h , which is the driving pressure from pre-existing high-angle grain boundaries. In this work, no subgrains are observed. Hence ΔG becomes

$$\Delta G = \Delta G_h = \sigma_h V_m \left(\frac{C_n}{R_n} - \frac{C_a}{R_a} \right) \quad \text{Appendix (A-2)}$$

where σ_h is the grain boundary energy, which is not readily available. The only reported value for the grain boundary energy in Inconel 718 is considered as 0.424 J/m² from Nishimoto et al. [170] during the study of grain boundary liquation. This value is comparable with other work for the Inconel alloys [171]. V_m is the molar volume of Inconel 718 and is calculated to be 7.38×10⁻⁶ m³/mol using the TCNI8 database. R_n and R_a are the mean radii of normal grains and abnormal grains, respectively. The value of R_n is taken as 113.5 μm (representing the left peak of grain size

distribution in sample AC1h, Fig. 3-16(i)), and R_a is estimated to be 406.6 μm (representing the weighted average grain size of abnormal grains in sample AC12h). C_n and C_a are constants, and are taken as 1.5 and 1, respectively, for 3D growth case and when $R_n \ll R_a$ [114]. The value of ΔG is calculated as 0.0337 J/mol.

The grain boundary mobility M^{gb} is calculated by:

$$M^{gb} = \frac{D^{gb}}{\delta RT} \quad \text{Appendix (A-3)}$$

where δ is the grain boundary thickness and is used as 5×10^{-10} m [114,172,173], R is the constant of the ideal gas, T is the temperature, i.e., 1453.15 K (1180°C). D^{gb} is the diffusivity of the grain boundary. Due to the lack of experimental data of D^{gb} in Inconel 718, experimental parameters measured by Cermak [172] in a Ni-10.04Fe-18.98Cr (in wt.%) alloy are adopted. The D^{gb} is estimated by [172,173]:

$$D^{gb} = \frac{1}{s \cdot \delta} \{s\delta D^{gb}\}_0 \exp\left(-\frac{Q^{gb}}{RT}\right) \quad \text{Appendix (A-4)}$$

where s is the segregation factor, which equals the ratio of the concentrations of an element i in the grain boundary and in the matrix near the grain boundary. It is found that when the content of Cr approaches to about 20 wt.%, the gradients of elemental concentrations near grain boundaries are small, and the values of s of Cr and Fe can be considered as 1 [172]. In our case, the concentration of Cr in Inconel 718 is about 19 wt.%, which is close to the threshold of 20 wt.% in [172]. Additionally, it is reasonable to speculate that the high-temperature and long-time

homogenization applied on the alloys can reduce the grain boundary segregation to a relatively low level. Therefore, $s=1$ is an acceptable assumption. $\{s\delta D^{gb}\}_0$ is the pre-exponential factor and Q^{gb} is the activation energy of grain boundary self-diffusion [172,173]. The values of $\{s\delta D^{gb}\}_0$ and Q^{gb} are taken as $1.349 \times 10^{-10} \text{ m}^3/\text{s}$ and $2.187 \times 10^5 \text{ J/mol}$ from [172], respectively. These values are for the diffusion of Fe in the grain boundaries of the Ni-10.04Fe-18.98Cr (in wt.%) alloy, since the diffusion of Fe was found to be slower than that of Cr, as reported in [172], becoming a controlling factor of grain boundary movement. The D^{gb} is calculated to be $3.71 \times 10^{-9} \text{ m}^2/\text{s}$.

The M^{gb} is estimated to be $6.142 \times 10^{-4} \text{ mol}\cdot\text{m}/(\text{J}\cdot\text{s})$. Hence, the theoretically predicted abnormal grain growth rate is $dR/dt=2.067 \times 10^{-5} \text{ m/s}$.

The experimental abnormal grain growth rate for the suction-cast sample homogenized at 1180°C for 12 h, i.e., the sample AC12h, is determined as follows. The grain growth from the beginning (0 h) to 12 h can be described by:

$$R(t)^2 - R_0^2 = kt \quad \text{Appendix (A-5)}$$

where $R(t)$ is the average abnormal grain radius at time t , and R_0 is the initial grain radius at the time t_0 . In this case, $R(t)$ is R_a , and R_0 is the average grain radii ($16 \mu\text{m}$) in the as-cast sample, respectively. k is a constant and calculated as $3.82 \times 10^{-12} \text{ m}^2/\text{s}$, and $t=12 \text{ h}$. Thus the experimental value of $dR/dt(t=12 \text{ h})$ is $4.7 \times 10^{-9} \text{ m/s}$.

Bibliography

- [1] Y. Zhao, K. Li, M. Gargani, W. Xiong, A comparative analysis of Inconel 718 made by additive manufacturing and suction casting: Microstructure evolution in homogenization, *Addit. Manuf.* 36 (2020) 101404. <https://doi.org/10.1016/j.addma.2020.101404>.
- [2] X. Zhao, J. Chen, X. Lin, W. Huang, Study on microstructure and mechanical properties of laser rapid forming Inconel 718, *Mater. Sci. Eng. A.* 478 (2008) 119–124. <https://doi.org/10.1016/j.msea.2007.05.079>.
- [3] E. Chlebus, K. Gruber, B. Kuźnicka, J. Kurzac, T. Kurzynowski, Effect of heat treatment on the microstructure and mechanical properties of Inconel 718 processed by selective laser melting, *Mater. Sci. Eng. A.* 639 (2015) 647–655. <https://doi.org/10.1016/j.msea.2015.05.035>.
- [4] M.M. Kirka, F. Medina, R. Dehoff, A. Okello, Mechanical behavior of post-processed Inconel 718 manufactured through the electron beam melting process, *Mater. Sci. Eng. A.* 680 (2017) 338–346. <https://doi.org/10.1016/j.msea.2016.10.069>.
- [5] ASTM International, B670–07: Standard specification for precipitation-hardening nickel alloy (UNS N07718) plate, sheet, and strip for high-temperature service, *ASTM Int.* (2010). <https://doi.org/10.1520/B0670-07>.
- [6] D.D. Keiser, H.L. Brown, Review of the physical metallurgy of Alloy 718, U.S. Department of Energy, 1976. <https://doi.org/10.2172/4016087>.
- [7] S. Sui, J. Chen, E. Fan, H. Yang, X. Lin, W. Huang, The influence of Laves phases on the high-cycle fatigue behavior of laser additive manufactured Inconel 718, *Mater. Sci. Eng. A.* 695 (2017) 6–13. <https://doi.org/10.1016/j.msea.2017.03.098>.
- [8] S.J. Hong, W.P. Chen, T.W. Wang, A diffraction study of the γ'' phase in INCONEL 718 superalloy, *Metall. Mater. Trans. A.* 32 (2001) 1887–1901. <https://doi.org/10.1007/s11661-001-0002-4>.
- [9] Y. Huang, T.G. Langdon, The evolution of delta-phase in a superplastic Inconel 718 alloy, *J. Mater. Sci.* 42 (2007) 421–427. <https://doi.org/10.1007/s10853-006-0483-z>.
- [10] G.P. Dinda, A.K. Dasgupta, J. Mazumder, Texture control during laser deposition of nickel-based superalloy, *Scr. Mater.* 67 (2012) 503–506. <https://doi.org/10.1016/j.scriptamat.2012.06.014>.
- [11] L. Xiao, D.L. Chen, M.C. Chaturvedi, Shearing of γ'' precipitates and formation of planar slip bands in Inconel 718 during cyclic deformation, *Scr. Mater.* 52 (2005) 603–607. <https://doi.org/10.1016/j.scriptamat.2004.11.023>.

- [12] M.C. Chaturvedi, Y. Han, Strengthening mechanisms in Inconel 718 superalloy, *Met. Sci.* 17 (1983) 145–149. <https://doi.org/10.1179/030634583790421032>.
- [13] Y.T. Chen, A.C. Yeh, M.Y. Li, S.M. Kuo, Effects of processing routes on room temperature tensile strength and elongation for Inconel 718, *Mater. Des.* 119 (2017) 235–243. <https://doi.org/10.1016/j.matdes.2017.01.069>.
- [14] Z. Chen, R.L. Peng, J. Moverare, P. Avdovic, J.M. Zhou, S. Johansson, Surface integrity and structural stability of broached Inconel 718 at high temperatures, *Metall. Mater. Trans. A.* 47 (2016) 3664–3676. <https://doi.org/10.1007/s11661-016-3515-6>.
- [15] M. Dehmas, J. Lacaze, A. Niang, B. Viguiet, TEM study of high-temperature precipitation of delta phase in inconel 718 alloy, *Adv. Mater. Sci. Eng.* 2011 (2011). <https://doi.org/10.1155/2011/940634>.
- [16] X. Wang, Z. Huang, B. Cai, N. Zhou, O. Magdysyuk, Y. Gao, S. Srivatsa, L. Tan, L. Jiang, Formation mechanism of abnormally large grains in a polycrystalline nickel-based superalloy during heat treatment processing, *Acta Mater.* 168 (2019) 287–298. <https://doi.org/10.1016/j.actamat.2019.02.012>.
- [17] F. Yan, W. Xiong, E. Faierson, G.B. Olson, Characterization of nano-scale oxides in austenitic stainless steel processed by powder bed fusion, *Scr. Mater.* 155 (2018) 104–108. <https://doi.org/10.1016/j.scriptamat.2018.06.011>.
- [18] D.M. Collins, B.D. Conduit, H.J. Stone, M.C. Hardy, G.J. Conduit, R.J. Mitchell, Grain growth behaviour during near- γ' solvus thermal exposures in a polycrystalline nickel-base superalloy, *Acta Mater.* 61 (2013) 3378–3391. <https://doi.org/10.1016/j.actamat.2013.02.028>.
- [19] W. Xiong, G.B. Olson, Cybermaterials: Materials by design and accelerated insertion of materials, *Npj Comput. Mater.* 2 (2016). <https://doi.org/10.1038/npjcompumats.2015.9>.
- [20] D. Zhang, W. Niu, X. Cao, Z. Liu, Effect of standard heat treatment on the microstructure and mechanical properties of selective laser melting manufactured Inconel 718 superalloy, *Mater. Sci. Eng. A.* 644 (2015) 32–40. <https://doi.org/10.1016/j.msea.2015.06.021>.
- [21] L. Chang, W. Sun, Y. Cui, R. Yang, Influences of hot-isostatic-pressing temperature on microstructure, tensile properties and tensile fracture mode of Inconel 718 powder compact, *Mater. Sci. Eng. A.* 599 (2014) 186–195. <https://doi.org/10.1016/j.msea.2014.01.095>.
- [22] S. Azadian, L.Y. Wei, R. Warren, Delta phase precipitation in inconel 718, *Mater. Charact.* 53 (2004) 7–16. <https://doi.org/10.1016/j.matchar.2004.07.004>.
- [23] W.J. Sames, K.A. Unocic, R.R. Dehoff, T. Lolla, S.S. Babu, Thermal effects on microstructural heterogeneity of Inconel 718 materials fabricated by electron beam melting, *J. Mater. Res.* 29 (2014) 1920–1930. <https://doi.org/10.1557/jmr.2014.140>.

- [24] M.J. Sohrabi, H. Mirzadeh, M. Rafiei, Solidification behavior and Laves phase dissolution during homogenization heat treatment of Inconel 718 superalloy, *Vacuum*. 154 (2018) 235–243. <https://doi.org/10.1016/j.vacuum.2018.05.019>.
- [25] M. Rafiei, H. Mirzadeh, M. Malekan, M.J. Sohrabi, Homogenization kinetics of a typical nickel-based superalloy, *J. Alloys Compd.* 793 (2019) 277–282. <https://doi.org/10.1016/j.jallcom.2019.04.147>.
- [26] A. Oradei-Basile, J.F. Radavich, A current T-T-T diagram for wrought Alloy 718, in: *Superalloys 718, 625 Var. Deriv.*, TMS, 1991: pp. 325–335. https://doi.org/10.7449/1991/Superalloys_1991_325_335.
- [27] Special Metals, (n.d.). https://www.specialmetals.com/assets/smc/documents/inconel_alloy_718.pdf (accessed November 3, 2019).
- [28] High Temp Metals, (n.d.). <https://www.hightempmetals.com/techdata/hitempInconel718data.php> (accessed November 3, 2019).
- [29] ASTM International, B637–18: Standard specification for precipitation-hardening and cold worked nickel alloy bars, forgings, and forging stock for moderate or high temperature service, *ASTM Int.* (2018). <https://doi.org/10.1520/B0637-18.2>.
- [30] T. Trosch, J. Ströbner, R. Völkl, U. Glatzel, Microstructure and mechanical properties of selective laser melted Inconel 718 compared to forging and casting, *Mater. Lett.* 164 (2016) 428–431. <https://doi.org/10.1016/j.matlet.2015.10.136>.
- [31] D. Zhang, Z. Feng, C. Wang, W. Wang, Z. Liu, W. Niu, Comparison of microstructures and mechanical properties of Inconel 718 alloy processed by selective laser melting and casting, *Mater. Sci. Eng. A.* 724 (2018) 357–367. <https://doi.org/10.1016/j.msea.2018.03.073>.
- [32] P. Han, Additive design and manufacturing of jet engine parts, *Engineering*. 3 (2017) 648–652. <https://doi.org/10.1016/J.ENG.2017.05.017>.
- [33] S.M. Thompson, L. Bian, N. Shamsaei, A. Yadollahi, An overview of Direct Laser Deposition for additive manufacturing; Part I: Transport phenomena, modeling and diagnostics, *Addit. Manuf.* 8 (2015) 36–62. <https://doi.org/10.1016/j.addma.2015.07.001>.
- [34] A. Jiménez, P. Bidare, H. Hassanin, F. Tarlochan, S. Dimov, K. Essa, Powder-based laser hybrid additive manufacturing of metals: a review, *Int. J. Adv. Manuf. Technol.* (2021) 63–96. <https://doi.org/10.1007/s00170-021-06855-4>.
- [35] D.D. Gu, W. Meiners, K. Wissenbach, R. Poprawe, Laser additive manufacturing of metallic components: Materials, processes and mechanisms, *Int. Mater. Rev.* 57 (2012) 133–164. <https://doi.org/10.1179/1743280411Y.0000000014>.

- [36] X. Gong, T. Anderson, K. Chou, Review on powder-based electron beam additive manufacturing Technology, *Manuf. Rev.* 1 (2014). <https://doi.org/10.1051/mfreview/2014001>.
- [37] S.W. Williams, F. Martina, A.C. Addison, J. Ding, G. Pardal, P. Colegrove, Wire+Arc additive manufacturing, *Mater. Sci. Technol. (United Kingdom)*. 32 (2016) 641–647. <https://doi.org/10.1179/1743284715Y.0000000073>.
- [38] J.P. Kruth, L. Froyen, J. Van Vaerenbergh, P. Mercelis, M. Rombouts, B. Lauwers, Selective laser melting of iron-based powder, *J. Mater. Process. Technol.* 149 (2004) 616–622. <https://doi.org/10.1016/j.jmatprotec.2003.11.051>.
- [39] A. Staub, A.B. Spierings, K. Wegener, Correlation of meltpool characteristics and residual stresses at high laser intensity for metal lpbfd process, *Adv. Mater. Process. Technol.* 5 (2019) 153–161. <https://doi.org/10.1080/2374068X.2018.1535643>.
- [40] A.S. Wu, D.W. Brown, M. Kumar, G.F. Gallegos, W.E. King, An experimental investigation into additive manufacturing-induced residual stresses in 316L stainless steel, *Metall. Mater. Trans. A*. 45 (2014) 6260–6270. <https://doi.org/10.1007/s11661-014-2549-x>.
- [41] X. Wang, X. Gong, K. Chou, Review on powder-bed laser additive manufacturing of Inconel 718 parts, *Proc. Inst. Mech. Eng. Part B J. Eng. Manuf.* 231 (2017) 1890–1903. <https://doi.org/10.1177/0954405415619883>.
- [42] C. Li, Z.Y. Liu, X.Y. Fang, Y.B. Guo, Residual stress in metal additive manufacturing, *Procedia CIRP*. 71 (2018) 348–353. <https://doi.org/10.1016/j.procir.2018.05.039>.
- [43] J. Smith, W. Xiong, W. Yan, S. Lin, P. Cheng, O.L. Kafka, G.J. Wagner, J. Cao, W.K. Liu, Linking process, structure, property, and performance for metal-based additive manufacturing: computational approaches with experimental support, *Comput. Mech.* 57 (2016) 583–610. <https://doi.org/10.1007/s00466-015-1240-4>.
- [44] S. Sui, H. Tan, J. Chen, C. Zhong, Z. Li, W. Fan, A. Gasser, W. Huang, The influence of Laves phases on the room temperature tensile properties of Inconel 718 fabricated by powder feeding laser additive manufacturing, *Acta Mater.* 718 (2019) 413–427. <https://doi.org/10.1016/J.ACTAMAT.2018.10.032>.
- [45] H. Qi, M. Azer, A. Ritter, Studies of standard heat treatment effects on microstructure and mechanical properties of laser net shape manufactured INCONEL 718, *Metall. Mater. Trans. A*. 40 (2009) 2410–2422. <https://doi.org/10.1007/s11661-009-9949-3>.
- [46] K. V. Yang, Y. Shi, F. Palm, X. Wu, P. Rometsch, Columnar to equiaxed transition in Al-Mg(-Sc)-Zr alloys produced by selective laser melting, *Scr. Mater.* 145 (2018) 113–117. <https://doi.org/10.1016/j.scriptamat.2017.10.021>.

- [47] F. Yan, W. Xiong, E. Faierson, Grain structure control of additively manufactured metallic materials, *Materials* (Basel). 10 (2017) 1260.
- [48] L. Thijs, F. Verhaeghe, T. Craeghs, J. Van Humbeeck, J.P. Kruth, A study of the microstructural evolution during selective laser melting of Ti-6Al-4V, *Acta Mater.* 58 (2010) 3303–3312. <https://doi.org/10.1016/j.actamat.2010.02.004>.
- [49] D. Deng, R.L. Peng, H. Brodin, J. Moverare, Microstructure and mechanical properties of Inconel 718 produced by selective laser melting: sample orientation dependence and effects of post heat treatments, *Mater. Sci. Eng. A.* 713 (2018) 294–306. <https://doi.org/10.1016/j.msea.2017.12.043>.
- [50] M. Ni, C. Chen, X. Wang, P. Wang, R. Li, X. Zhang, K. Zhou, Anisotropic tensile behavior of in situ precipitation strengthened Inconel 718 fabricated by additive manufacturing, *Mater. Sci. Eng. A.* 701 (2017) 344–351. <https://doi.org/10.1016/j.msea.2017.06.098>.
- [51] T. Mishurova, S. Cabeza, T. Thiede, N. Nadammal, A. Kromm, M. Klaus, C. Genzel, C. Haberland, G. Bruno, The influence of the support structure on residual stress and distortion in SLM Inconel 718 parts, *Metall. Mater. Trans. A.* 49 (2018) 3038–3046. <https://doi.org/10.1007/s11661-018-4653-9>.
- [52] P. Mercelis, J. Kruth, Residual stresses in selective laser sintering and selective laser melting, *Rapid Prototyp. J.* 12 (2006) 254–265. <https://doi.org/10.1108/13552540610707013>.
- [53] H. Qin, Z. Bi, H. Yu, G. Feng, R. Zhang, X. Guo, H. Chi, J. Du, J. Zhang, Assessment of the stress-oriented precipitation hardening designed by interior residual stress during ageing in IN718 superalloy, *Mater. Sci. Eng. A.* 728 (2018) 183–195. <https://doi.org/10.1016/j.msea.2018.05.016>.
- [54] J. Schneider, B. Lund, M. Fullen, Effect of heat treatment variations on the mechanical properties of Inconel 718 selective laser melted specimens, *Addit. Manuf.* 21 (2018) 248–254. <https://doi.org/10.1016/j.addma.2018.03.005>.
- [55] F. Liu, X. Lin, G. Yang, M. Song, J. Chen, W. Huang, Microstructure and residual stress of laser rapid formed Inconel 718 nickel-base superalloy, *Opt. Laser Technol.* 43 (2011) 208–213. <https://doi.org/10.1016/j.optlastec.2010.06.015>.
- [56] F. Liu, X. Lin, G. Yang, M. Song, J. Chen, W. Huang, Recrystallization and its influence on microstructures and mechanical properties of laser solid formed nickel base superalloy Inconel 718, *Rare Met.* 30 (2011) 433–438. <https://doi.org/10.1007/s12598-011-0319-0>.
- [57] Y.L. Hu, Y.L. Li, S.Y. Zhang, X. Lin, Z.H. Wang, W.D. Huang, Effect of solution temperature on static recrystallization and ductility of Inconel 625 superalloy fabricated by directed energy deposition, *Mater. Sci. Eng. A.* 772 (2020). <https://doi.org/10.1016/j.msea.2019.138711>.

- [58] I. Yadroitsev, P. Krakhmalev, I. Yadroitsava, Hierarchical design principles of selective laser melting for high quality metallic objects, *Addit. Manuf.* 7 (2015) 45–56. <https://doi.org/10.1016/j.addma.2014.12.007>.
- [59] Y. Tian, D. McAllister, H. Colijn, M. Mills, D. Farson, M. Nordin, S. Babu, Rationalization of microstructure heterogeneity in INCONEL 718 builds made by the direct laser additive manufacturing process, *Metall. Mater. Trans. A.* 45 (2014) 4470–4483. <https://doi.org/10.1007/s11661-014-2370-6>.
- [60] S. Malinov, Z. Guo, W. Sha, A. Wilson, Differential scanning calorimetry study and computer modeling of $\beta \Rightarrow \alpha$ phase transformation in a Ti-6Al-4V alloy, *Metall. Mater. Trans. A.* 32 (2001) 879–887. <https://doi.org/10.1007/s11661-001-0345-x>.
- [61] C. Radhakrishna, K.P. Rao, S. Srinivas, Laves phase in superalloy 718 weld metals, *J. Mater. Sci. Lett.* 14 (1995) 1810–1812. <https://doi.org/10.1007/BF00271015>.
- [62] C.I. Garcia, A.K. Lis, E.A. Loria, A.J. DeArdo, Thermomechanical processing and continuous cooling transformation behavior of IN-718, in: *Superalloys 1992 (Seventh Int. Symp., TMS, 1992: pp. 527–536*. https://doi.org/10.7449/1992/Superalloys_1992_527_536.
- [63] X. Hu, A. Nycz, Y. Lee, B. Shassere, S. Simunovic, M. Noakes, Y. Ren, X. Sun, Towards an integrated experimental and computational framework for large-scale metal additive manufacturing, *Mater. Sci. Eng. A.* 761 (2019) 138057. <https://doi.org/10.1016/j.msea.2019.138057>.
- [64] Y. Zhou, S. Chen, X. Chen, T. Cui, J. Liang, C. Liu, The evolution of bainite and mechanical properties of direct laser deposition 12CrNi2 alloy steel at different laser power, *Mater. Sci. Eng. A.* 742 (2019) 150–161. <https://doi.org/10.1016/j.msea.2018.10.092>.
- [65] S.W. Thompson, D.J. Vin Col, G. Krauss, Continuous cooling transformations and microstructures in a low-carbon, high-strength low-alloy plate steel, *Metall. Trans. A.* 21 (1990) 1493–1507. <https://doi.org/10.1007/BF02672564>.
- [66] M. Zhang, L. Li, R.Y. Fu, D. Krizan, B.C. De Cooman, Continuous cooling transformation diagrams and properties of micro-alloyed TRIP steels, *Mater. Sci. Eng. A.* 438–440 (2006) 296–299. <https://doi.org/10.1016/j.msea.2006.01.128>.
- [67] A.B. Cota, P.J. Modenesi, R. Barbosa, D.B. Santos, Determination of CCT diagrams by thermal analysis of an HSLA bainitic steel submitted to thermomechanical treatment, *Scr. Mater.* 40 (1998) 165–169. [https://doi.org/10.1016/S1359-6462\(98\)00410-2](https://doi.org/10.1016/S1359-6462(98)00410-2).
- [68] P.D. Jablonski, C.J. Cowen, Homogenizing a Nickel-based superalloy: Thermodynamic and kinetic simulation and experimental results, *Metall. Mater. Trans. B.* 40 (2009) 182–186. <https://doi.org/10.1007/s11663-009-9227-1>.

- [69] L. Geng, Y. Na, N.-K. Park, Continuous cooling transformation behavior of Alloy 718, *Mater. Lett.* 30 (1997) 401–405. [https://doi.org/10.1016/S0167-577X\(96\)00225-X](https://doi.org/10.1016/S0167-577X(96)00225-X).
- [70] C. Slama, G. Cizeron, Étude du comportement structural de l'alliage NC 19 Fe Nb (Inconel 718), *J. Phys. III.* 7 (1997) 665–688. <https://doi.org/10.1051/jp3:1997148>.
- [71] A. Niang, B. Viguiier, J. Lacaze, Some features of anisothermal solid-state transformations in alloy 718, *Mater. Charact.* 61 (2010) 525–534. <https://doi.org/10.1016/j.matchar.2010.02.011>.
- [72] J.W. Brooks, P.J. Bridges, Metallurgical Stability of Inconel Alloy 718, in: *Superalloys 1988* (Sixth Int. Symp., TMS, 1988: pp. 33–42. https://doi.org/10.7449/1988/Superalloys_1988_33_42.
- [73] L. Yang, K.-M. Chang, S. Mannan, J. DeBarbadillo, A new DTA approach for verifying precipitate solvus in Inconel alloy 718, in: *Superalloys 718, 625, 706 Var. Deriv.*, TMS, 1997: pp. 353–365. https://doi.org/10.7449/1997/Superalloys_1997_353_365.
- [74] X. Xie, C. Xu, G. Wang, J. Dong, W. Di Cao, R. Kennedy, TTT diagram of a newly developed nickel-base superalloy-Allvac® 718Plus™, *Proc. Int. Symp. Superalloys Var. Deriv.* (2005) 193–202. https://doi.org/10.7449/2005/superalloys_2005_193_202.
- [75] W.M. Tucho, V. Hansen, Characterization of SLM-fabricated Inconel 718 after solid solution and precipitation hardening heat treatments, *J. Mater. Sci.* 54 (2019) 823–839. <https://doi.org/10.1007/s10853-018-2851-x>.
- [76] C. Slama, C. Servant, G. Cizeron, Aging of the Inconel 718 alloy between 500 and 750 °C, *J. Mater. Res.* 12 (1997) 2298–2316. <https://doi.org/10.1557/JMR.1997.0306>.
- [77] F. Theska, K. Nomoto, F. Godor, B. Oberwinkler, A. Stanojevic, S.P. Ringer, S. Primig, On the early stages of precipitation during direct ageing of Alloy 718, *Acta Mater.* 188 (2020) 492–503. <https://doi.org/10.1016/j.actamat.2020.02.034>.
- [78] ASTM International, E8/E8M–16a: Standard test methods for tension testing of metallic materials, *ASTM Int.* (2016). https://doi.org/10.1520/E0008_E0008M-16A.
- [79] J. Bratberg, H. Mao, L. Kjellqvist, A. Engström, P. Mason, Q. Chen, The development and validation of a new thermodynamic database for Ni-based alloys, *Superalloys.* 12 (2012) 803–812.
- [80] M. Hillert, L.-I. Staffansson, The regular solution model for stoichiometric phases and ionic melts, *Acta Chem. Scand.* 24 (1970) 3618–3626. <https://doi.org/10.3891/acta.chem.scand.24-3618>.
- [81] B. Sundman, J. Ågren, The sublattice model, *MRS Proc.* 19 (1982) 115. <https://doi.org/10.1557/PROC-19-115>.

- [82] B. Sundman, J. Ågren, A regular solution model for phases with several components and sublattices, suitable for computer applications, *J. Phys. Chem. Solids.* 42 (1981) 297–301. [https://doi.org/10.1016/0022-3697\(81\)90144-X](https://doi.org/10.1016/0022-3697(81)90144-X).
- [83] O. Redlich, A.T. Kister, Algebraic representation of thermodynamic properties and the classification of solutions, *Ind. Eng. Chem.* 40 (1948) 345–348. <https://doi.org/10.1021/ie50458a036>.
- [84] K. Wu, F. Zhang, S. Chen, W. Cao, Y.A. Chang, A modeling tool for the precipitation simulations of superalloys during heat treatments, in: *Superalloys 2008 (Eleventh Int. Symp., TMS, 2008: pp. 933–939*. https://doi.org/10.7449/2008/Superalloys_2008_933_939.
- [85] N. Saunders, A.P. Miodownik, *CALPHAD: Calculation of phase diagrams - a comprehensive guide*, Elsevier, 1998. [https://doi.org/10.1016/S1470-1804\(98\)X8001-6](https://doi.org/10.1016/S1470-1804(98)X8001-6).
- [86] Y.M. Muggianu, M. Gambino, J.P. Bros, Enthalpies of formation of liquid alloys bismuth-gallium-tin at 723K-choice of an analytical representation of integral and partial thermodynamic functions of mixing for this ternary-system, *J. Chim. Phys. Physico-Chimie Biol.* 72 (1975) 83–88.
- [87] H. Lukas, S.G. Fries, B. Sundman, *Computational thermodynamics*, Cambridge University Press, Cambridge, 2007. <https://doi.org/10.1017/CBO9780511804137>.
- [88] J.-O. Andersson, T. Helander, L. Höglund, P. Shi, B. Sundman, Thermo-Calc & DICTRA, computational tools for materials science, *Calphad.* 26 (2002) 273–312. [https://doi.org/10.1016/S0364-5916\(02\)00037-8](https://doi.org/10.1016/S0364-5916(02)00037-8).
- [89] J. Andersson, J. Ågren, Models for numerical treatment of multicomponent diffusion in simple phases, *J. Appl. Phys.* 72 (1992) 1350–1355. <https://doi.org/10.1063/1.351745>.
- [90] Precipitation module (TC-PRISMA) user guide, (n.d.). <https://thermocalc.com/content/uploads/Documentation/Archive/2020-2024/2020b/2020b-precipitation-module-tc-prisma-user-guide.pdf>.
- [91] S. Sridar, Y. Zhao, W. Xiong, Phase transformations during homogenization of Inconel 718 alloy fabricated by suction casting and laser powder bed fusion: A CALPHAD case study evaluating different homogenization models, *J. Phase Equilibria Diffus.* 42 (2021) 28–41. <https://doi.org/10.1007/s11669-021-00871-3>.
- [92] E. Chlebus, K. Gruber, B. Kuźnicka, J. Kurzac, T. Kurzynowski, Effect of heat treatment on the microstructure and mechanical properties of Inconel 718 processed by selective laser melting, *Mater. Sci. Eng. A.* 639 (2015) 647–655. <https://doi.org/10.1016/j.msea.2015.05.035>.
- [93] W.M. Tucho, V. Hansen, Characterization of SLM-fabricated Inconel 718 after solid solution and precipitation hardening heat treatments, *J. Mater. Sci.* 54 (2019) 823–839. <https://doi.org/10.1007/s10853-018-2851-x>.

- [94] V.P. Sabelkin, G.R. Cobb, T.E. Shelton, M.N. Hartsfield, D.J. Newell, R.P. O'Hara, R.A. Kemnitz, Mitigation of anisotropic fatigue in nickel alloy 718 manufactured via selective laser melting, *Mater. Des.* 182 (2019) 108095. <https://doi.org/10.1016/j.matdes.2019.108095>.
- [95] X. Li, J.J. Shi, G.H. Cao, A.M. Russell, Z.J. Zhou, C.P. Li, G.F. Chen, Improved plasticity of Inconel 718 superalloy fabricated by selective laser melting through a novel heat treatment process, *Mater. Des.* 180 (2019). <https://doi.org/10.1016/j.matdes.2019.107915>.
- [96] W. Huang, J. Yang, H. Yang, G. Jing, Z. Wang, X. Zeng, Heat treatment of Inconel 718 produced by selective laser melting: microstructure and mechanical properties, *Mater. Sci. Eng. A.* 750 (2019) 98–107. <https://doi.org/10.1016/j.msea.2019.02.046>.
- [97] L. Yu, Z. Wang, J. Wu, X. Meng, X. Lai, Microstructure and properties of vacuum cast Sc-containing Be–Al alloys, *Int. J. Met.* 13 (2019) 201–212. <https://doi.org/10.1007/s40962-018-0249-9>.
- [98] Y. Liu, L. Shi, G. Yang, W. Jin, J. Cui, Microstructure and metastable phase in rapidly solidified TiAl alloy prepared by vacuum suction casting, *Cryst. Res. Technol.* 54 (2019) 1–7. <https://doi.org/10.1002/crat.201900054>.
- [99] L.Y. Sheng, W. Zhang, J.T. Guo, L.Z. Zhou, H.Q. Ye, Microstructure evolution and mechanical properties' improvement of NiAl–Cr(Mo)–Hf eutectic alloy during suction casting and subsequent HIP treatment, *Intermetallics.* 17 (2009) 1115–1119. <https://doi.org/10.1016/j.intermet.2009.05.003>.
- [100] L. Sheng, W. Zhang, J. Guo, H. Ye, Microstructure and mechanical properties of Hf and Ho doped NiAl–Cr(Mo) near eutectic alloy prepared by suction casting, *Mater. Charact.* 60 (2009) 1311–1316. <https://doi.org/10.1016/j.matchar.2009.06.005>.
- [101] Y. Tian, J.A. Muñoz-Lerma, M. Brochu, Nickel-based superalloy microstructure obtained by pulsed laser powder bed fusion, *Mater. Charact.* 131 (2017) 306–315. <https://doi.org/10.1016/j.matchar.2017.07.024>.
- [102] M.A. Taha, A.F. Yousef, K.A. Gany, H.A. Sabour, On selective laser melting of ultra high carbon steel: Effect of scan speed and post heat treatment, *Materwiss. Werksttech.* 43 (2012) 913–923. <https://doi.org/10.1002/mawe.201200030>.
- [103] E. Scheil, Bemerkungen zur schichtkristallbildung, *Zeitschrift Für Met.* 34 (1942) 70–72.
- [104] G.H. Gulliver, The quantitative effect of rapid cooling upon the constitution of binary alloys, *J. Inst. Met.* 9 (1913) 120–157.
- [105] Q. Chen, B. Sundman, Computation of partial equilibrium solidification with complete interstitial and negligible substitutional solute back diffusion, *Mater. Trans.* 43 (2002) 551–559. <https://doi.org/10.2320/matertrans.43.551>.

- [106] W.D. Cao, R.L. Kennedy, M.P. Willis, Differential thermal analysis (DTA) study of the homogenization process in alloy 718, *Miner. Met. Mater. Soc.* (1991) 147–160. https://doi.org/10.7449/1991/Superalloys_1991_147_160.
- [107] Z.J. Miao, A.D. Shan, Y.B. Wu, J. Lu, W.L. Xu, H.W. Song, Quantitative analysis of homogenization treatment of INCONEL718 superalloy, *Trans. Nonferrous Met. Soc. China* (English Ed. 21 (2011) 1009–1017. [https://doi.org/10.1016/S1003-6326\(11\)60814-5](https://doi.org/10.1016/S1003-6326(11)60814-5).
- [108] Y.L. Hu, X. Lin, S.Y. Zhang, Y.M. Jiang, X.F. Lu, H.O. Yang, W.D. Huang, Effect of solution heat treatment on the microstructure and mechanical properties of Inconel 625 superalloy fabricated by laser solid forming, *J. Alloys Compd.* 767 (2018) 330–344. <https://doi.org/10.1016/j.jallcom.2018.07.087>.
- [109] S. Sui, J. Chen, Z. Li, H. Li, X. Zhao, H. Tan, Investigation of dissolution behavior of laves phase in inconel 718 fabricated by laser directed energy deposition, *Addit. Manuf.* 32 (2020) 101055. <https://doi.org/10.1016/j.addma.2020.101055>.
- [110] H.L. Chen, Q. Chen, A. Engström, Development and applications of the TCAL aluminum alloy database, *Calphad Comput. Coupling Phase Diagrams Thermochem.* 62 (2018) 154–171. <https://doi.org/10.1016/j.calphad.2018.05.010>.
- [111] R. Maldonado, E. Nembach, The formation of precipitate free zones and the growth of grain boundary carbides in the nickel-base superalloy NIMONIC PE16, *Acta Mater.* 45 (1997) 213–224. [https://doi.org/10.1016/S1359-6454\(96\)00139-5](https://doi.org/10.1016/S1359-6454(96)00139-5).
- [112] M. Hillert, On the theory of normal and abnormal grain growth, *Acta Metall.* 13 (1965) 227–238. [https://doi.org/10.1016/0001-6160\(65\)90200-2](https://doi.org/10.1016/0001-6160(65)90200-2).
- [113] F.J. Humphreys, M. Hatherly, The control of the grain size by particles, in: *Recryst. Relat. Annealing Phenom.*, 2nd ed., Elsevier Ltd, 2004: p. 308.
- [114] T. Kusama, T. Omori, T. Saito, S. Kise, T. Tanaka, Y. Araki, R. Kainuma, Ultra-large single crystals by abnormal grain growth, *Nat. Commun.* 8 (2017) 354. <https://doi.org/10.1038/s41467-017-00383-0>.
- [115] P. Nandwana, M. Kirka, A. Okello, R. Dehoff, Electron beam melting of Inconel 718 : effects of processing and post-processing, *Mater. Sci. Technol.* 34 (2018) 612–619. <https://doi.org/10.1080/02670836.2018.1424379>.
- [116] D.P. Field, L.T. Bradford, M.M. Nowell, T.M. Lillo, The role of annealing twins during recrystallization of Cu, *Acta Mater.* 55 (2007) 4233–4241. <https://doi.org/10.1016/j.actamat.2007.03.021>.
- [117] C.D. Barrett, A. Imandoust, A.L. Oppedal, K. Inal, M.A. Tschopp, H. El Kadiri, Effect of grain boundaries on texture formation during dynamic recrystallization of magnesium alloys, *Acta Mater.* 128 (2017) 270–283. <https://doi.org/10.1016/j.actamat.2017.01.063>.

- [118] M. Zouari, N. Bozzolo, R.E. Loge, Mean field modelling of dynamic and post-dynamic recrystallization during hot deformation of Inconel 718 in the absence of δ phase particles, *Mater. Sci. Eng. A.* 655 (2016) 408–424. <https://doi.org/10.1016/j.msea.2015.12.102>.
- [119] A. Hadadzadeh, F. Mokdad, M.A. Wells, D.L. Chen, A new grain orientation spread approach to analyze the dynamic recrystallization behavior of a cast-homogenized Mg-Zn-Zr alloy using electron backscattered diffraction, *Mater. Sci. Eng. A.* 709 (2018) 285–289. <https://doi.org/10.1016/j.msea.2017.10.062>.
- [120] I. Basu, T. Al-Samman, Twin recrystallization mechanisms in magnesium-rare earth alloys, *Acta Mater.* 96 (2015) 111–132. <https://doi.org/10.1016/j.actamat.2015.05.044>.
- [121] A.A. Gazder, M. Sánchez-Araiza, J.J. Jonas, E. V. Pereloma, Evolution of recrystallization texture in a 0.78 wt.% Cr extra-low-carbon steel after warm and cold rolling, *Acta Mater.* 59 (2011) 4847–4865. <https://doi.org/10.1016/j.actamat.2011.04.027>.
- [122] L.H. Rettberg, T.M. Pollock, Localized recrystallization during creep in nickel-based superalloys GTD444 and René N5, *Acta Mater.* 73 (2014) 287–297. <https://doi.org/10.1016/j.actamat.2014.03.052>.
- [123] A. Imandoust, C.D. Barrett, A.L. Oppedal, W.R. Whittington, Y. Paudel, H. El Kadiri, Nucleation and preferential growth mechanism of recrystallization texture in high purity binary magnesium-rare earth alloys, *Acta Mater.* 138 (2017) 27–41. <https://doi.org/10.1016/j.actamat.2017.07.038>.
- [124] S. Mitsche, P. Pölt, C. Sommitsch, M. Walter, Quantification of the recrystallized fraction in a Nickel-base-alloy from EBSD-data, *Microsc. Microanal.* 9 (2003) 344–345. <https://doi.org/10.1017/S1431927603026229>.
- [125] S.W. Cheong, H. Weiland, Understanding a microstructure using GOS (grain orientation spread) and its application to recrystallization study of hot deformed Al-Cu-Mg alloys, *Mater. Sci. Forum.* 558–559 (2007) 153–158. <https://doi.org/10.4028/www.scientific.net/MSF.558-559.153>.
- [126] N. Allain-Bonasso, F. Wagner, S. Berbenni, D.P. Field, A study of the heterogeneity of plastic deformation in IF steel by EBSD, *Mater. Sci. Eng. A.* 548 (2012) 56–63. <https://doi.org/10.1016/j.msea.2012.03.068>.
- [127] B. Song, S. Dong, Q. Liu, H. Liao, C. Coddet, Vacuum heat treatment of iron parts produced by selective laser melting: Microstructure, residual stress and tensile behavior, *Mater. Des.* 54 (2014) 727–733. <https://doi.org/10.1016/j.matdes.2013.08.085>.
- [128] A.K. Sinha, Growth of MC particles on stacking faults and dislocations, *Metallography.* 20 (1987) 37–45. [https://doi.org/10.1016/0026-0800\(87\)90063-2](https://doi.org/10.1016/0026-0800(87)90063-2).
- [129] T. Omori, T. Kusama, S. Kawata, I. Ohnuma, Y. Sutou, Y. Araki, K. Ishida, R. Kainuma, Abnormal Grain Growth Induced by Cyclic Heat Treatment, *Science.* 341 (2013) 1500–1502. <https://doi.org/10.1126/science.1238017>.

- [130] M.Y. Shen, X.J. Tian, D. Liu, H.B. Tang, X. Cheng, Microstructure and fracture behavior of TiC particles reinforced Inconel 625 composites prepared by laser additive manufacturing, *J. Alloys Compd.* 734 (2018) 188–195. <https://doi.org/10.1016/j.jallcom.2017.10.280>.
- [131] G.E. Dieter, D.J. Bacon, Dislocation sources, in: *Mech. Metall.*, SI Metric, McGraw-Hill Book Company, 1986: p. 176.
- [132] M. Sundararaman, P. Mukhopadhyay, S. Banerjee, Deformation behaviour of γ'' strengthened inconel 718, *Acta Metall.* 36 (1988) 847–864. [https://doi.org/10.1016/0001-6160\(88\)90139-3](https://doi.org/10.1016/0001-6160(88)90139-3).
- [133] D. Fournier, A. Pineau, Low cycle fatigue behavior of Inconel 718 at 298 K and 823 K, *Metall. Trans. A.* 8 (1977) 1095–1105.
- [134] S. Kondo, T. Mitsuma, N. Shibata, Y. Ikuhara, Direct observation of individual dislocation interaction processes with grain boundaries, *Sci. Adv.* 2 (2016) e1501926. <https://doi.org/10.1126/sciadv.1501926>.
- [135] ASTM International, ASTM E-407: Standard practice for microetching metals and alloys, *ASTM Int.* 07 (2016) 1–22. <https://doi.org/10.1520/E0407-07R15E01.2>.
- [136] S. Sridar, Y. Zhao, W. Xiong, Cyclic re-austenitization of copper-bearing high-strength low-alloy steels fabricated by laser powder bed fusion, *Mater. Charact.* 166 (2020) 110437. <https://doi.org/10.1016/j.matchar.2020.110437>.
- [137] K.C. Russell, Nucleation in solids: the induction and steady state effects, *Adv. Colloid Interface Sci.* 13 (1980) 205–318. [https://doi.org/10.1016/0001-8686\(80\)80003-0](https://doi.org/10.1016/0001-8686(80)80003-0).
- [138] J. Svoboda, F.D. Fischer, P. Fratzl, E. Kozeschnik, Modelling of kinetics in multi-component multi-phase systems with spherical precipitates I: Theory, *Mater. Sci. Eng. A.* 385 (2004) 166–174. <https://doi.org/10.1016/j.msea.2004.06.018>.
- [139] Q. Zhang, S.K. Makineni, J.E. Allison, J.-C. Zhao, Effective evaluation of interfacial energy by matching precipitate sizes measured along a composition gradient with Kampmann-Wagner numerical (KWN) modeling, *Scr. Mater.* 160 (2019) 70–74. <https://doi.org/10.1016/j.scriptamat.2018.09.048>.
- [140] D.A. Porter, K.E. Easterling, Precipitation Growth, in: *Phase Transform. Met. Alloy.*, 2nd ed., Chapman & Hall, 1992: p. 281.
- [141] F. Theska, K. Nomoto, F. Godor, B. Oberwinkler, A. Stanojevic, S.P. Ringer, S. Primig, On the early stages of precipitation during direct ageing of Alloy 718, *Acta Mater.* 188 (2020) 492–503. <https://doi.org/10.1016/j.actamat.2020.02.034>.
- [142] M. Sundararaman, P. Mukhopadhyay, S. Banerjee, Precipitation of the δ -Ni₃Nb phase in two nickel base superalloys, *Metall. Trans. A.* 19 (1988) 453–465. <https://doi.org/10.1007/BF02649259>.

- [143] C.X. Huang, W.P. Hu, Q.Y. Wang, C. Wang, G. Yang, Y.T. Zhu, An ideal ultrafine-grained structure for high strength and high ductility, *Mater. Res. Lett.* 3 (2015) 88–94. <https://doi.org/10.1080/21663831.2014.968680>.
- [144] S. Gribbin, J. Bicknell, L. Jorgensen, I. Tsukrov, M. Knezevic, Low cycle fatigue behavior of direct metal laser sintered Inconel alloy 718, *Int. J. Fatigue.* 93 (2016) 156–167. <https://doi.org/10.1016/j.ijfatigue.2016.08.019>.
- [145] Z. Zhang, Z. Yang, S. Lu, A. Harte, R. Morana, M. Preuss, Strain localisation and failure at twin-boundary complexions in nickel-based superalloys, *Nat. Commun.* 11 (2020) 1–11. <https://doi.org/10.1038/s41467-020-18641-z>.
- [146] Z. Wang, E. Denlinger, P. Michaleris, A.D. Stoica, D. Ma, A.M. Beese, Residual stress mapping in Inconel 625 fabricated through additive manufacturing: method for neutron diffraction measurements to validate thermomechanical model predictions, *Mater. Des.* 113 (2017) 169–177. <https://doi.org/10.1016/j.matdes.2016.10.003>.
- [147] D.J. Child, G.D. West, R.C. Thomson, Assessment of surface hardening effects from shot peening on a Ni-based alloy using electron backscatter diffraction techniques, *Acta Mater.* 59 (2011) 4825–4834. <https://doi.org/10.1016/j.actamat.2011.04.025>.
- [148] S.J. Lainé, K.M. Knowles, P.J. Doorbar, R.D. Cutts, D. Rugg, Microstructural characterisation of metallic shot peened and laser shock peened Ti–6Al–4V, *Acta Mater.* 123 (2017) 350–361. <https://doi.org/10.1016/j.actamat.2016.10.044>.
- [149] D. Kumar, S. Idapalapati, W. Wang, D.J. Child, T. Haubold, C.C. Wong, Microstructure-mechanical property correlation in shot peened and vibro-peened Ni-based superalloy, *J. Mater. Process. Technol.* 267 (2019) 215–229. <https://doi.org/10.1016/j.jmatprotec.2018.12.007>.
- [150] G.D. Smith, S.J. Patel, The role of niobium in wrought precipitation-hardened nickel-base alloys, *Proc. Int. Symp. Superalloys Var. Deriv.* (2005) 135–154. https://doi.org/10.7449/2005/superalloys_2005_135_154.
- [151] C.M. Kuo, Y.T. Yang, H.Y. Bor, C.N. Wei, C.C. Tai, Aging effects on the microstructure and creep behavior of Inconel 718 superalloy, *Mater. Sci. Eng. A.* 510–511 (2009) 289–294. <https://doi.org/10.1016/j.msea.2008.04.097>.
- [152] R. Chandrasekar, C.C.H. Lo, A.M. Frishman, B.F. Larson, N. Nakagawa, Quantification of precipitates and their effects on the response of nickel-base superalloy to shot peening, *AIP Conf. Proc.* 1430 (2012) 1437–1444. <https://doi.org/10.1063/1.4716385>.
- [153] M. Koyama, Z. Zhang, M. Wang, D. Ponge, D. Raabe, K. Tsuzaki, H. Noguchi, C.C. Tasan, Bone-like crack resistance in hierarchical metastable nanolaminate steels, *Science* (80-.). 355 (2017) 1055–1057. <https://doi.org/10.1126/science.aal2766>.

- [154] Aircraft Materials, (n.d.). <https://www.aircraftmaterials.com/data/nickel/718.html> (accessed November 3, 2019).
- [155] K.N. Amato, S.M. Gaytan, L.E. Murr, E. Martinez, P.W. Shindo, J. Hernandez, S. Collins, F. Medina, Microstructures and mechanical behavior of Inconel 718 fabricated by selective laser melting, *Acta Mater.* 60 (2012) 2229–2239. <https://doi.org/10.1016/j.actamat.2011.12.032>.
- [156] M.M. Kirka, F. Medina, R. Dehoff, A. Okello, Mechanical behavior of post-processed Inconel 718 manufactured through the electron beam melting process, *Mater. Sci. Eng. A.* 680 (2017) 338–346. <https://doi.org/10.1016/j.msea.2016.10.069>.
- [157] A. Strondl, M. Palm, J. Gnauk, G. Frommeyer, Microstructure and mechanical properties of nickel based superalloy IN718 produced by rapid prototyping with electron beam melting (EBM), *Mater. Sci. Technol.* 27 (2011) 876–883. <https://doi.org/10.1179/026708309X12468927349451>.
- [158] J. Strößner, M. Terock, U. Glatzel, Mechanical and microstructural investigation of Nickel-based superalloy IN718 manufactured by selective laser melting (SLM), *Adv. Eng. Mater.* 17 (2015) 1099–1105. <https://doi.org/10.1002/adem.201500158>.
- [159] ASTM International, F3055-14a: Standard specification for additive manufacturing Nickel alloy (UNS N07718) with powder bed fusion, *ASTM Int.* (2014). <https://doi.org/10.1520/F3055-14A>.
- [160] Y. Zhao, N. Sargent, K. Li, W. Xiong, A new high-throughput method using additive manufacturing for alloy design and heat treatment optimization, *Materialia.* 13 (2020) 1–5. <https://doi.org/10.1016/j.mtla.2020.100835>.
- [161] C. Wei, J.C. Zhao, Gradient temperature heat treatment for efficient study of phase precipitation in a high-temperature Fe-Cr-Mo ferritic steel, *Materialia.* 3 (2018) 31–40. <https://doi.org/10.1016/j.mtla.2018.10.003>.
- [162] A. Agrawal, A. Choudhary, Perspective: Materials informatics and big data: Realization of the “fourth paradigm” of science in materials science, *APL Mater.* 4 (2016). <https://doi.org/10.1063/1.4946894>.
- [163] J.J. de Pablo, N.E. Jackson, M.A. Webb, L.Q. Chen, J.E. Moore, D. Morgan, R. Jacobs, T. Pollock, D.G. Schlom, E.S. Toberer, J. Analytis, I. Dabo, D.M. DeLongchamp, G.A. Fiete, G.M. Grason, G. Hautier, Y. Mo, K. Rajan, E.J. Reed, E. Rodriguez, V. Stevanovic, J. Suntivich, K. Thornton, J.C. Zhao, New frontiers for the materials genome initiative, *Npj Comput. Mater.* 5 (2019) 1–23. <https://doi.org/10.1038/s41524-019-0173-4>.
- [164] Y. Ning, Z. Yao, H. Guo, M.W. Fu, Structural-gradient-materials produced by gradient temperature heat treatment for dual-property turbine disc, *J. Alloys Compd.* 557 (2013) 27–33. <https://doi.org/10.1016/j.jallcom.2013.01.011>.

- [165] A. Oradei-Basile, J.F. Radavich, A current T-T-T diagram for wrought alloy 718, in: *Superalloys 718, 625 Var. Deriv.*, TMS, 1991: pp. 325–335. https://doi.org/10.7449/1991/Superalloys_1991_325_335.
- [166] J.M. Oblak, D.F. Paulonis, D.S. Duvall, Coherency strengthening in Ni base alloys hardened by DO22 γ' precipitates, *Metall. Trans.* 5 (1974) 143–153. <https://doi.org/https://doi.org/10.1007/BF02642938>.
- [167] Y. Ji, Y. Lou, M. Qu, J.D. Rowatt, F. Zhang, T.W. Simpson, L.Q. Chen, Predicting coherency loss of γ'' precipitates in IN718 superalloy, *Metall. Mater. Trans. A.* 47 (2016) 3235–3247. <https://doi.org/10.1007/s11661-016-3480-0>.
- [168] R.Y. Zhang, H.L. Qin, Z.N. Bi, J. Li, S. Paul, T.L. Lee, S.Y. Zhang, J. Zhang, H.B. Dong, Evolution of lattice spacing of gamma double prime precipitates during aging of polycrystalline Ni-base superalloys: an in situ investigation, *Metall. Mater. Trans. A.* 51 (2020) 574–585. <https://doi.org/10.1007/s11661-019-05536-y>.
- [169] R. Cozar, A. Pineau, Morphology of γ' and γ'' precipitates and thermal stability of Inconel 718 type alloys, *Metall. Trans.* 4 (1973) 47–59. <https://doi.org/10.1007/BF02649604>.
- [170] K. Nishimoto, I. Woo, T. Ogita, M. Shirai, Mathematical Simulation of Grain Boundary Liquation in HAZ during Welding-Study on Weldability of Cast Alloy 718 (Report 5), *Weld. Res. ABROAD.* 19 (2001) 317–325.
- [171] D.D. Pruthi, M.S. Anand, R.P. Agarwala, Diffusion of chromium in Inconel-600, *J. Nucl. Mater.* 64 (1977) 206–210. [https://doi.org/10.1016/0022-3115\(77\)90026-5](https://doi.org/10.1016/0022-3115(77)90026-5).
- [172] J. Čermák, Grain boundary self-diffusion of 51Cr and 59Fe in austenitic NiFeCr alloys, *Mater. Sci. Eng. A.* 148 (1991) 279–287. [https://doi.org/10.1016/0921-5093\(91\)90830-G](https://doi.org/10.1016/0921-5093(91)90830-G).
- [173] P. Lejcek, Grain boundary diffusion, in: *Grain Bound. Segreg. Met.*, Springer, 2010: pp. 190–196. <https://doi.org/10.1007/978-3-642-12505-8>.